Dublin City University

Reactive Oxygen and Nitrogen Species Detection Produced by an Atmospheric Pressure Plasma Jet

Candidate:

Louis Free

B. Sc. (Hons), M. Eng.

58368007

Supervisor:

Prof. Stephen Daniels

Co-Supervisors

Dr. James Conway

Prof. Enda McGlynn

Submitted as part of the degree of Doctor of Philosophy (PhD)

from

Dublin City University,

School of Electronic Engineering

November 2020

Declaration: I hereby certify that this material, which I now submit for assessment on the programme of study leading to the award of Ph.D. is entirely my own work, that I have exercised reasonable care to ensure that the work is original, and does not to the best of my knowledge breach any law of copyright, and has not been taken from the work of others save and to the extent that such work has been cited and acknowledged within the text of my work.

Signed (candidates signature): _____

Candidate name (typed): Louis Free

Student Number: 58368007

Date: November 14, 2021

Acknowledgements

I like to take this time to acknowledge the people who, without, this piece of work would not have been possible.

First and foremost, my supervisor Professor Stephen Daniels, whose guidance, encouragement and occasional kick in the back side pushed me to not only complete this work, but to do so at my highest capabilities.

To my co-supervisors, Professor Enda McGlynn and Dr. Jim Conway. Your expertise in the lab made were invaluable. Thank you for taking the time to read my work and guide me through the Viva.

To Dr.'s Rajani, Niall, Sharath, Sean. Your constant guidance, knowledge, expertise and know how was invaluable in helping me complete this work. I would also take a special moment to acknowledge Mr. Conor Murphy whose hard work and dedication throughout made possible a lot of this work.

To Ronan, Cleo, Ben, Brian and Conor. The endless games of pool, Friday NuBar pints and late nights were a much needed distraction. I wish you all the best in your future endeavours and thank you for your friendship.

To Fiona, Ruth, Ciprian, Sean, Adrian, Elena and all at the Water Institute. Thank you for providing a distraction and showing there is a light at the end of the tunnel.

As is tradition, to Dr. Bert Ellingboe and his coffee machine. A true work horse of the Physics department, many a Ph.D. would not have been complete without a constant source of high quality coffee.

To my parents Nuala and Eamonn and siblings Kevin and Kathryn, for your constant support throughout all of my education. I wouldn't be who I am today without you.

Finally, to Aisling, I don't know how you put up with me, but I incredibly thankful and grateful that you did. Your constant support and encouragement enabled me to finish this work, while also providing welcome distractions, especially during the pandemic.

Abstract

Reactive Oxygen and Nitrogen Species Detection Produced by an Atmospheric Pressure Plasma Jet

Louis Free

This thesis presents a novel, asymmetrical atmospheric pressure plasma jet, that uses air as its working gas, operating in the kilohertz range. The plasma system is designed to be mobile, easily set-up in many environments and has variable controllability, such as voltage, airflow and electrode position.

The initial body of work presented in the thesis relates to the design and development of the atmospheric pressure plasma jet used throughout the bulk of the thesis. The key components of the atmospheric plasma jet are introduced. Electrical measurements of the plasma were also preformed and showed that the plasma operated electrically in two modes, the so called noisy and quiet modes.

Optical emission spectroscopy was preformed on the plasma jet and showed that the emission spectrum of the jet was complex, containing emissions from many species, both molecular and atomic. These species included but were not limited to atomic species of nitrogen, oxygen and hydrogen and molecular emissions from N_2, O_2 and OH. In addition to this, it is possible to control the emission intensities from these species by varying the control parameters of the plasma jet such as voltage, airflow and electrode distance.

The observed emission spectra were noticed to be lacking in any optical features due to emissions from nitric oxide, while it was believed to be the case that the plasma jet should produce nitric oxide. To test this hypothesis the experimental method laser induced fluorescence was chosen as a means to probe

for nitric oxide in the plume region of the plasma. Experimentally it was found that nitric oxide was present within the plume. In addition by again varying the control parameters of the plasma jet the absolute number density of nitric oxide within the plume of the plasma could be varied.

Finally, two-photon absorption laser induced fluorescence is used to probe for atomic oxygen in the plume region of the atmospheric pressure plasma jet. Two-photon absorption differs from the single photon method in that two photons are simultaneously absorbed by and used to excite the species under investigation, opening up the possibility to probe species with excitation energies that are difficult to reach using conventional lasers systems. Like, the case for nitric oxide, atomic oxygen was confirmed to be present within the plume, although it was not possible to determine an absolute number density. Likewise, by varying the control parameters a change in the trend in the intensity of the fluorescence was observed.

Contents

List of Figures

List of Tables

1 Introduction

Over the course of the past two decades, the interest and development of atmospheric pressure plasma (APPs) has grown substantially. The science has become more mature and has seen novel and growing applications in various industries such as biomedical, aerospace, agricultural and food handling industries, as well as material processing. This is in due part due to the generation of active species that are beneficial to the processes of sterilization, surface decontamination and materials enhancement.

APPs are attractive in many industries for a variety of reasons, such as the ability to operate in air and ambient conditions, allowing continuous processing. They do not require expensive vacuum equipment. They come in a variety of configurations, geometries and specific types that can be matched to specific requirements. The ability to produce, at room temperature, a range of excited species without further thermal requirements, is also very attractive for many industries.

Within the field there are a number of open ended questions. In particular, in the biomedical, food processing industries and agricultural industries, reactive oxygen and nitrogen species (RONS) have been identified as the culprit for the anti-microbial properties of APPs. RONS however contain a rather large amount of atomic and molecular species, and an investigation into which particular species enhance or contribute to the anti-microbial properties of APPs and could possibly allow more tailored and suitable APPs to be produced.

This investigation however would be rather difficult as there are many various forms of microbes that range in size, structure and phenotype and what molecular “cocktail”

that works for one organism, may have no affect on another or may be more harmful than any potential treatment. For that reason, it is important to have an understanding of what species are present and generated by APPs.

1.1 Goals and motivations

The motivations behind this thesis was to design and build a low cost, portable atmospheric pressure plasma jet (APPJ) that could used in many applications such as the medical and food industries for surface decontamination and sterilization.

The APPJ was to be simple to set up, using off the shelf parts that could be easily sourced as required. To avoid the need to for gas tanks and allow the APPJ to be portable, air was to be the working gas. In addition to this, the APPJ was to be designed in such a way as to give the user flexibility in the control parameters used, such as voltage, electrode position and airflow.

As discussed, the nature of RONS is such that they contain a large number of atomic and molecular species. The nature of these species is complex and requires a great deal of understanding of plasma chemistry in order to ascertain their origin and role within the plasma. As such a number of optical experiments were designed to determine the chemical make up of the APPJ.

Optical emission spectroscopy (OES) is a powerful optical technique that can detect the emissions from excited particles produced in a plasma. The technique is especially useful as a it provides a non-invasive way to determine the make up of the plasma, while also being relatively easy to do.

Another powerful experimental tool is laser induced fluorescence (LIF). Using this technique it is possible to probe ground state species by using tuned laser emissions specific to the species under investigation and detecting the fluorescence emitted. Using appropriate calibration methods it is possible to determine the absolute number density of the species under investigation. It is also possible for a species to absorb multiple photons and therefore probe species with excitation energies that are difficulty to reach with conventional lasers, such as those with excitation energies in the VUV range. As such two-photon absorption laser induced fluorescence is another powerful experimental tool that can be used to probe ground state species with excitation energies in the VUV region of the spectrum and again if correctly calibrated allow the determination of the absolute number density of the species under investigation.

1.1.1 Goals

The goals of the thesis are as follows:

- Design and construct a low cost APPJ that could be easily moved from area to area and quickly set-up with minimal training or user requirements.
- Electrically characterise the APPJ to determine the nature of the APPJ and attempt to understand its behaviour.
- Determine the chemical make up of excited species in the APPJ by using optical emission spectroscopy
- By utilizing the experimental method of laser induced fluorescence, determine the absolute number density of NO in the plume region of the APPJ.

- By utilizing the experimental method of two-photon absorption laser induced fluorescence, determine the absolute number density of atomic oxygen in the plume region of the APPJ

1.2 Thesis contributions

In this thesis the aforementioned mentioned diagnostic methodologies are employed to gain a better understanding of the operation of the atmospheric pressure plasma jet designed for this work. An addition to this work is the use of APPJs as a means to increase the shelf life of food through bio-inactivation of spoilage micro-organisms [12, 13]. The contributions from this work are as follows:

1. Develop a cheap, portable atmospheric pressure plasma jet system that can be easily deployed in a range of situations such as food manufacturing or clinical environments and without the need for rf power. APPJs exist in many guises, most of which require the use of Noble gases as a feed gas. The excitation of these Noble gases is then typically used to induce chemistry in the ambient outside the jet or by the introduction of N_2/O_2 admixtures. The APPJ used in this work uses air as a working gas, negating the need for gas canisters and allowing indefinite, continuous deployment. The outcomes of this work show that it is possible to produce a cheap APPJ, using air as a working gas.

2. Test the efficacy of this APPJ for the removal of microbial lifeforms. Using the APPJ several investigation were made into the efficacy of the APPJ [12, 13]. The work presented in this thesis contributed to these works and showed that by using

the APPJ it was possible to remove microbial life from surfaces.

3. Determine the chemical make up of the APPJ. Early into the work it was noticed that by changing the control parameters of the APPJ it was possible to alter the colour of the light emitted from the APPJ indicating a change in the chemical composition of the discharge. Optical emission spectroscopy was used to show that by changing these parameters: voltage, electrode distance and airflow in particular, it was possible to alter the make-up of the plasma discharge. Throughout this work it will be shown that the emission spectrum of the APPJ varies as the control parameters are altered.

4. The discharge itself is not in contact with any of the treatment surfaces mentioned. In order to ascertain what species came into contact with microbially rich surfaces, laser induced fluorescence (LIF) and two-photon absorption laser induced fluorescence (TALIF) were used to probe for atomic oxygen (TALIF) and nitric oxide (LIF) within the plume region of the APPJ. Within this work it will be shown that it was possible to detect both of these species within the plasma plume and again by altering the control parameters, the absolute number densities of NO are influenced by the control parameters and that the trends in atomic oxygen are also influenced by the control parameters.

5. Finally the electrical behaviour of the APPJ was investigated to elucidate the possible influence of the electrical features on the plasma chemistry. The APPJ had unique electrical behaviour, with asymmetrical current-voltage signals observed. In addition, at least two modes of operation were observed, initially

named due to their audible behaviour as the noisy and quite modes. Electrically it will be shown that the behaviour of these modes is due to a large, short current spike typically 20 ns in duration with a simultaneous voltage drop, preventing the APPJ to transitioning to an arc. Electrically the two modes were distinguishable by a current spike and voltage per half cycle in the case of the noisy mode and single current spike and voltage drop during the negative half cycle for the quiet mode. It was hoped to link at least two of the diagnostic methods (OES and electrical) together to attempt to understand in full the behaviour of the jet, but this work was interrupted due to the COVID-19 pandemic.

1.3 Publications

- *Investigation into NO in an atmospheric pressure plasma jet.* Louis Free, James Conway, Miles M. Turner, Stephen Daniels. Journal of Applied Physics D. (being written)

- *Effect of non-thermal plasma technology on microbial inactivation and total phenolic content of a model liquid food system and black pepper grains.* Clementine Charoux, Louis Free, Laura Hinds, Rajani Vijayaraghavan, Stephen Daniels, Colm O'Donnel and Brijesh Tiwari. LWT - Food Science and Technology 2020

1.4 Conferences

- Conference On Cold Plasma Sources and Applications, Ypres 2018: Poster presentation

- Physics in Food Manufacturing 2017 Edinburgh: Poster presentation, awarded best poster
- International Union of Food Science and Technology 2016 Dublin: Poster presentation

1.5 Structure of the thesis

The thesis is structured as follows. In chapter 2 an introduction to the physics and forms of atmospheric pressure plasmas is presented. Chapter 3 presents the atmospheric pressure plasma jet used throughout the investigation and includes an investigation into the atmospheric pressure plasma jets electrical behaviour. Chapter 4 is an investigation into the emission spectra of the atmospheric pressure plasma jet to determine the excited species generated by the plasma. In chapters 5 and 6 the experimental procedure of laser induced fluorescence is introduced as a means to probe molecular and ground state species generated by the atmospheric pressure plasma jet. In chapter 5 laser induced fluorescence is used to determine the absolute number density of nitric, while chapter 6 uses two-photon absorption laser induced fluorescence to probe for atomic oxygen. Finally, chapter 7 concludes the work and discusses further work.

2 Atmospheric Pressure Plasmas

Plasma is one of the four fundamental sates of matter found in nature. The term was coined in the 1920s by chemist Irving Langmuir [14] as the behaviour reminded him of the medium, plasma, found in blood. As the temperature of a substance is increased, molecules and or atoms within the substance become more energetic, allowing a phase transformation from solid, liquid, gas and finally plasma as per figure 2.1. At high enough temperatures, molecules within the gas begin to dissociate and form a gas of atoms and followed by gas of freely moving moving charged particles.

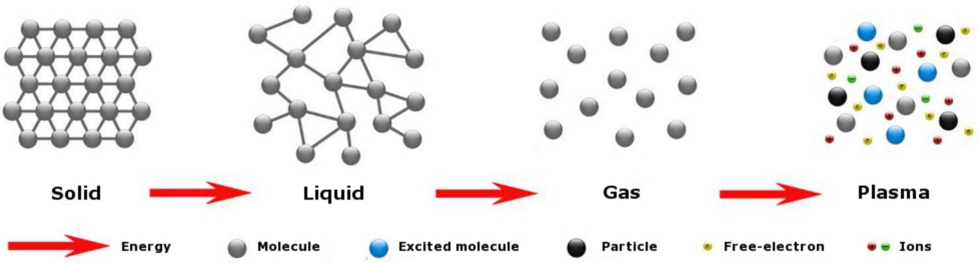

Figure 2.1: Phase transitions found in nature, from solid, liquid, gas and finally plasma.

The plasma state is characterised by a mixture of electrons, ions and neutral particles arranged and moving in random directions that on average is electrically neutral, the number of electrons $n_e \cong n_i$ the number of ions. The presence of these free charge carriers make plasmas electrically conductive, obtaining conductivities larger than metals like gold and copper [15].

Plasmas are the most common state of ordinary matter found in the observable universe (unless dark matter is accounted for). The vast majority of plasma is found at the cosmological level, in stars or in a highly rarefied form in intergalactic space.

At the terrestrial level, naturally occurring plasmas include lightning, auroras, corona discharges and electrical arcs. Plasmas are extensively used in industrial applications; from atmospheric arc welding to low pressure plasmas routinely used in the semiconductor [16–18] and medical device industry [19, 20].

Plasmas are typically classified according to their degree of ionization (electron or ion density) and the temperature (energy) of the electrons and neutrals [21, 22], as shown in figure 2.2 which outlines and classifies different plasmas based on their electron densities and temperature. Electrons, due to the relative difference in mass when compared with heavier particles are electrons able to obtain a greater energy distribution than the heavier ionic and neutral species within the plasma. This temperature imbalance allows highly energetic reactions to take place within the plasma whilst the gas temperature remains relatively low and often close to room temperature.

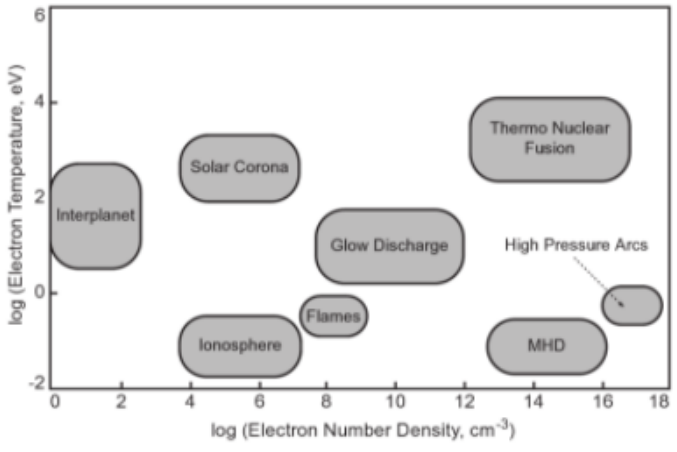

Figure 2.2: Plasma temperature and electron number density.

The atmospheric pressure plasmas of interest for this thesis are glow type discharges, with typical electron densities in the range of 10^8 to 10^{13} cm^{-3} and electron

temperatures between 1 and 8 eV as per figure 2.2. The electron densities of these types of plasmas is much lower than the gas density $\sim 10^{19}$ cm^{-3}, meaning that high energy electron collisions with the background gas are not enough to allow thermodynamic equilibrium and the gas remains cold. This allows plasmas to be used when temperature sensitive materials are involved. As the electron density becomes comparable to the gas density, an arc is formed, a plasma that is typically very close to thermodynamic equilibrium.

Plasma have two main properties that make them extremely useful for practical applications. Temperatures and energy densities that are greater than those produced by ordinary chemical means, and plasmas can produce energetic species that can initiate chemical reactions that are difficult or impossible to obtain using ordinary chemical mechanisms. Energetic particles generated by plasmas are numerous; charged particles (electrons and ions), atomic and molecular radicals, highly reactive neutral species such as reactive atoms (e.g. O, F, N etc.), excited atomic states, reactive molecular fragments and photons with energies ranging from the far IR to VUV, to name a few. These plasma produced species can then be utilised to participate in chemical or physical reactions with their surrounding environments such as gaseous or solid substrates [23–26] and in the production of radiation for discharge lamps and lasers [27–30].

When plasmas are used in treatment processes they typically have major benefits over existing material treatment processes and are at times the only possible way for the process to be preformed. Plasmas also typically provide an increase in efficiency in processing capabilities and can reduce the environmental impact by removing the

need for harmful chemicals.

Traditionally, plasma treatments and applications are preformed at pressures much lower than atmosphere, requiring expensive vacuum equipment and prohibiting continuous batch treatment processes [22,31,32]. Replacing some of these existing plasma processes with those that operate at atmospheric pressure and open is an attractive alternative for current plasma industries.

There are however many hurdles that must be overcome if the industry is to transition to atmospheric pressure plasmas. Low density and reduced collisions of hot electrons at low pressure make it relatively easy to sustain non-thermal plasmas, while at atmosphere these hot electrons are much more likely to make collisions, greatly increasing the possibility of arc formation. Larger voltages are also required to for the gas to breakdown.

The field and study of plasmas is large and in order to classify and diagnose plasmas, it is important to understand their fundamental characteristics and properties. The following chapter will attempt to understand the key components of plasmas, with an emphasis on those generated at atmospheric pressure. The breakdown mechanism, sustained ignition, volt-ampere characteristics will be outlined. Various approaches at forming plasmas will also be outlined as well as the key physical and chemically processes made possible by plasma.

2.1 Background

Development of atmospheric pressure plasmas (APPs) begin the early 20th century. The plasmas generated at this time were typically high-temperature, equilibrium plasmas. In the 1930s, von Engel *et al* attempted to lower the plasma temperature by controlling the cathode temperature [33]. However, it wasn't until the late 1980's and early 1990's that work on APP began in earnest. These early works used Dielectric Barrier Discharge (DBD) type configurations with He as a working gas [34–36]. Sinusoidal excitation voltages in the kV and kHz range were used to generate these plasmas.

In the late 1990s and early 2000s, the trend in APPs moved towards fast rise time voltage pulses with pulse widths in the nanosecond-to-microsecond range. These shorter pulses coupled energy more effectively to the electrons within the discharge, allowing greater control of the Electron Energy Distribution Function (EEDF) and therefore better control of the plasma chemistry [37–40]. These works contributed to the emergent applications of APPs in biology and medicine that started in the mid-1990s [41, 42].

As associated research and applications in biology and medicine progressed, the need for devices that could deliver species created by the plasma beyond the limited volume of the electrodes or discharge tubes where the plasma is generated became apparent. This led to the development of plasma sources that could deliver plasma plumes into the surrounding environment, known as Atmospheric Pressure Plasma Jets (APPJs) [43–59] .

2.2 Plasma Theory for APPSs

As a result of continuous cosmic radiation within the ambient atmosphere, electron-ion pairs are constantly generated, with typical values being 10^6 ion-electron pairs s^{-1} m^{-3}. Excess electrons created during this process provide the initial source of electrons required to generate a plasma.

In order to ignite or a spark a plasma, energy must be delivered to the free electrons created during this process. This energy can come in many forms such as thermal, electrical or optical, with electrical energy being the preferred industrial and laboratory method. Electrical energy is typically supplied through electromagnetic fields, in the form of high voltage electrodes or induction coils.

Sufficient energy must be delivered to the free electrons within the gas to free additional electrons creating an avalanche effect, known as electrical breakdown. Electrical breakdown depends on a number of factors, of which electric field strength (voltage), gas type and gas pressure are the most important factors.

2.2.1 Gas Breakdown

Gas breakdown is the transition of a gas from an insulating to a conductive state. In reality, the electrical breakdown of a gaseous medium is a complex multi-stage phenomenon. We can however better understand it if we consider the idealised scenario shown in figure 2.3, of two conducting metal plates connected to a DC power supply of voltage V, separated by a distance d. The space between the two electrodes is filled with an ideal, chemically pure gas at pressure P.

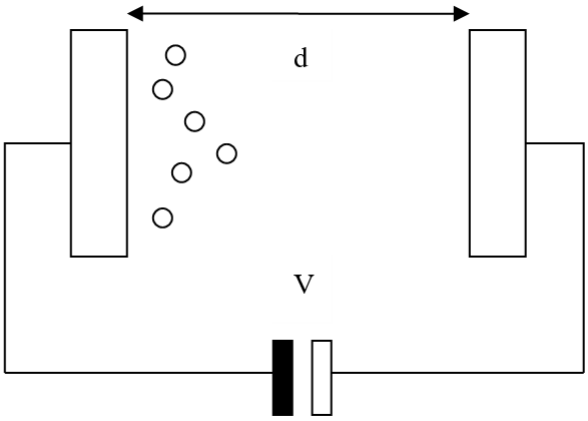

Figure 2.3: DC electrical gas discharge.

The presence of the naturally occurring background electrons in the gas act as a precursor for electrical breakdown. These electrons are accelerated towards the anode, due to the applied electric field E given by:

$$E = \frac{V}{d} \tag{2.1}$$

The velocity of the electrons within the gas is determined by two factors; random thermal motion due to collisions with other gas molecules and directed motion due to the applied electric field. The net velocity of the electrons, known as the drift velocity v_d is given by:

$$v_d = -\mu E \tag{2.2}$$

where, μ is the mobility of the electrons. The mobility of the electrons depends upon the density n_0 of the background gas.

If we consider the situation shown in figure 2.4, where an electron is travelling

through a volume xyz, normal to the xy surface, of neutral gas atoms at rest with respect to the electron. We will consider only a simple case were each collision is elastic and thus assume the atoms in the gas are hard spheres. In addition we will assume the electron is a point mass and neglect any effects arising from charge. Each volume of the gas will contain n_0xyz atoms, each of cross sectional area $\sigma = \pi r^2$, where r is the atomic radius, that will virtually obscure the surface xy as in figure 2.4. In this idealised scenario, a collision between an electron and a gas atom will occur with very high statistical probability when the z axis extends as far as λ_m.

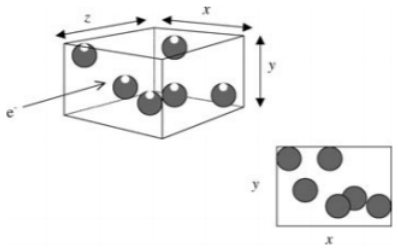

Figure 2.4: Electron collision with background gas.

This distance λ_m, is known as the electron mean free path, the average distance a particle will travel before colliding with another. When viewed through the xy plane, the total area blocked by atoms will be given by $n_g xyz\sigma$ and we can say

$$(n_g xy\lambda_m)\sigma = xy \tag{2.3}$$

rearranging,

$$\lambda_m = \frac{1}{\sigma n_g} \tag{2.4}$$

If the kinetic energy T, gained by the electron prior to a collision with a gas atom is greater than the energy required to ionise a neutral atom V_i, an electron may be released from the atom. Such secondary electrons are subject to the same applied field and accelerated towards the anode. This may lead to further ionisation events resulting in multiplication of electrons or electron avalanche effect shown in figure 2.5 that evolves in both space and time.

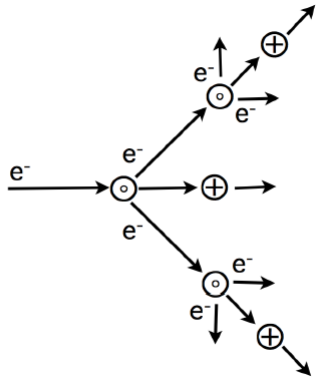

Figure 2.5: Electron avalanche mechanism [1].

After one mean free path for ionization λ_i an electron produces on average one electron ion pair and we can represent the increase in the number of electrons in a small segment of gas with thickness dx as

$$dN = N\frac{dx}{\lambda_i} \tag{2.5}$$

where N is the number of electrons. As a result of this, the electron (and positive ion) population increases exponentially with distance giving

$$N = N_0 \exp(x/\lambda_i) \tag{2.6}$$

2.2.2 Townsend Breakdown Theory

The number of ionisation events per unit length α, is in general a function of the type of gas, pressure and applied electric field. This relation was determined semi-empirically by Townsend and produced the formula:

$$\alpha = PA \exp \frac{-BP}{E} \tag{2.7}$$

where A and B are specific to the type of gas and α is the Townsend ionisation coefficient [2].

The rate of electron production along the direction of the electric field with respect to the axial distance from the cathode is given by:

$$\frac{dne}{dx} = \alpha n_e \tag{2.8}$$

where n_e is the number of electrons created along the length. Integrating leads to:

$$n_e(x) = n_{e0} \exp(\alpha x) \tag{2.9}$$

where n_{e0} is the initial number of electrons present in the gas.

Up to this point, we were only concerned with the behaviour of electrons present in the gas. Next, attention turns to the positive ions created during the ionisation process which will be accelerated to the cathode. In order for the discharge to become self sufficient, positive ions initially close to the cathode must also lead to the production of secondary electrons from the cathode surface through ion bombardment, otherwise the discharge will extinguish. We can therefore say that the number of secondary

electrons per incident ion is given by γ.

Ions, which are created by the electron avalanche propagating through the gas, are accelerated towards the cathode. Ion bombardment of the cathode can lead to the emission of secondary electrons. These secondary electrons are subject to the applied field and can subsequently cause further avalanching. The discharge will then become self sustaining when the number of secondary electrons produced through ion bombardment equals the number of ions lost to the cathode. According to equations 2.5 and 2.9 N_0 initial electrons will produce $\alpha N_0 exp(\alpha x)dx$ ions in the small space dx. Therefore across the gap there will be $N_0\left[exp(\alpha d) - 1\right]$ ions generated. To be self sustaining

$$\gamma N_0\Big[\exp(\alpha d) - 1\Big] = N_0 \tag{2.10}$$

Simplified to:

$$\alpha d = \ell n\Big(1 + \frac{1}{\gamma}\Big) \tag{2.11}$$

where γ is the secondary electron emission coefficient [2, 60].

Using the planar geometry in figure 2.3, the breakdown voltage must occur when

$$V_b = Ed \tag{2.12}$$

Therefore combining equations 2.7 and 2.11, we arrive at the Paschen Law for gas discharges [61].

$$V_b = \frac{BPd}{ln(APd) - ln\Big[ln(1 + \gamma^{-1})\Big]} \tag{2.13}$$

Figure 2.6 [15,61,62] shows the characteristic of curve electrical breakdown for various gases. At low Pd values, the gas is almost in a state of vacuum, resulting in the breakdown voltage going to infinity. This can be explained by either the electrons not having enough distance to travel between electrodes to gain the required ionisation energy or there not being enough gas particles within the space for the electrons to collide with. At some Pd value for each gas, the curve will reach a minimum where ideal gas breakdown condition occur. After this point, the breakdown voltage begins to rise again as the gas becomes more dense and hence behaves more as an insulator [2, 61].

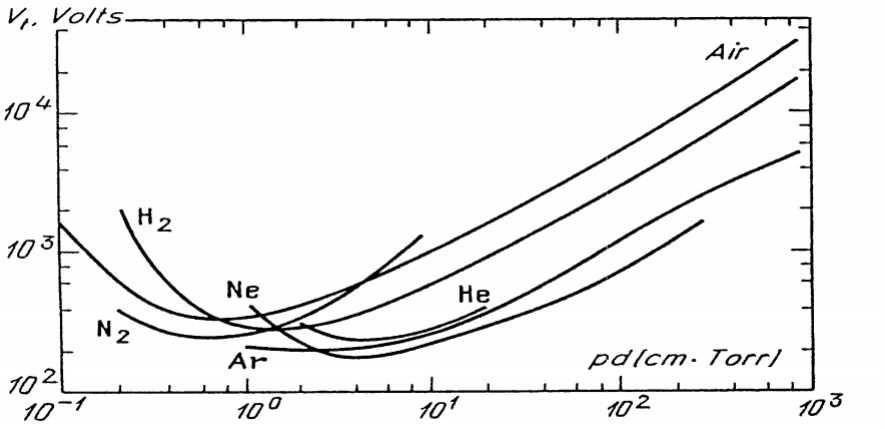

Figure 2.6: Paschen curve: Breakdown voltage as a function of electrode distance and voltage product (Pd) for various gases [2].

2.2.3 Streamer Breakdown of Gases

The theory of gas breakdown described so far, generally only applies to gases with low Pd values. Experiments carried out in the 1930s and 1940s showed however that for Pd values greater than 200 torr cm, a new model was required to explain the breakdown

mechanism. The time lag between breakdown and formation of a conducting gas could not be explained by the ion dominated plasma development mechanism described by the Townsend theory [2, 63].

In 1940, J. M. Meek developed the "streamer" theory to explain the development of such high Pd discharges [64]. Electric fields generated by the electron avalanche must be considered due to the large space charge created. Streamer development is shown in figure 2.7 [2, 3].

As the electron avalanche propagates towards the anode, the field generated by the avalanche head modifies the field between the electrodes. Assuming a spherical space charge due to the charge head, the electric field is given by:

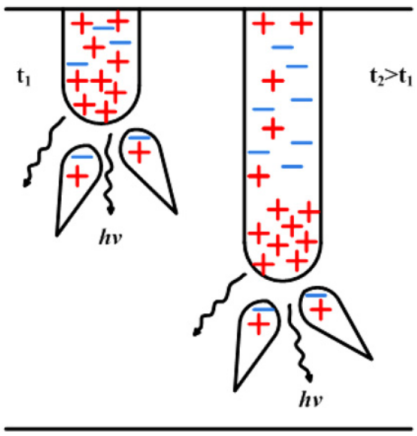

Figure 2.7: Streamer breakdown mechanism development and propagation at two different times [2, 3].

$$E = \frac{Ne}{4\pi\epsilon r^2} \tag{2.14}$$

where N is the number of charges in the head and r its radius. The radius of the

avalanche depends on the time t after the development of the avalanche and the diffusion coefficient D [2], given by:

$$r = \sqrt{4Dt} \tag{2.15}$$

When the avalanche field strength becomes comparable or greater to the applied field, secondary avalanches develop in front of the streamer head. Further avalanches are formed outside the charge head due to photoionisation. A highly conducting channel is rapidly formed by this process. The criterion for streamer development known as the *Raether criterion* [65] is given by:

$$\frac{\alpha}{p} d_{crit} = 20 + \ell n d_{crit} \tag{2.16}$$

where d_{crit} is the critical distance the avalanche head must travel to form a streamer. Typical streamer formation velocity is on the order of 10^6 ms^{-1}, close to the electron drift velocity, while discharges involving the Townsend mechanism proceed at much slower speeds of 10^3 ms^{-1} [63, 65].

2.3 Plasma Temperature

Due to the relatively large difference in the masses of electrons and ions, heating of charged particles by an external electric field is dominated by electron heating at low pressures. The collisional rate between electrons and heavy neutral and ionic species means that electrons come to thermodynamic equlilbrium amongst themselves much faster than they come into equilibrium with the ions or neutrals. The electron

temperature T_e can be one or two orders of magnitude greater than the neutral or ion temperatures T_n and T_i [66]. As the pressure increases, the collisional rate will rise to a point where energy can be exchanged effectively between the electrons and heavy particles so that $T_e \approx T_n$. This trend is shown in figure 2.8 [4].

When the temperature of the electrons and heavy particles are equal, the plasma is said to be at equilibrium or a thermal plasma. If the temperatures are different this type of plasma is known as a non-equilibrium or non-thermal plasma.

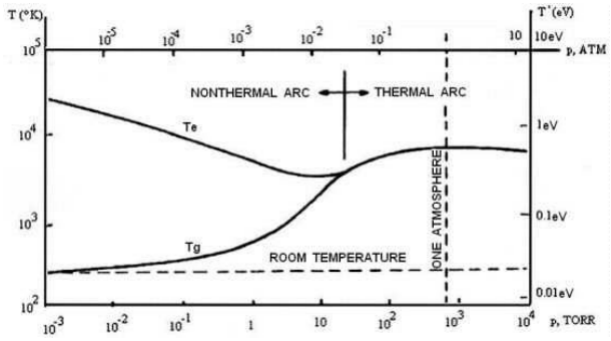

Figure 2.8: Electron and gas temperature as a function of pressure [4].

2.4 Plasma Scale

Charged particles within a gas that are disturbed by an external electric field will oscillate about an equilibrium driven by an electrostatic (Coulombic) restoring force. Electrons, due to their relatively light mass when compared to ions, are far more mobile than ions. As a result, electrons will have a much higher frequency response to any electrostatic forces, while ions will remain approximately stationary within this timeframe. The electron plasma frequency response therefore creates a fundamental time scale for the plasma known as the plasma period. The oscillatory response of

electrons allows collective conductive properties to emerge within the plasma while remaining overall electrically neutral on times-scales greater than the plasma period. This property is known as quasi-neutrality.

The electron plasma frequency highlights another fundamental feature of plasma behaviour. Considering an electron with thermal velocity v and oscillation period τ. The product of $v\tau$ gives a fundamental length scale known as the Debye length. The Debye length is the radius of force influence a charged particle has over its neighbouring charged particles. Coulomb electric potential lengths scales within the plasma are limited to the distance of the Debye length due to increased thermal motion of the electrons. The Debye λ_D length can be calculated using:

$$\lambda_D = \sqrt{\frac{\epsilon_0 k_B T_e}{e^2 n_e}} \tag{2.17}$$

which can be approximated:

$$\lambda_D = 740\sqrt{T_e/n_e} \tag{2.18}$$

where T_e is the electron temperature and n_e is the electron density [67], with units in eV. A steady state plasma not in contact with a boundary is electrically neutral at length scales above the Debye length and on time scales above the electron plasma period.

For the plasma state to exist, at least one other charge carrier must be within the Debye sphere of influence so that collective behaviour may emerge. Collective plasma behaviour emerges from local concentrations of charge confined to a Debye sphere

influencing other charges throughout the plasma. This final fundamental aspect of plasma is known as the plasma approximation.

2.5 Atmospheric pressure plasma characterisation

Various forms of atmospheric pressure plasma exist and are classified based on their volt - ampere characteristics as shown in figure 2.9. Included within this group are corona discharges [21], shown from D to E in figure 2.9, Dielectric Barrier Discharges (DBDs) from E to H; which include Filamentary Discharges (FDs) and ozonizers [68], and arc jets from H to K. Additional atmospheric pressure plasmas include the Atmospheric Pressure Plasma Jet (APPJ) [69], from F to K, the Atmospheric Pressure Glow (APG) [34] from D to G, and the One Atmosphere Uniform Glow Discharge Plasma (OAUGDP) [70] from F to H in figure 2.9. The various plasmas mentioned above while having unique properties, each share common properties including being non-thermal, non-equilibrium plasmas and produced in air or noble gases.

2.5.1 Corona discharges

A corona discharge is a positive or negative electrical discharge created by the ionisation of a gas surrounding a conductor. Corona discharges are formed by large, non-uniform electric fields at pointed conducting surfaces or thin wires. The discharge can be created using several geometrical arrangement: parallel coaxial cylinder, concentric spheres, parallel wires or parabolic tip to plane. Figure 2.10 shows various forms of both positive and negative corona discharges [5].

Corona discharges are always highly non-uniform and can be classified into two

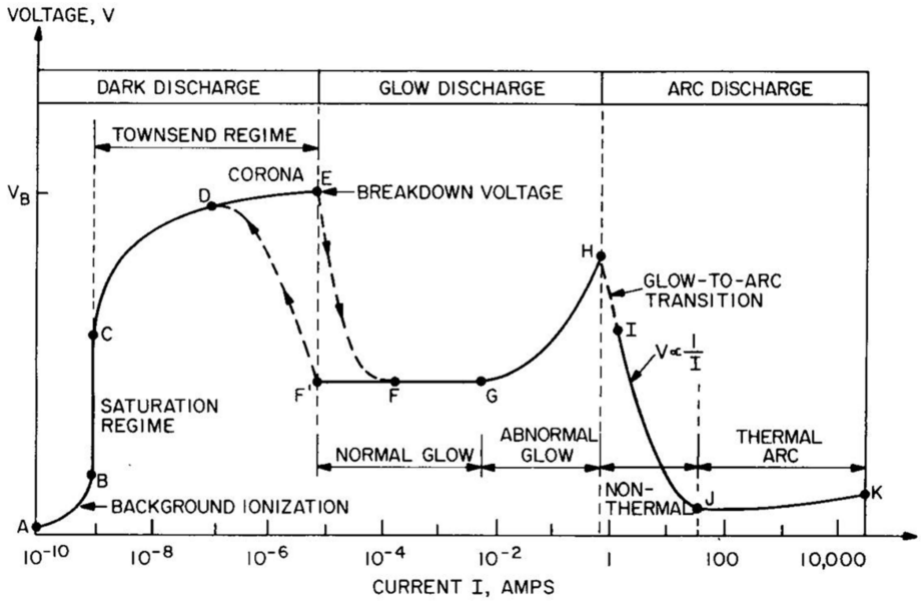

Figure 2.9: Plasma voltage - current characteristics.

categories based on the polarity of the applied voltage. A region of weak luminosity develops at the anode or cathode based on this polarity. Again, due to the mobility of electrons, negative coronas are much more difficult to initiate then their positive counterparts. For the case of positive coronas, ionisation is caused by the formation of a cathode directed streamer and in the case of a negative streamer through the Townsend mechanism, allowing a multiplication of avalanches and continuity of the plasma through the propagation of secondary electrons due to impact ionisation [21].

The power coupling to corona discharges is typically quite small. Increasing the voltage tends to have a small increase in the current through the discharge. Decreasing the distance between the electrodes would seem like a reasonable approach to increase the electric field. However, if the distance between the anode and cathode is not sufficiently large, then the resulting discharge can lead to the formation of a spark channel that results in a highly non-uniform plasma and localised heating, both of

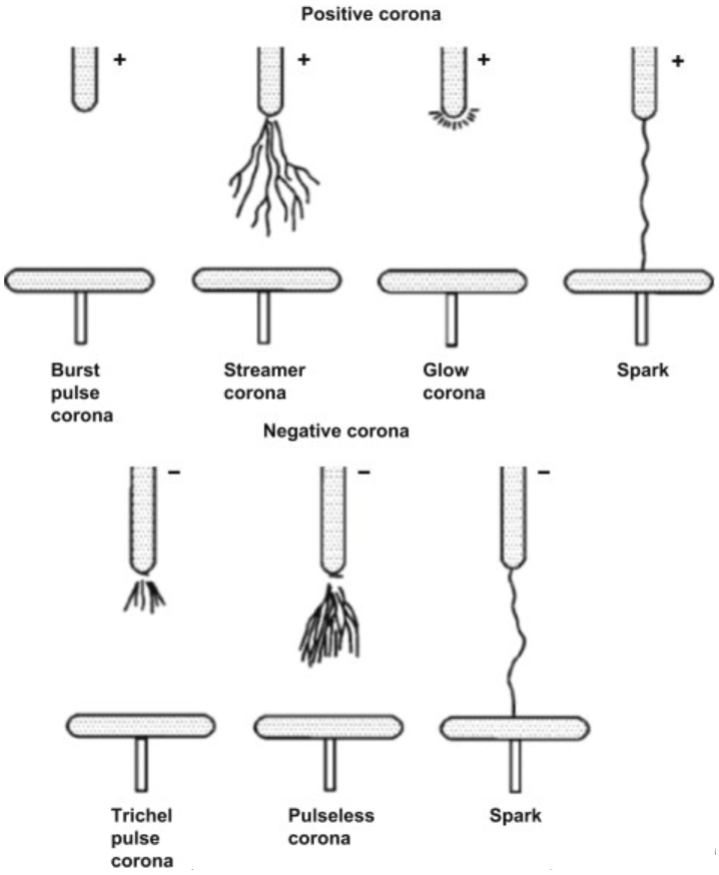

Figure 2.10: Various forms of positive and negative corona discharges [5].

which are undesirables for most applications.

Methods exist to prevent the formation of a spark usually through the application of a pulsed voltage that has sufficiently spaced intervals to enable streamer formation but preventing electron avalanches to breach the discharge gap, thereby preventing the spark formation. Pulsed discharges also has the benefit of greater power transfer efficiency and mean electron energies . Greater electron energies are required to increase the fraction of energy coupled to ionization and dissociation of molecules, rather than vibrational excitation of gas molecules [15]. Corona discharge applications are rather limited, usually invoked in gas cleaning and surface treatment where uniformity is not

required [21, 22].

2.5.2 Dielectric barrier discharge

An alternative method to prevent streamer to spark formation was developed by covering one or both of the electrodes in an insulating material, known as a dielectric barrier discharge (DBDs), the most common configurations are shown in figure 2.11. Also known as "silent discharges," "barrier discharges" or "ozonizer discharges;" DBDs were first discovered in 1857 by Siemens for the generation of ozone. DBDs have many applications, e.g. surface treatment [71–73], water treatment [74, 75], degradation of pollutant molecules in gases [76, 77], laser gas pumping [78–80], plasma displays, and the generation of excimer radiation [81]. More recently DBDs have been used for biological decontamination of medical devices [82, 83], wound healing [84] and dermatology [85, 86], air flows [74] and tissues [87–89].

DBDs are a form of atmospheric pressure plasma characterised by the presence of an insulation material within the discharge path, typically located on one or more of the electrodes, as seen in figure 2.11. The dielectric barrier is responsible for a self-pulsing plasma operation and thus the formation of a non-thermal plasma at atmospheric pressure. When a sufficiently high electric field is applied across the gap, local breakdown leads to the rapid formation of electron avalanches. These avalanches are able to produce such a large space charge that self-propagating streamers are able to form. A space charge induced field enhancement at the streamer head is reflected at the anode and reflected back towards the cathode forming an extremely thin cathode fall region within a fraction of a nanosecond. The current peaks at this moment as the

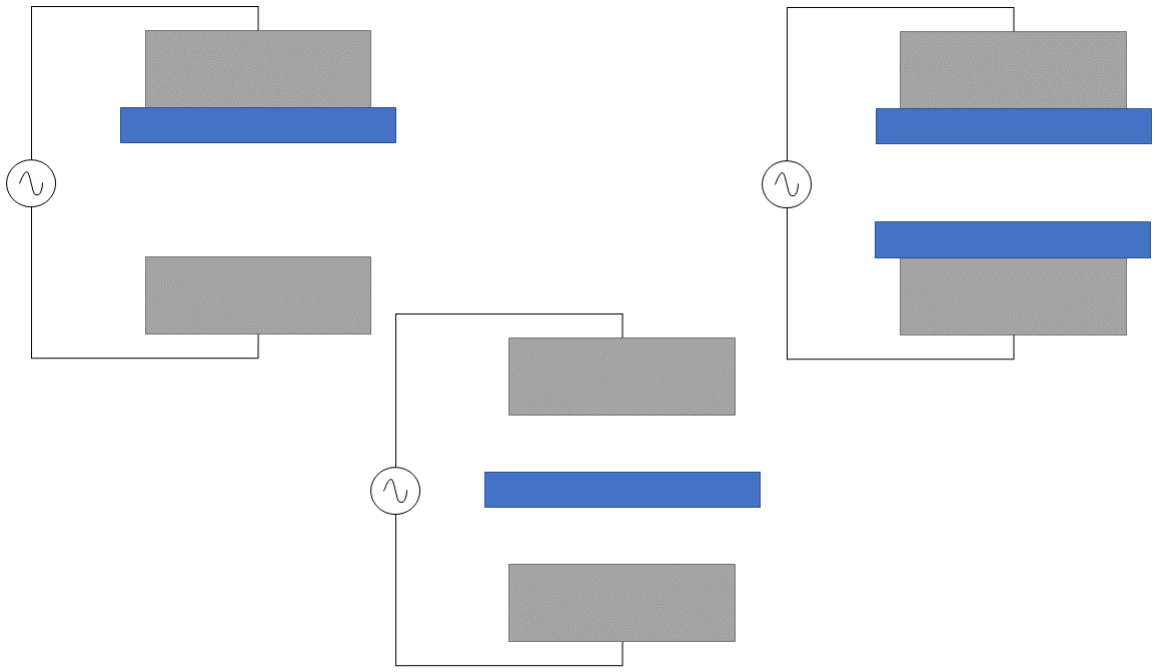

Figure 2.11: Typical electrode and dielectric material arraignments found in dielectric barrier discharges.

conductive channel is bridged across the gap and subsequent charge accumulation on the dielectric surface reduces the local electric field to such an extent that ionization stops within a few nanoseconds, choking the micro-discharge.

Typical dielectric media used in DBDs are quartz, glass, ceramics, enamel, mica, plastics, silicon rubber and Teflon [90]. Discharge gaps range from 0.1 - 10 mm and require moderately high voltage amplitudes and due to the capacitive nature of the discharge arrangement, alternating or pulsed high voltages are used, with voltages ranging from 1 - 100 kV_{rms}. Typical DBD electrode configurations are shown in figure 2.11.

2.5.3 Atmospheric pressure plasma jet

DBDs have many modern applications, but their usefulness is somewhat limited for applications that cannot be treated between the electrodes of the DBD system [43,66]. Atmospheric pressure plasmas jets (APPJs) are a solution that allow a more versatile alternative by allowing the delivery of excited species to locations beyond the confines of the electrodes.

A plasma is typically struck within the confines of a cylindrical tube through the application of RF [91], pulsed DC [92,93] or kHz [94–96] driven inner or outer electrode while the other electrode remains grounded and through the use of noble gases [97–99], air [100–102] or other gas admixtures. Typical APPJs electrode arrangements are shown in figure 2.12 [103], that can be subdivided into two category's: those where the applied field is perpendicular to the gas flow known as cross field and those where the applied field is parallel to the gas flow known as linear field [104]. Linear configurations typically have a more reactive chemistry and higher electron temperature [104]

The most useful feature of APPJs is their ability to introduce plasma excited species to substrates far away from the source of excitation. This opens up the possibility of many applications for APPJs that require non-thermal chemical treatment such as medicine [20,45,105–107], sterilization [108,109], food [110] and animal tissue treatment [111, 112].

The plasma produced by APPJs appears to be continuous, but is actually formed by either one or a number of discrete breakdown events, known as plasma bullets, that propagate at hypersonic speeds through the jet, and can be imaged while using a high

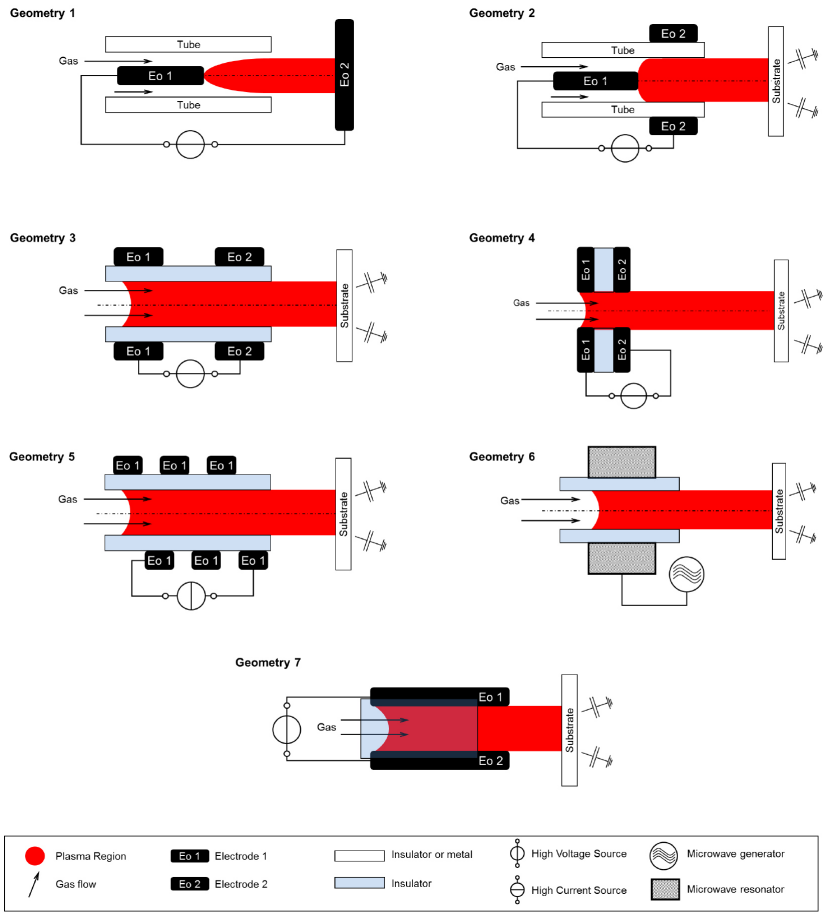

Figure 2.12: Typical APPJ electrode configurations.

speed camera [113]. This structure of the jet has been attributed to the streamer like mechanism as previously described [114].

As with DBDs, APPJs discharge breakdown, structure and chemical reactivity are sensitive to the type of high voltage excitation [104, 114–116], gas flow and gas composition [115–117, 117].

2.6 Physical and chemical process due to gas breakdown

Gas breakdown leads to the production of a large variety of atomic and molecular, ionic and excited species. The production of these species may be used in physical and chemically reactions that are not possible through conventional means.

Electronic and Atomic or Molecular reactions		
Reaction	Description	Number
$e^-_{fast} + A_{slow} -> e^-_{slower} + A_{faster}$	Elastic collision	(1)
$e^- + A -> e^- + A^*$	Excitation by electrons	(2)
$e^- + A -> e^- + A^+ + e^-$	Electron impact ionisation	(3)
$e^- + A^+ -> A$	Electron - ion recombination	(4)
$e^- + A -> A^-$	Electron attachment	(5)
$e^- + A_2 -> A^- + A$	Dissociative attachment	(6)
$e^- + A_2 -> A^+ + A + e$	Dissociative ionization	(7)
$A^* or A^+ + B -> A + e^-$	Secondary electron emission	(8)
$e^- + A_2 -> A_2 + 2e^-$	Detachment	(9)
Atomic, Molecular and Photonic reactions		
Reaction	Description	Number
$M^* + A_2 -> M + 2A$	Penning dissociation	(10)
$M^* + A_2 -> M + A_2^+ + e^-$	Penning ionization	(11)
$M^\pm + A -> M + A^\pm$	Charge transfer	(12)
$M^- + A^+ -> MA$	Ionic recombination	(13)
$h\nu + A -> e^- + A^+ or A^*$	Photo-ionization or excitation	(14)

A summary of the most important physical and chemical processes in given in table 2.6. The number of physical and chemical processes in a plasma can be enormous and should not be considered exhaustive. The reactions are not only important for the production of chemically reactive species but also for the propagation and stability of the discharge itself.

2.7 Conclusions

In this chapter a review of the major features associated with plasmas has been presented. The onus has been to develop a fundamental understanding of the physics and processes involved in plasmas, specifically regarding those at atmospheric pressure. Initially a brief overview of plasma formation was developed and then expanded to suit the needs at atmospheric pressure. This was done with an eye on future chapters, to allow a full explanation of work carried out

The difference between a thermal and non-thermal plasma was explained and detailed regarding the difference in temperature between electrons and the more heavier particles atoms, ions and molecules. The key parameters of that define a plasma: the Debye length, plasma frequency and plasma parameter were also discussed.

A description of the various forms of APPs was also presented including corona discharges, dielectric barrier discharges and finally atmospheric pressure plasma jets.

Finally a brief outline of the various physical and chemical processes that happen with a plasma were discussed. The purpose of this work and chapter was to present the basics of plasma physics.

3 Atmospheric Pressure Plasma Jet

For the purposes of this investigation, an atmospheric pressure plasma jet (APPJ) shown in figure 3.1, was designed and developed. The jet was based on work presented by Gogna *et al* [118], with several improvements, such as a variable power supply and a transparent casing to allow optical diagnostics.

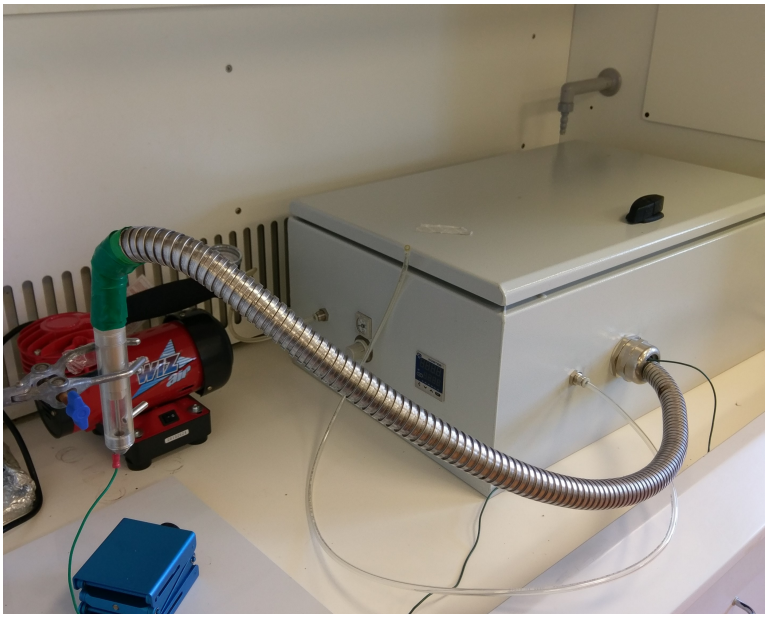

Figure 3.1: The atmospheric pressure plasma jet system used throughout this investigation.

The APPJ presented in this chapter is used throughout the main body of work of this thesis so a detailed description of the components that make up the APPJ is presented. Following this, an investigation into the electrical behaviour is given.

3.1 Jet Design

The jet used to generate a plasma is shown in figure 3.2 and is similar to those described in [119]. The jet is constructed of a 100 mm length outer plastic tube, with an inner diameter of 18 mm and outer diameter of 20 mm. A 5 mm hole cut into the side of the tube allows for gas to be introduced to the jet chamber. A Teek capsule held in place at one end of the plastic tube extends 40 mm into the tube.

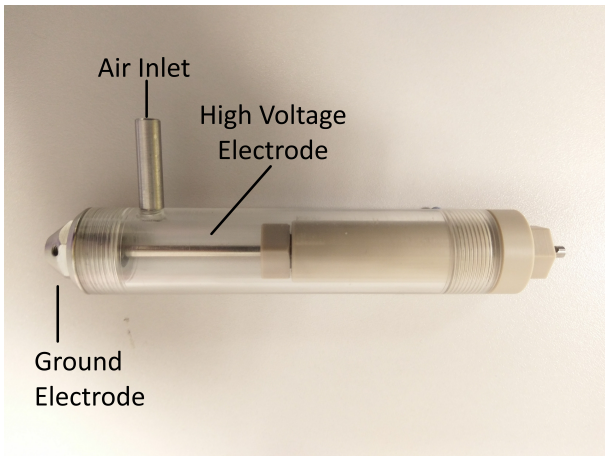

Figure 3.2: Atmospheric pressure plasma jet used throughout to generate plasma. Shown are the ground and high voltage electrodes and air inlet.

Two stainless steel electrodes provide electrical power to the jet. The first electrode, a nozzle as shown in figure 3.2, is fixed in place within the plastic tube and electrically grounded. The interior of the nozzle electrode is conical in shape, with a small 0.6 mm hole at the bottom to allow airflow out of the jet chamber.

The second electrode, a pin as shown in figure 3.2, is electrically connected to the high voltage line. The pin is held in place by the Teek capsule and may be moved further or closer to the ground electrode.

Plasma is generated between the pin and ground electrode when a sufficiently high voltage is supplied as shown in figure 3.3 (a) and excited species are transported out of the jet chamber to the plume region as shown in figure 3.3 (b). Figures 3.3 (a) and (b) also show the two main regions of interest while discussing the plasma, in part (a) the plasma region located within the jet between the two electrodes and the plume or afterglow region located outside the APPJ in contact with the ambient.

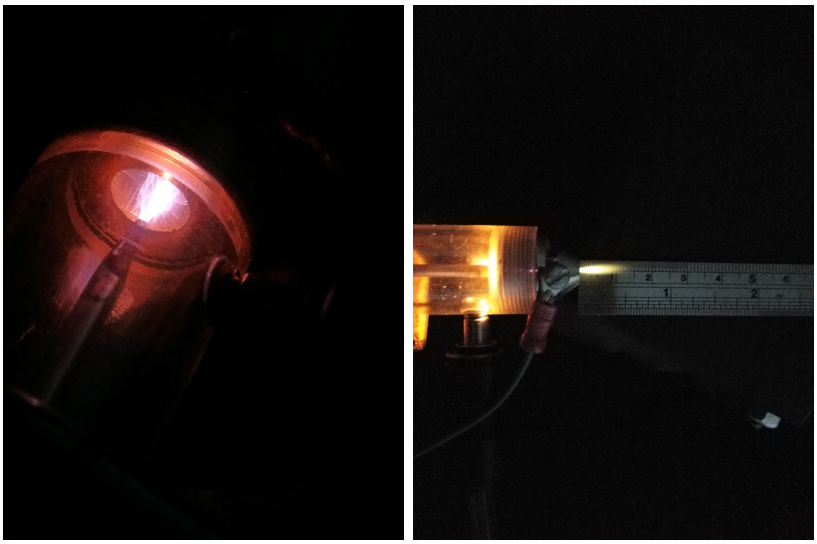

Figure 3.3: (a) Example of plasma produced by Atmospheric Pressure Plasma Jet. (b) Example of the plume region outside the plasma chamber.

3.2 High Voltage Power Supply Unit

To generate a plasma within the jet chamber, high voltage must be supplied between the pin and the ground electrodes. In the case of air, the breakdown voltage has been found to be approximately 20 kV based on standard atmospheric conditions. To produce such high voltages, a *PVM500* high voltage power supply, shown in figure 3.4

is utilised in the system.

The high voltage PSU provides variable voltage from 0 - 20kV pk-pk at frequencies from 20 kHz - 70 kHz. In addition, the power supply allows control over duty cycle, current and frequency monitoring and the capability to double the voltage. Power is supplied to the *PVM500* from mains through a 220/110 V step down voltage converter.

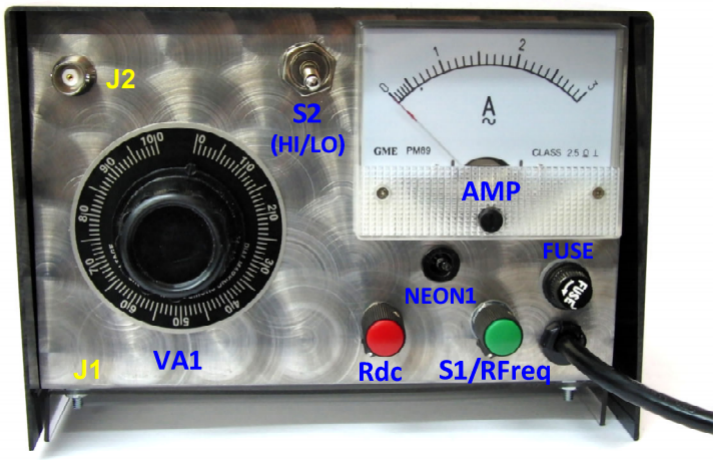

Figure 3.4: *PVM500* high voltage power supply front panel showing control systems: VA1: Voltage control, S1/RFreq: frequency control, S2: HI/LO voltage doubler, Rdc: duty cycle control, NEON1: Power on indicator, AMP: ammeter, FUSE: 4 amp slow blow fuse, J1: Frequency monitoring port, J2: Remote control port.

The *PVM500* power supply has two outputs: (1) high voltage power line and (2) high voltage return line or ground. Line 1 is connected to the pin electrode through an insulated coaxial high voltage cable and line 2 is connected to the nozzle electrode creating a capacitive load between the two electrodes when no plasma has been formed been formed and a resistive load when a plasma is formed. An electrical schematic of the APPJ is shown in figure 3.5.

Figure 3.5: Schematic representation of the atmospheric pressure plasma jet. Shown is the mains power supply, 220/110 V step down converter, *PVM500* high voltage power supply, high voltage cable, pin and nozzle electrodes.

3.3 Airflow Control

The primary gas used throughout is air, composed of approximately 78 % N_2, 21 % O_2 and 1 % Ar and various other trace amounts (CO_2, water vapour, etc.). Since, the jet chamber and the gas source are at the same pressure, approximately 1 atm, an airflow control system is required to pump air through the system at a controllable rate. A schematic representation of the airflow control and components is shown in figure 3.6.

Figure 3.6: Schematic diagram of the air flow and components used in the plasma system

Air is initially supplied to the plasma system by the *Clarke air WIZ - Mini Air compressor*. The air compressor supplies a constant 11 L/min of air to the system from the ambient environment. From the *Clarke air WIZ - Mini Air compressor*, air is passed to an air regulator that stabilises the air flow, followed by an air filter that removes large particles and oils from the air. A Mass Flow Controller (MFC) allows final control of the air flow, from 0 L/min up to 11 L/min in 0.1 L/min increments,

finally passes the air into the jet chamber at the desired flow rate.

For larger air flows than possible from the *Clark air WIZ - Mini Air compressor* air was supplied directly from a mains laboratory air tank. This allowed air flows up to 20 L/min, while still passing through the air control system.

3.4 Electrical Characterisation

Electrical measurements were preformed to determine the current voltage characteristics of the APPJ while varying conditions related to the Paschen relation Pd, voltage, airflow and the distance between the two electrodes. A schematic representation of the experimental set-up is shown in figure 3.7.

Current measurements were preformed using a *Pearson 8181* current monitoring probe. The probe has a 1:1 volt/amp relation and is possible to measure up to a peak of 500 A. The probe was attached to the cable connecting the ground electrode to the HV PSU. Current flowing through the ground wire induces a current in the probe that is measured while connected to an oscilloscope.

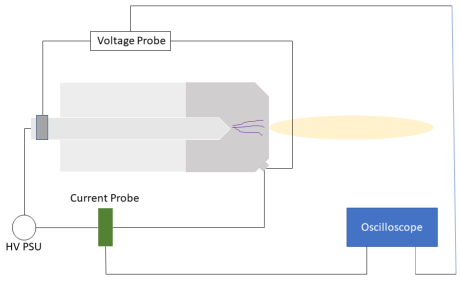

Figure 3.7: Schematic representation of the electrical characterisation experiment.

Since the power supply delivers an AC voltage, the direction of the current is

dependent on the initial orientation of the probe. For consistency throughout, the probe was orientated in such a direction that the arrow on the probe, was the same direction that current would flow while the voltage between the ground and high voltage electrode was positive. Changing the orientation of the arrow on the probe resulted in the phase of the current changing by 180^o.

Throughout the investigation it was discovered that the current spikes created by the plasma were relatively large, on the order of 10s of A, so a 3 dB attenuator was attached to the current probe between the probe and the oscilloscope.

Voltage measurements were preformed using a *Tektronics P6015A* high voltage probe. The probe has an attenuation factor of 1000x and a maximum input voltage of 20 kV. Measurements were made by attaching one end of the probe to an exposed part of the high voltage electrode while the ground connection was attached to a screw placement on the ground electrode. A BNC connection was then made to the oscilloscope.

The oscilloscope was triggered off the current spike generated when the plasma was active. This was achieved by the setting the time division on the oscilloscope to 100 ns and adjusting the trigger level of the oscilloscope to be approximately 60 % of the current reading, giving a stable reading for both current and voltage. The averaging of the oscilloscope was then set to 64 and measurements were made.

Due to the large differences in scale between on voltage cycle, approximately 500 ms, and one current spike, approximately 20 ns it was not possible to record the voltage waveform and the current spike simultaneously. Instead the current spike and voltage

drop were measured at once, and after the time setting was adjusted and voltage was then recorded, see figure 3.9 for an example.

Initially three distinct modes of operation were observed: (1) a non-plasma mode before electrical breakdown, the system behaved like an RC circuit. (2) A quiet mode, so named as the jet was audibly noted to be quiet. Electrically this was significant due to a single current pulse and corresponding voltage drop. (3) A noisy mode, again so named due to being audibly noisier than the quiet mode and electrically significant due to two distinct current pulses and corresponding voltage drops per cycle.

The voltage waveforms of each mode of operation are shown in figures 3.8 (also shown is the current), 3.9 and 3.10. In the case of the non-plasma mode the voltage and current waveform follow a sinusoidal pattern with the voltage lagging the current, see figure 3.8. In the case of the quite mode of operation, the voltage waveform approximately resembles a distorted sine wave for the positive half cycle of the pulse, however for the negative half cycle the voltage drops. In the case of the noisy mode of operation, the waveform has two voltage drops, one in the positive half cycle and the other in the negative half cycle.

3.4.1 Non-Plasma Mode

When insufficient voltage is supplied to the gas for breakdown to occur, the electrical behaviour is that of a capacitive load. Both the current and the voltage signals have sinusoidal waveforms, with the current leading the voltage. The period of both the current and voltage was measured to be 51.2 μs corresponding to a frequency of 19.5 kHz meaning a slight deviation between the measured frequency and the HV PSU

expected frequency of 20 kHz. In an ideal capacitative load the voltage should lag the current by 90°, which should for the case of a period of 51.2 μs should be 12.8 μs, however the calculated phase difference was found to be 8.4 μs corresponding to a phase difference of approximately 60°.

An example of the current and voltage measurements taken are shown in figure 3.8.

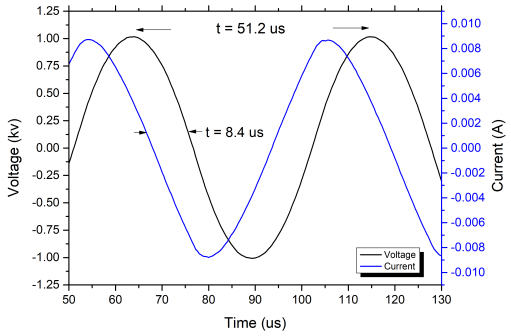

Figure 3.8: An example of the current and voltage signals measured when no plasma is active. While no plasma was active both the current and voltage behaved sinusoidally. The period of each wave was determined to be 51.2 μs and the phase difference between the current and voltage was also determined to be 8.4 μs.

3.4.2 Quiet Mode

When a sufficient electric field is applied between the electrodes, the gas was able to breakdown and switched from a capacitive load to a resistive load. Two distinct modes were electrically observed, the quiet and the noisy modes.

The so called quiet mode was named due to the audible behaviour of the plasma when active. When in this mode, the jet had a quiet hiss to it when compared to the noisy mode that had a more erratic, chaotic sound.

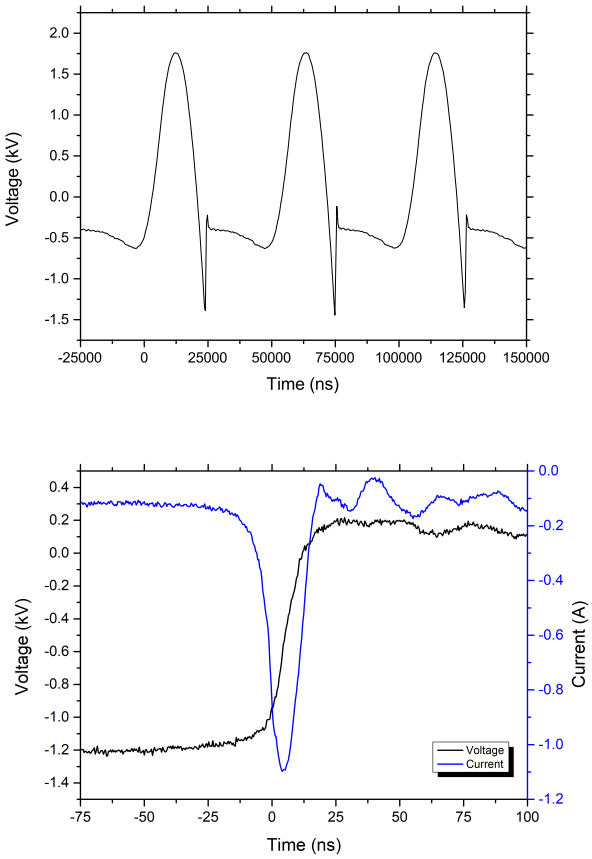

Figure 3.9: (a) An example of the voltage signal observed when the plasma was in the quiet mode. (b) An example of the corresponding voltage drop and current spike.

Figure 3.9 (a) shows an example of the voltage waveform of the quiet mode of operation over three voltage periods, while figure 3.10 (b) zooms in on the voltage drop seen in figure 3.9 and shows the corresponding current spike.

There are several distinct features that distinguish the quiet mode of operation. During the negative half cycle, the voltage experiences a sharp drop in magnitude with a corresponding sharp, short current spike typically in the order of 1 - 3 A with a duration of 25 ns. During this voltage drop, the polarity of the voltage was seen to reverse from negative to positive once the current spike had ended. After the voltage

drop and polarity reversal, the voltage quickly reversed polarity again to negative and proceeded to have a long plateau that typically extended into when the polarity of the applied voltage should have changed to positive. Depending on the operating conditions of the APPJ, the plateau would remain relatively flat between 300 - 400 V or gradually increase over the length of the cycle, or becoming more pronounced and increased in magnitude towards the end of the negative half cycle as the polarity of the applied voltage began to change.

During the positive half cycle, the voltage waveform was distorted and temporarily reduced in length, typically 20 μs in length. There was no observed voltage drop or current spike.

3.4.3 Noisy Mode

The so called noisy mode of operation was characterised electrically by one current spike per half cycle and a corresponding voltage drop as shown in figure 3.10 (a). Figure 3.10 (b) shows a zoom in of the positive current spike and voltage drop and figure 3.10 shows the corresponding zoom in of the negative current spike and voltage drop. The negative current spikes were similar to those detected in the quite mode, approximately 20-25 ns in duration and ranging from 1 - 3 A. However the positive current pulses were typically larger, in magnitude, ranging from 3 - 5 A.

Like the quiet mode of operation, the noisy mode has some distinct features, not least of which is the appearance of a current spike during each half cycle of the voltage period. During the negative half, the voltage drop observed is similar in magnitude and duration and also features a short reversal in voltage polarity. However, unlike

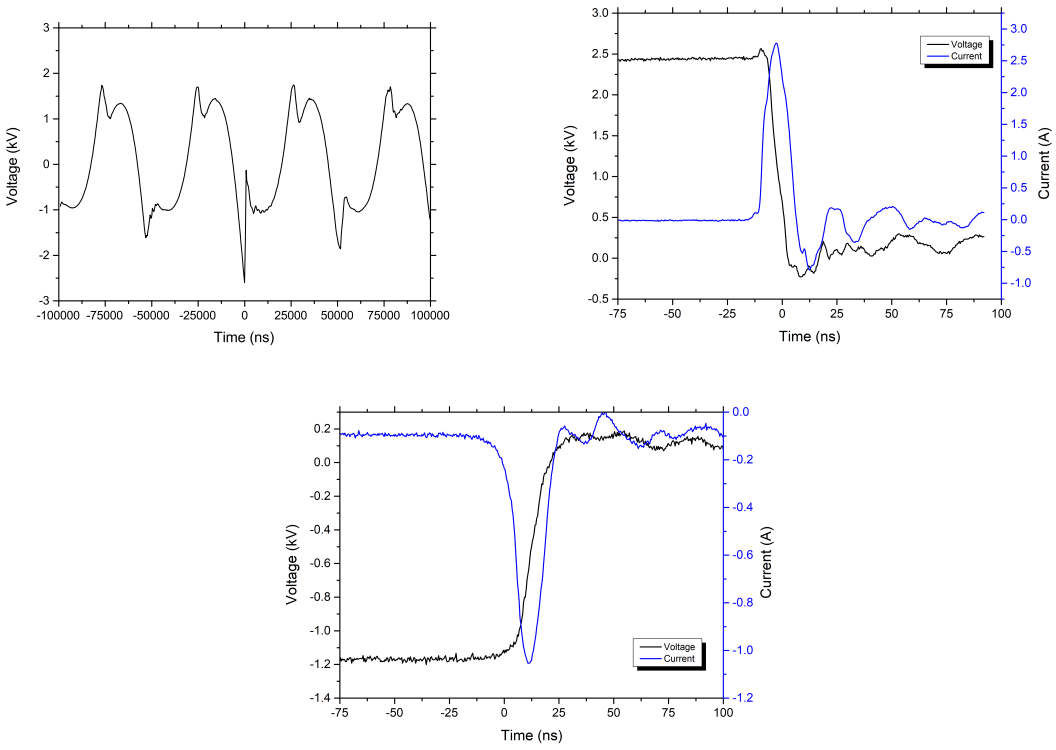

Figure 3.10: (a) An example of the voltage signal observed when the plasma was in the noisy mode. (b) Example of the positive voltage drop and current spike. (c) Example of the negative voltage drop and current spike.

the quiet mode that featured a long plateau after the voltage drop, the noisy mode of operation has more rounded appearance after the voltage drop for both the negative and positive half cycles and is also shorter in duration, tending to end before the applied voltage reverses polarity. On the positive half cycle, the voltage dropped to zero but did not reverse polarity. The waveform distortion also tended to be more rounded, rather than flat, and shorter in duration than the negative half cycle.

3.5 Results and discussion

3.5.1 Electrode position

It was possible to alter the position of the pin electrode relative to the ground electrode. The pin electrode could be slide in and out of position and fixed in place. At its closest the gap between the pin and ground electrode is approximately 2 mm. This corresponds to the pin electrode protruding 5 mm from the end of the Teek tube and all measurements were taken relative to this position, designated position one for this purpose. At distances greater than 12 mm from this position stable and continuous plasmas were difficult to achieve as the electric field strength became too weak to ignite the discharge. Measurements were therefore confined to a 1 cm region and taken at three different positions.

Initial measurements were taken with the voltage knob position set to 100 and with an airflow of 10 L/min. The voltage waveform was then measured at three electrode positions. Position 1 was as described before, position 2 was 5 mm further away from the ground electrode or level with the edge of the Peek tubing and position three a further 5 mm away from the ground electrode. The voltage waveforms measured are shown in figure 3.11.

While in position 1 the plasma was in the quiet mode of operation and as the powered electrode was withdrawn from the grounded electrode the behaviour transitioned to the noisy mode. The elongation of the negative plateau can clearly be seen in figure 3.11 while in position 1, extending into when the polarity of the applied voltage changes. As the powered electrode was withdrawn, the length of the plateau

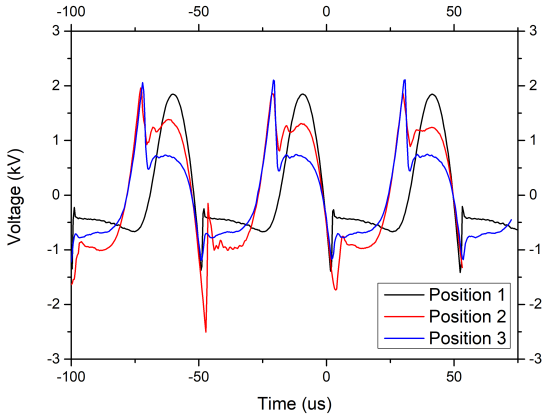

Figure 3.11: Voltage waveforms of the plasma at three different electrode positions.

decreased and became more rounded. During the positive half cycle, the magnitude of rounded part of the voltage distortion decreased as the distance between the ground and powered electrode was increased.

3.5.2 Voltage

The influence of voltage knob position was measured at each of the three electrode positions. It was noted that the behaviour of the plasma changed when the electrode positioning was altered as well as the voltage. The measurements were made in ten step intervals as per the dial interval on the power supply. The results of these measurements are shown in figure 3.12. Figure 3.12 (a) shows the voltage waveform in position one, (b) in position two and (c) in position three.

While in position one, the plasma remained in the quite mode of operation for all measurements made. At higher knob positions, the length of the plateau tended to increase and the plasma tended to ignite earlier into the cycle due to a larger electric field. The magnitude of the plateau region was similar for all measurements made and

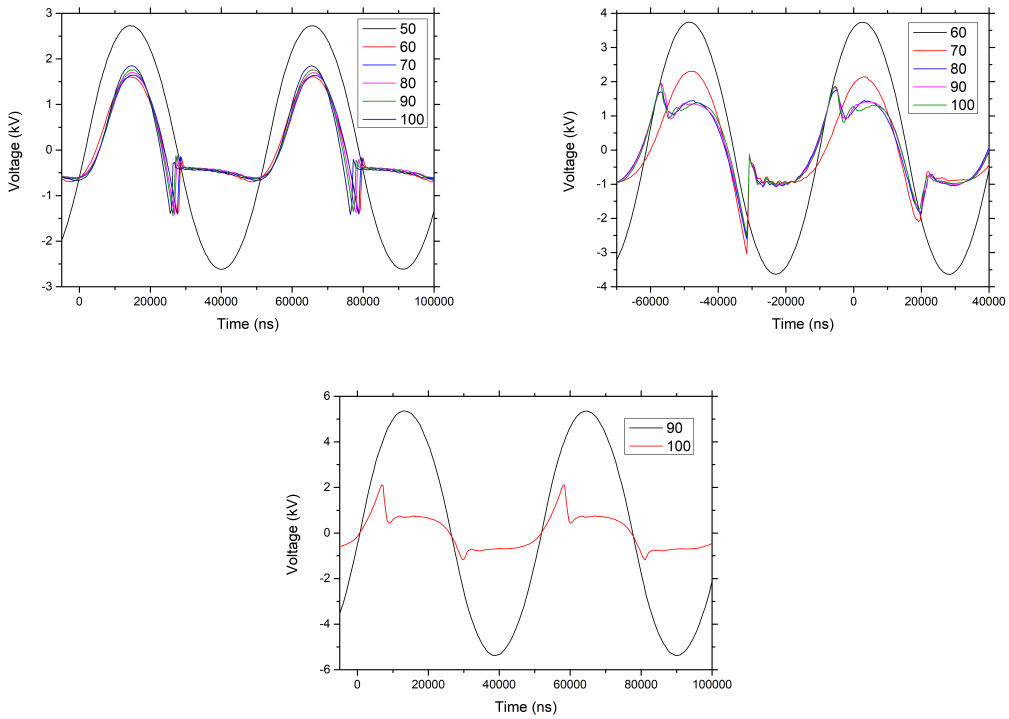

Figure 3.12: The voltage waveforms measured at position one while the plasma was active at different voltage knob positions. (a) Voltage waveform in position one. (b) Voltage waveform in position two. (c) Voltage waveform in position three.

sloped downward throughout the negative half cycle.

While in position two, it was observed that the plasma could transition between the two modes of operation based on the position of the voltage knob. At higher knob positions the plasma operated in the noisy mode and as the voltage was decrease eventually transitioned to the quite mode before extinguishing. In figure 3.12 (b) it can be seen that when the voltage knob was in positions 80 - 100 the voltage waveform remained relatively unchanged, but when it was decreased to 70 the plateau region became elongated and extended, causing the plasma to transition to the quiet mode. Shown also is the voltage waveform of the while the voltage knob was in position 60

just before breakdown.

While in position three it was only possible to ignite the plasma while the voltage knob was set to 100 %. When in this position the plasma was typically unstable and difficult to maintain. While in this position the applied voltage was largest before breakdown occurred. This is believed to be due to the decrease in electric field due to the increased distance between powered electrode and ground electrode.

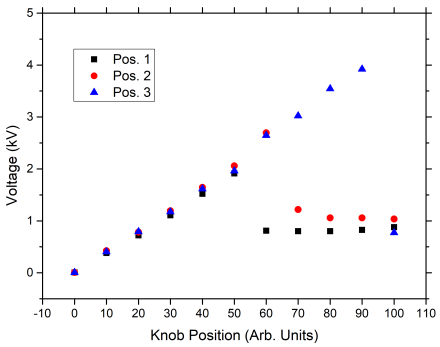

Figure 3.13: Calculated RMS voltages of the plasma in each electrode position.

The values of the RMS voltages were calculated for each position and are shown in figure 3.13. As can be seen, the values remain relatively invariant based on the position of the electrodes, although the plasma does breakdown at different applied voltages, indicating that the electric field strength reduces as the powered electrode is pulled further away from the ground electrode.

3.5.3 Airflow

The influence of airflow was also tested while the the electrode was in position one and the voltage set at 100. Voltage measurements were taking in 2.5 L/min intervals

ranging from 5 L/min to 20 L/min. To achieve these greater airflows, the APPJ was attached to a laboratory air gas tank and all measurements were taken using this air source. In addition to voltage measurements, a closer look into the current behaviour was also made. This was achieved by reducing the time constant on the oscilloscope to 10 ns/division making it possible to see the behaviour of the current spikes. It was not possible to make these measurements in parallel however due to the vast differences in time scales. The current spikes lasted 10s ns while the period of the voltage was in the ms range.

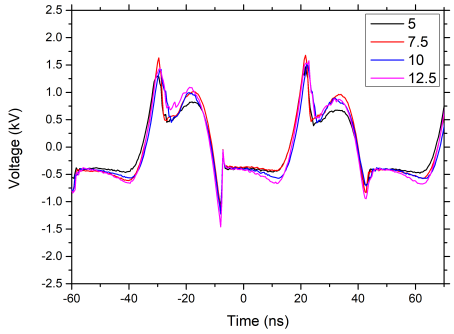

Figure 3.14: Voltage waveform while varying the airflow through the APPJ at low airflows.

Figure 3.14 and 3.15 shows the resulting voltage waveforms. The results are divided into two parts; lower voltages as seen in figure 3.14 and higher voltages in figure 3.15. This was in part due to the observed trends in the current measurements and to clarify the images.

At lower airflows, as shown in figure 3.14, the trend was for the plasma to behave in the noisy manner with the characteristics double voltage drop, relatively flat voltage after the drop during the negative half cycle and during the positive half cycle the

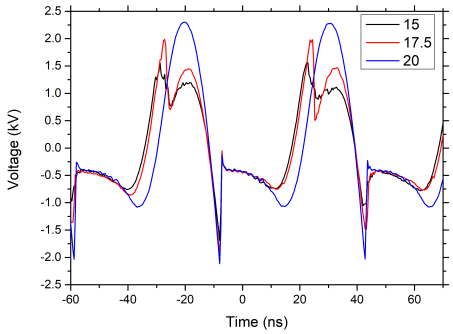

Figure 3.15: Voltage waveform while varying the airflow through the APPJ at higher airflows. At higher airflows the distortions in the voltage waveform became more pronounced before transitioning to the quiet mode

rounded rise and fall in voltage after the voltage drop. As the airflow was increased, at lower voltages there was little pronounced impact on the waveform distortion. The peak of the of the rounded part of the negative half cycle remained relatively stable, typically just below 1 kV, while the plateau in the negative half cycle did start to change as the airflow was increased. It can be seen in figure 3.14 that as the airflow increased the slope of the plateau became more negative, but also increase in length.

As the airflow was further increased these distortions became more pronounced and increased in magnitude towards the end of the negative half cycle. This also resulted in the duration of the plateau to increase. Finally when the flow rate was increased to 20 L/min the discharge transitioned to the quite mode. This could be seen as the further elongation and increase in magnitude of the plateau region, blocking the formation of the positive current spike.

Figure 3.16 shows the current waveforms measured while varying the airflow through the APPJ. In figure 3.16 (a) the positive current spike is shown which is typically large

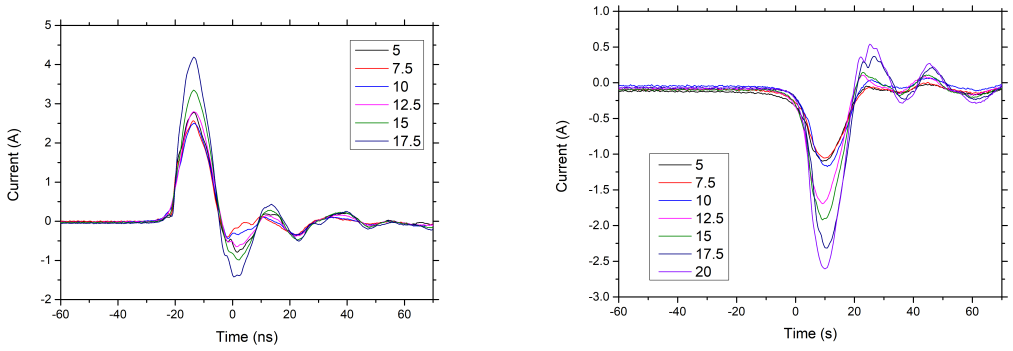

Figure 3.16: Meausured current waveforms for both (a) the positive current spike and (b) the negative current spike.

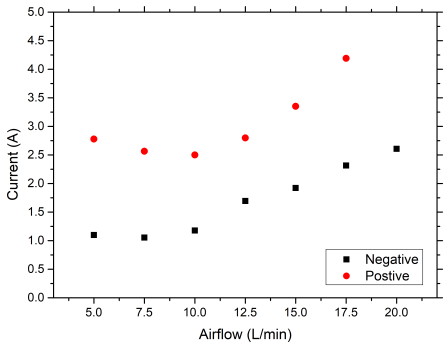

Figure 3.17: Current peak measured for each airflow condition, showing both the negative and positive peaks where applicable.

than the negative current spikes shown in figure 3.16 (b). In both cases the spikes have the same duration of 20 ns.

Figure 3.17 shows how the peak of each current spike varies as a function of airflow. As can be seen, the positive spikes were larger than the negative. There also appears to be two different phases. At lower airflows 5 - 10 L/min the discharge current remained stable as the airflow was altered, however as the airflow was increased beyond

a threshold, the current spikes increased in intensity.

3.6 Plasma formation

It is interesting to speculate on the plasma formation and electrical behaviour as it is unique. The behaviour is similar to that observed in [120]. In their work a voltage drop was observed in the negative half cycle of the voltage with a corresponding current spike, with a voltage peak of 3 kV and a current spike of 4.5 A over 80 ns, corresponding to 18 W. The geometrical layout of the APPJ was also similar to the APPJ presented in this work, with a central high voltage electrode surrounded by an outer ground electrode. In [120] they also claimed that because the current spike was short the dissipated power was low meaning the temperature remained low and it was possible to touch the afterglow. However they did not offer an explanation as to electrical behaviour or plasma formation.

Likewise, similar electrical behaviour was observed in [121], although the the current pulse and voltage drop was observed during the positive half cycle and not the negative. In their work [121], investigated mode transition in low pressure nitrogen discharge. They observed two modes, so-called G (presumably Glow) and self-pulsing (SP). The G mode had properties related to corona discharge and was easy to ignite in pure nitrogen. By increasing the input power the behaviour of the plasma switched to the SP mode and it was attributed to similar E-to-H transitions observed in cylindrical ICP sources reported in [122, 123] Similar, that as more power was coupled to the plasma, a behaviour change was noted, like the capacitive to inductive found in ICPs.

In the G mode, the voltage and current waveforms were both sinusoidal, and at the transition between the G and SP mode, the discharge waveforms became distorted along with random current pulses. Finally after the transition, extreme current pulses were observed as well as a large voltage fall and voltage waveform distortion, similar to that observed in this work. They also concluded that the G mode was capacitive, while the SP mode was resistive. They concluded that a feedback mechanism was promoting the G-to-SP transition and sustaining the discharge at the SP-mode discharge.

Similar electrical behaviour was also observed in He DBDs [121, 124–126]. Luo *et al* [126] investigate the transition from a Townsend to a glow discharge in a helium atmospheric discharge. They attributed the electrical behaviour as follows: as the current increased, more and more charged particles were produced in the gap. As the mobility of electrons is much greater than ions, a "swarm" of positive space charge is formed that moves towards the the cathode. This region of space charge distorts the the field distribution, causing field enhancement in the region between the cathode and the moving positive space charge, while at the same time causing a field decrease in the region between the anode and swarm. As a result the necessary uniform field is no longer present for a Townsend discharge. As the current was further increased, the positive swarm becomes stronger and closer to the cathode, before finally forming a cathode fall region, leading to a glow discharge. Finally, Luo *et al* concluded that it was possible to continuously adjust between the glow like and Townsend discharge by appropriate choice of dielectric barrier [127].

Similar work by Dai *et al* [124] involved a 1-D fluid model investigation into the

electrical behaviour of a He DBD while varying the gap distance. They found that all small gap distances, the discharge was symmetrical (SP1), however at distances greater than 0.97 cm, the behaviour of the discharge began to transition to an asymmetrical form, (AP1) donated by a discharge with the same period as the applied voltage, but with different shapes for both the positive and negative half cycles in a period.

At shorter gap distances the negative current pulse was larger, due to a larger gap width resulting in a lower electric field strength in the gap. When the negative current pulse was extinguished, the charged particle density in the positive column was relatively unchanged due to the weak electric field. A small particle density gradient in the positive column also greatly reduced drift, recombination and diffusion of charged particles. In the cathode fall region, the electric field decreases, causing the ion density to decrease, so after the negative current pulse is quenched, charged particle density is greatest in the in the positive column.

The charged particles near the left border of the positive column drift towards the original cathode fall region as a result of strong diffusion and since the electric field in the region of the original cathode is still large they will recombine quickly. This resulted in the gradual diminishing of the positive column from the left border after the negative current pulse has extinguished. This was found to be the case for all three positions measured, however for long distances, the positive column can last for a long time, even after the polarity of the voltage has been inverted.

In this case, i.e. distances greater than 0.97 cm, it was concluded that the residual positive column began to diminish from the right after the gas voltage is inverted.

Since the electrons move faster than the ions, a large space charge effect develops in the region close to the instantaneous cathode. While, at the left side of the column, the movement of electrons and ions was found to balance, greatly reducing the density disparity, resulting in a relatively low electric field in the region.

It was noted in [124] that non-uniform distribution of the electric field prior to the initiation of the next discharge will have a significant affect on the intensity of the discharge current density. At large distances, the positive discharge may ignite after the negative discharge so long as local electric fields near the instantaneous discharge is large enough. The current densities of these discharges are small, do not develop further and extinguish almost immediately due to the low electric field across the whole gap.

The electrical behaviour of the APPJ is unusual. The geometry would suggest that it should behave like a corona discharge, while the lack dielectric material should suggest that the discharge should transition to an arc, but the electrical behaviour does not fully support this. It may however be possible to unite these two scenarios as a possible means to understand how the APPJ behaves.

The behaviour of the plasma is asymmetric, indicated by the different behaviour of both the noisy and quiet modes of operation. This is believed to be the case for both modes. The asymmetry is manifested in a difference in both the shape and magnitude of the voltage measured and the difference in the current measured in both half cycles of the discharge.

In non-uniform field gaps, streamer formation is initiated in close vicinity to the

high electric field electrode. The streamer may then propagate farther away into the gap where the electric field is typically too low for streamer initiation, but due to it's own space charge field, high enough for streamer propagation.

3.7 Conclusions

In this chapter we have outlined and discussed the atmospheric pressure plasma to be used throughout this study. The device was based on previous APPJs, with modifications to improve the performance, adjustablity and allow more experiments to be carried out. These included the ability to control the voltage and electrode position, as well as a transparent casing to allow optical diagnostics.

The various components used to build the APPJ were discussed including the power supply and the electrode configuration. Preliminary observations about the APPJ performance revealed that the APPJ had two distinct modes of operation that were audibly identifiable and named accordingly as the quiet and noisy modes.

The structure of the plasma itself was divided into two regions of interest; the plasma itself, contained within the jet chamber between the pin and ground electrodes and the afterglow or plume region located outside the plasma chamber and in contact with the outside ambiance.

Electrical measurements revealed the RC nature of the systems performance before a plasma was formed as the current lead the voltage by 90 degrees. Once a plasma was formed the two distinct modes already identified audibly were noted to have distinct voltage waveforms. In the case of quiet mode, a single voltage drop was observed at

each negative half cycle of the power cycle, with a corresponding current pulse. In the case of the noisy mode of operation two voltage drops were observed per power cycle. Further observations revealed that the magnitude of the current pulses were also asymmetric, with the positive pulses being larger.

Before the plasma was ignited, the current and voltage waveforms were both sinusoidal with the current leading the voltage indicating a capacitive load. Increasing the voltage knob position lead to a linear increase in the RMS value of the voltage signal until the plasma ignited were it was found that the RMS voltage value remained stable at 750 V. A similar trend was also observed for current.

Finally, an attempt to explain the observed electrical behaviour based on existing theories and observations from other plasma sources. It is the belief that the electrical phenomena observed are based on the electrical current being self limiting due to large induced space charge build up between the electrodes causing the electric field between the electrodes to reduce to zero thereby limiting the current and preventing the transition to an arc, although the true cause of this is unknown

4 Optical Emission Spectroscopy of the Atmospheric Pressure Plasma

Spectroscopy is the study of the interaction between electromagnetic radiation (light) and matter. Spectroscopy is a powerful tool used in plasma diagnostics. At the astronomical level spectroscopy can provide detailed information about the composition of stars, nebulae and solar planets, while in the laboratory spectroscopy can be used to determine the populations of excited species and temperatures of the gas.

While discussing spectroscopy in the context of plasmas there are two types that are typically refereed to: (1) emission and (2) absorption.

Emission spectroscopy refers to when electromagnetic radiation is emitted by the plasma, and is recorded, spectrally resolved, analysed and interpreted in terms of the parameters of the plasma or characteristic parameters of the radiating atoms, ions or molecules. Emission spectroscopy is usually very straight forward since only a small viewing port is required to measure a spectrum. One draw back to this approach is that the measurement is inherently line of sight dependent.

Optical emission spectroscopy (OES) is a non-invasive method, meaning the plasma can be probed without interfering with the plasma, while also providing information regarding the temporal and spatial behaviour of the plasma.

On the other hand, absorption spectroscopy refers to when radiation is directed through the plasma and the resulting modification of the spectrum of the transmitted radiation by either through absorption or scattering, contains information about the plasma and its constituents.

4.1 OES principle

The basic underlying process of OES is outlined in figure 4.1. A particle (atomic, molecular, ionic) is excited, typically by direct electron impact from its ground level g to an excited level p. A spectral line is emitted when a bound electron undergoes a transition from an upper energy level (p) with energy $E(p)$ to a lower level (q) of energy $E(q)$.

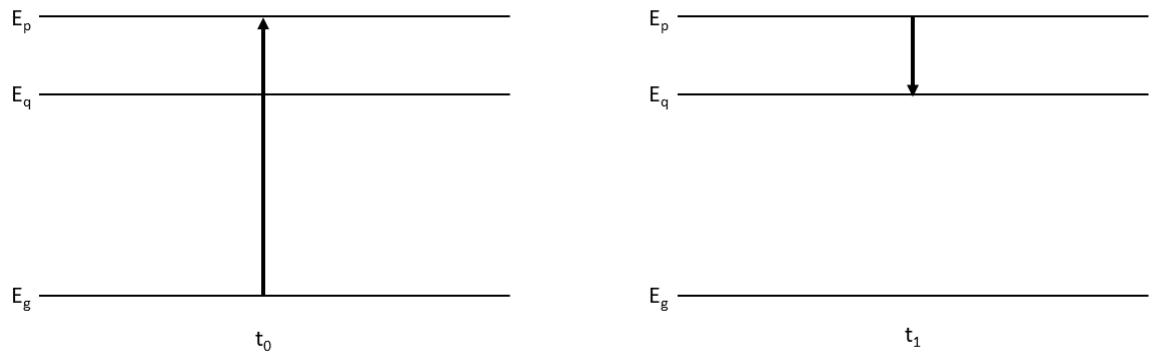

Figure 4.1: Energy level diagram of the optical emission spectroscopy principle.

Conservation of energy gives the frequency of the line

$$\nu_{pq} = \frac{E(p) - E(q)}{h} \tag{4.1}$$

where h is Plank's constant.

The transition from the higher state p to lower state q is spontaneous and the decay is proportional to the density $n_z(p)$ of the species of charge (z) in the upper state:

$$-\left.\frac{dn_z(p)}{dt}\right|_{p\to q} = A(p \to q)n_z(p) \tag{4.2}$$

The constant $A(p \to q)$ is a characteristic atomic constant for that specific transition and is known as the atomic transition probability or Einstein coefficient of spontaneous emission. A photon is emitted with each transition and the emission coefficient ϵ of the line is given by

$$\epsilon(p \to q) = \frac{h\nu_{pq}}{4\pi} A(p \to q)n_z(p) \tag{4.3}$$

This equation reveals that the population densities $n_z(p)$ of the excited states of the atomic species are the quantities measured.

An example emission spectrum is shown in figure 4.2 outlining the key characteristics of an emissions spectrum. The central wavelength λ_0 is given by the photon energy $E = E_p - E_q$ corresponding to the energy gap of the transition from level p with energy E_p to the energetically lower level q, with h the Plank constant and c the speed of light.

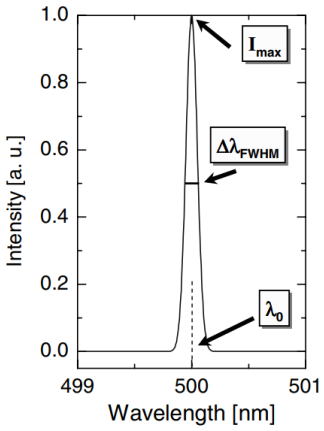

Figure 4.2: Line radiation and its characteristics.

$$\lambda_0 = \frac{hc}{E_p - E_q} \tag{4.4}$$

4.1.1 Atomic and molecular spectra

The electronic energy levels of atoms and diatomic molecules are represented in spectroscopic notation by:

$$nl^{w2S+1}L_{L+S} \tag{4.5}$$

and

$$nl^{w2S+1}\Lambda_{\Lambda+\Sigma^{+,-}_{g,u}\ldots} \tag{4.6}$$

respectively. Where n represents the main or principal quantum number, l is the angular momentum, w the number of electrons in the shell, S the spin, $2S+1$ the multiplicity, $L+S=J$ the total angular momentum.

Optically allowed transitions follow selection rules for dipole transitions. These are $\Delta L = 0, \pm 1$, $\Delta J = 0, \pm 1$, $\Delta S = 0$ for atoms and $\Delta \Sigma = 0, u \leftrightarrow s$ for molecules. $\Delta L = 0$ or $\Delta J = 0$ transitions are not allowed if the angular momentum of both states involved is zero.

4.1.2 Molecular emission

The combination of atoms into more complex molecules leads to the creation of more unique energetic states, each with their own unique spectra of transitions between states. Molecular spectra may be obtained from electron spin states, molecular rotations, vibrations as well as electronic states, of which vibrational, rotational and electronic are the most relevant for this study.

Molecules are more complex than atoms and therefore require a more detailed understanding. Molecules have a more complex structure, with electronic as well as vibrational and rotational excitations to consider. Each level (p) is represented by its electronic state n, vibrational v and rotational J.

The spectrum in the visible and ultraviolet regions corresponds to electronic transitions accompanied by a change in vibrational and molecular energies. Therefore the electronic spectra show up as electronic-vibrational bands which for each pair of vibrational levels consist of rotational lines from each different rotational branches (P-, Q- and R- branch). Emission between rotational levels of the same vibrational and electronic state are typically in the microwave region, and between vibrational levels in the infra-red, although they can be found in the near UV regions as is the case with nitrogen.

In molecular spectroscopy the convention is to mark the quantum numbers of the upper level with one prime and the lower level with two primes.

4.2 Dispersion

Light emitted from the plasma will contain photons from all possible transitions of species within the plasma, so in order to detect these individual photons, the light must be broken up into its constituent parts. This will depend on the wavelength of the light emitted and the region of interest. At the visible and near IR and UV regions this may be achieved by using a diffraction grating or a prism, to disperse the light based on its wavelength.

4.2.1 Diffraction grating

A diffraction grating is an optical component that is used to split and diffract light into several beams that travel in different directions. The direction of the output beam depends on the spacing of the grating and the wavelength of the light making the grating act as a dispersive element. Gratings typically come in two forms; transmissive and reflective. In practice reflective are the most commonly used, but the underlying principle is the same. The structure of the grating affects the amplitude or phase of the incident light, causing interference in the output wave.

In the transmissive case, the gratings can be considered as many tightly packed slits, which gives the general expression for diffraction with incidence angle ($\theta_i = 0$).

$$dsin(\theta_m) = n\lambda \tag{4.7}$$

where d is the slit spacing, θ_m the output angle and n the diffraction order. From equation 4.7 we can see that the output angle is wavelength dependent.

4.2.2 Transmission gratings

Transmission gratings are optically transparent for the region of interest whose surfaces are etched or scratched with thin parallel grooves. Light passing through the grating is dispersed at each individual slit, creating a diffraction pattern as the waves interact with each other. The dispersion angle is dependent on the wavelength of the light, the distance between the grooves d as per equation 4.7 but also on the incident angle which adjust equation 4.7 to

$$d\,[sin(\theta_m) - sin(\theta_i)] = n\lambda \tag{4.8}$$

where θ_i is the incident angle, although in most cases for transmission gratings this angle is close to zero.

4.2.3 Reflective gratings

Reflective gratings instead of allowing light pass through them reflect light by using a metallic surface again etched or scratched with grooves. Light is reflected off the ruled surface at different angles, corresponding to different orders, wavelengths and incident angle. Equation 4.7 is modified for reflective gratings to

$$d\,[sin(\theta_m) + sin(\theta_i)] = n\lambda \tag{4.9}$$

Both transmission and reflective gratings suffer from the same fact that zeroth order mode contains no diffraction pattern, appearing as a surface reflection or transmission. For example, the only possible solution to equation 4.8 when $\theta_m = \theta_i$ is $n = 0$. In this scenario no wavelength dependent information can be obtained and all light is lost as either a reflection or transmission.

A solution this is create a repeating surface pattern that produces a different reflection geometry. This type of grating is known as a blazed grating.

4.2.4 Blazed grating

Blazed gratings are a specific form of grating designed to produce a maximum grating efficiency for a specific diffraction order. The majority of the optical power will be in the designed diffraction order while minimising power lost to other orders, in particular the zeroth order. Due to their design, blazed gratings operate at a specific wavelength, known as the blaze wavelength.

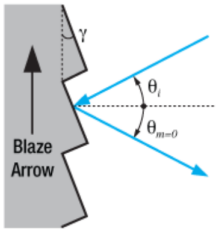

Figure 4.3: Blazed grating showing the key features.

The blaze wavelength is one of three characteristics of the blazed grating. The other two outlined in figure 4.3 are α, the groove spacing and γ the blaze angle. the blaze angle is the angle between the surface structure and the parallel surface and

simultaneously the angle between the surface normal and the facet normal.

4.2.5 Prism

Another technique used to disperse light is to employ an optical prism. Prisms were originally the main method used to disperse light but have largely been replaced by gratings, but still have some uses in spectroscopy. A prism works on the principle that light passing through a medium will travel at different speeds depending on the wavelength of the light and therefore bend at different angles.

The speed of light changes as it passes from one medium to another, causing the light to be refracted as it enters the new medium. The degree of bending while entering the new material depends on the initial angle, the angle of incidence, and the ratio of the two materials refractive indices. For many materials such as glass, the refractive index additionally varies based on the wavelength of the light. Meaning that light of different wavelengths will refract at different angles causing the light to disperse as it passes through the new medium. This phenomena is the bases for a prism to be used to disperse a white light source into its constituent spectrum of wavelengths.

4.3 Experimentation

OES measurements were taken in two regions: the plasma and the plume regions. The plasma measurements were taken looking in at an angle from outside the outer plastic tubing looking in to the active region, see figure 4.4 and the plume measurements were taken perpendicularly to the plume, see figure 4.5.

Measurements of the plasma region were made using an *Ocean Optics HR2000+*

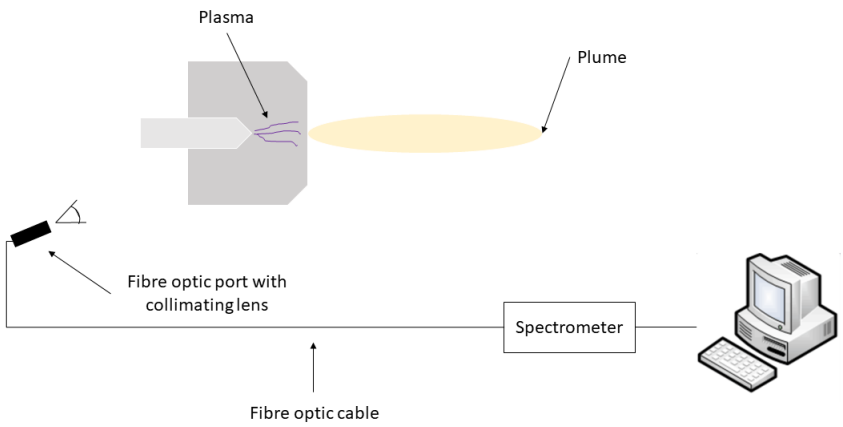

Figure 4.4: Experimental set-up for OES measurements taken of the plasma region of the APPJ

spectrometer. The optical resolution of this spectrometer was 6.8 nm (FWHM), with a spectral range of 190 - 1100 nm.

Light was coupled to the spectrometer using a collimating lens that was coupled to an SMA 905 single strand optical fibre with a 0.22 NA which acted as the entrance slit of the spectrometer. Light from the plasma was detected by the spectrometer using a *Sony ILX511B* CCD linear image sensor which contained 2048 pixels.

Data was collected using a PC connected to the spectrometer via USB 2.0 and visualised using *Ocean Optics Ocean View* software. Initially the electric dark field was corrected for using the software. The background signal was recorded and taken away from plasma measurements so as to only include light from the plasma source. The collimating lens was placed next to the plasma jet and held in place, while the plasma was ignited. The angle and position of the collimating lens was adjusted, so that

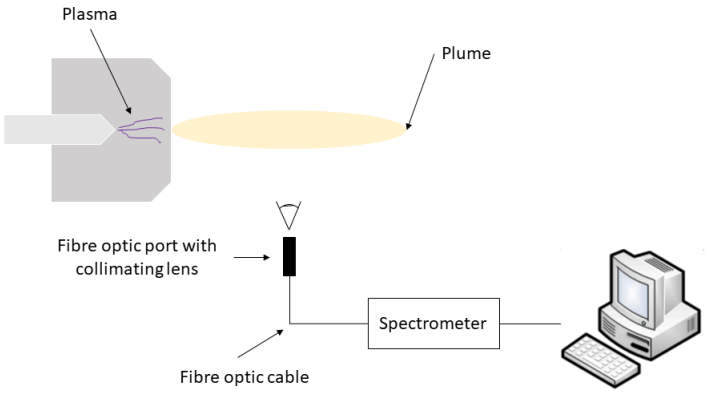

Figure 4.5: Experimental set-up for OES measurements taken of the plume region of the APPJ

the largest possible signal was detected. The acquisition time was adjusted to ensure the largest signal, without over saturation. This was determined by the magnitude of the largest peak in the spectrum being greater than 15000 counts/sec, but less than 17000 counts/sec. The acquisition time chosen was 100 ms. These conditions were kept constant throughout all experiments.

To record the spectrum, a high-speed acquisition was taken. Each acquisition was made up of five scans of the spectral range, using the acquisition time of 100 ms and each acquisition was taken five times. The average of these 25 scans was then taken as the spectrum of the plasma for each condition.

For the purposes of measuring the spectrum of the plume region of the plasma jet system, an *Ocean Optics Maya 2000 Pro* spectrometer was used. This spectrometer had a higher signal-to-noise ratio than the *HR2000+* spectrometer (450:1 vs. 250:1)

and was utilised due to the faint signal of the plume.

The optical resolution of the *Maya 2000 Pro* spectrometer was 7.4 nm (FWHM) with a spectral range of 200 - 1100 nm. Light was coupled to the spectrometer using a collimating lens and an SMA 905 single strand optical fibre with a 0.22 NA which acted as the entrance slit of the spectrometer.

Data was collected using a PC connected to the spectrometer via USB 2.0 and visualised using *Ocean Optics Ocean View* software. Electric dark field and background were corrected for so as to only include light from the plume. The collimating lens was placed with its axis perpendicular to the plasma plume direction and secured in place. Using the *Ocean View* software the acquisition time was adjusted until a strong signal was detected. The acquisition time used was 10 s.

To record the spectrum, a high speed acquisition was taken. Each acquisition was made up of five scans of the spectral range, using the acquisition time of 10 s and each acquisition was taken once. The average of these five scans was then taken as the spectrum of the plume.

4.4 Results and discussions

In figure 4.6 a typical spectrum obtained from the plasma used in this work is shown. The plasma was generated while the voltage was set to 100 % at the knob position, frequency of 20 kHz, air flow rate of 11 L/min and air as the working gas. The spectrum is dominated by two major spectral features; (1) a molecular spectrum due to the N_2 Second Positive System (SPS) located between 300 - 400 nm, and (2) atomic spectrum composing of atomic oxygen peaks at 777.4 nm and 844.6 nm, atomic nitrogen peaks at 745 nm, 821.6 nm and 869 nm, and the nitrogen First Positive System (FPS) between 600 - 800 nm.

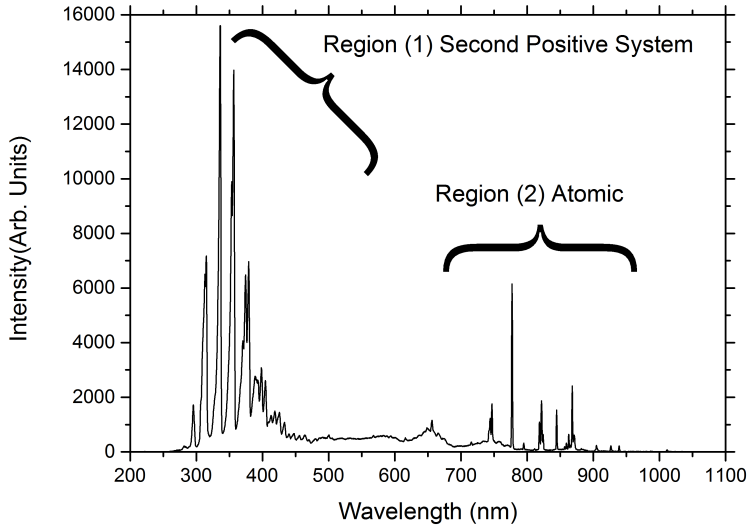

Figure 4.6: OES of air plasma obtained for a plasma frequency of 20 kHz and set to 100 % knob position.

The emission spectrum recorded reveals a lot of information about the plasma generated within the jet. Peaks provide both information about the type and quantity

of atomic and/or molecular species present within the plasma, while also providing information about the underlying processes involved in generating these species. As such we examine the spectrum in two regions: (1) between 290 nm and 410 nm as in figure 4.7 and (2) between 525 nm and 1100 as in figure 4.8.

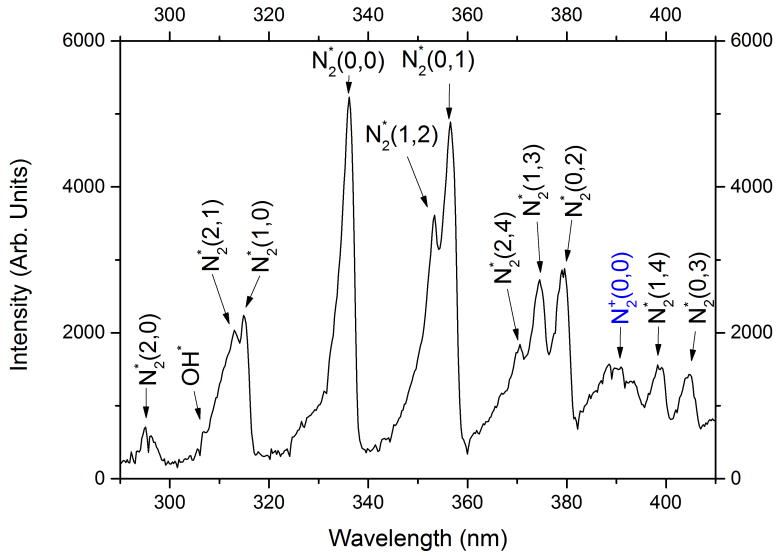

Figure 4.7: OES from 290 - 410 nm showing bands associated with the N_2 second positive system, N_2^+ first negative system and OH rotational band.

The most prominent features within figure 4.7 are peaks associated with the nitrogen SPS found between 300 - 400 nm. These peaks are caused by the radiative transition:

$$N_2(C^3\Pi_g) \longrightarrow N_2(B^3\Pi_g) + h\nu \tag{4.10}$$

caused by direct impact excitation of ground state molecular nitrogen by electrons. The SPS occurs through dipole allowed transitions between roto-vibronic manifolds of

the $C^3\Pi_g$ and $B^3\Pi_g$ states [128], whose allowed transitions and corresponding wavelengths are shown in Table 1 [6]. The strongest lines in the SPS occur at 337.1 nm, 353.6 nm and 357.7 nm, corresponding to the (0,0), (1,2) and (0,1) bands respectively. Note that due to the limited resolution of the spectrometer, peaks are broadened in some cases and form unresolved bands. Vibrational peaks can be resolved but rotational peaks are unresolved.

We also see evidence of the nitrogen First Negative System (FNS) highlighted in blue in figure 4.7. Positive ions of N_2^+ are produced by direct electron impact ionisation of the neutral molecule N_2 from its ground state $X^1\Sigma_g$.The FNS peaks are caused by the radiative transition:

$$N_2^+(B^2\Sigma_u^+) \longrightarrow N_2^+(X^2\Sigma_g^+) + h\nu \tag{4.11}$$

The FNS occurs through dipole allowed transitions between roto-vibronic manifolds of the $B^2\Sigma_u^+$ and $X^2\Sigma_g^+$ states of molecular ion N_2^+ [128], whose allowed transitions and corresponding wavelengths are shown in Table 2 [6].

Evidence of OH is also found in figure 4.7 shown as a shoulder at 306.4 nm as part of the $N_2^*(\Delta\nu + 1)$ band of the nitrogen SPS. This region is made up of emissions from the OH rotational transition:

$$OH(A^2\Sigma^+) \longrightarrow OH(X^2\Pi) + h\nu \tag{4.12}$$

and may explain the broad peak in this region. Using this OH band, it is possible to estimate the gas temperature (T_g) [7]. T_g may also be estimated from N_2 spectra

[129, 130] and O_2 spectra [131, 132]. However in both cases the spectrometer lacks the required resolution to produce meaningful results. OH production is caused by electron dissociation of H_2O leading to the production of H and OH by the reaction:

$$e + H_2O \longrightarrow e + H + OH \tag{4.13}$$

and by the excited state $O(^1D)$ dissociated by H_2O to generate OH

$$O(^1D) + H_2O \longrightarrow 2\,OH \tag{4.14}$$

The outer tubing material is optically opaque below 300 nm. Both OH and NO have emission bands in the UV region [7, 128] of the spectrum but could not be seen due to this. A different technique such as laser induced fluorescence is therefore required to determine if NO or OH are generated by the plasma.

Examining figure 4.8, which shows the spectrum between 500 - 1100 nm, we see emission lines associated with atomic oxygen, nitrogen and the FPS of molecular nitrogen.

The most prominent features in this region are peaks due to emissions from atomic oxygen. Table 3 outlines the expected transition lines of an oxygen based plasma [133]. When compared to the OES spectrum in figure 4.8, we observe lines at 615.9 nm, 777.4 nm, 844.6 nm and 926.6 nm relating to atomic oxygen. No transition lines relating to positively ionised molecular or atomic oxygen are observed.

Electron impact excitation of ground state molecular and atomic oxygen leads to

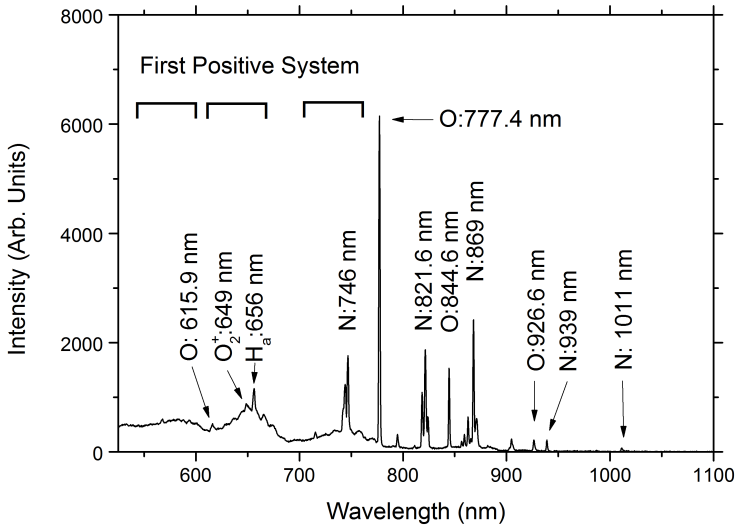

Figure 4.8: OES of the region between 525 - 1100 nm showing atomic nitrogen and oxygen emission lines and lines associated with the nitrogen first positive system.

the emission at 844.6 nm and 777.4 nm [134], which can be predicted by the following mechanisms:

Dissociative excitation

$$e + O_2 \longrightarrow e + O^* + O \tag{4.15}$$

and direct impact excitation

$$e + O \longrightarrow e + O^{**} \tag{4.16}$$

where O^* refers to the $O(3\,p^5P)$ state that emits at 777.4 nm and O^{**} to the $O(3\,p^3P)$ state that emits at 844.6 nm [135].

Also caused by direct electron impact excitation of molecular nitrogen is the first positive system (FPS). The FPS is due to the following radiative transition:

$$N_2(B^3\Pi_g) \longrightarrow N_2(A^2\Sigma_u^+) + h\nu \tag{4.17}$$

and is also caused by dipole-allowed transitions bewteen roto-vibronic manifolds of the $N_2(B^3\Pi_g)$ and $N_2(A^2\Sigma_u^+)$ states [128]. The FPS is a much more complex system than the SPS; further details of this system can be found in [128].

Lines associated with atomic nitrogen are also seen in figure 4.8. These lines are at 746 nm, 821 nm, 869 nm, 939 nm and 1011 nm, and are made up of complex multiplet peaks whose wavelength values and transitions are tabulated in Table 4 [11]. The lines found at 746 nm make up a triplet due to the:

$$3\,s^4P \longrightarrow 3\,p^4S^0 \tag{4.18}$$

transitions of atomic nitrogen [136–138]. Lines found at 821 nm make up a seven-line multiplet of peaks due to the:

$$3\,s^4P \longrightarrow 3\,p^4P^0 \tag{4.19}$$

transitions in atomic nitrogen [136–138]. The lines found at 869 nm form an eleven peak feature, from 856 nm to 872 nm. Two atomic transitions are responsible for these transitions. The first, a four line multiplet of peaks from 856 - 866 nm is due to the:

$$3\,s^2P \longrightarrow 3\,p^2P^0 \tag{4.20}$$

transitions in atomic nitrogen [136–138]. While the second form an eight line multiplet of lines associated with the:

$$3\,s^4P \longrightarrow 3\,p^2D^0 \tag{4.21}$$

transitions in atomic nitrogen [136–138].

The hydrogen emission is shown in figure 4.8 at 656 nm caused by electron impact excitation and the following transition [11]:

$$H(1\,s) + e \longrightarrow H^*(n{=}3) + eH^*(n{=}3) \longrightarrow H^*(n{=}2) + h\nu \tag{4.22}$$

4.4.1 Voltage Measurements

OES measurements were taken over a range of voltages by varying the position of the voltage knob. Starting at voltage position 100, the spectrum was recorded, and then the knob position was decreased in 10 step intervals until the plasma extinguished. The results of these measurements are shown in figure 4.9. The emissions go through a trend whereby they typically peak when the voltage is typically set to 70 %.

To show these trends various emission lines were monitored at each voltage position. These were the nitrogen SPS peak intensities, shown in figure 4.10, and the SPS peak at 337 nm, figure 4.11, the atomic oxygen line at 844 nm, He emission at 588 nm, H emission at 656 nm, N emission at 870 nm and OH at 310 nm.

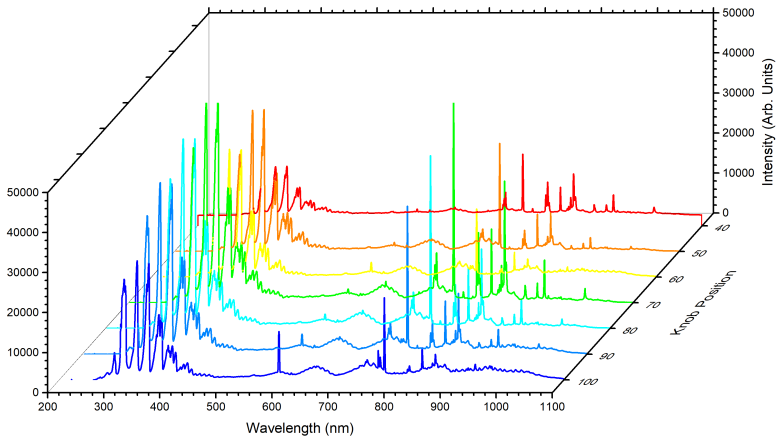

Figure 4.9: Variation of the overall OES signal taken at each voltage knob position.

From figure 4.10 we can see how the emission intensity trends for each peak of the nitrogen SPS. The intensity peaks for all voltage positions at 337 nm and 357 nm

corresponding to the (0-0) and (0-1) transitions in the SPS. To show this trend the emission intensities at 337 nm were graphed and are shown in figure 4.11. As can be seen from figure 4.11 the intensity has a peak when the voltage was set 70 % before the intensity drops off as the power is further decreased.

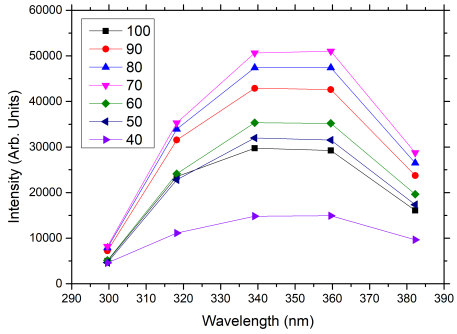

Figure 4.10: Variation of the SPS peaks for each knob position measured.

Vibrationally excited molecules play a very important role in plasma kinetics. The electron energy distribution function (EEDF) is greatly influenced by excited molecules, impacting the ionization of and dissociation of molecules in the plasma [139–141]. They also affect dissociative attachment (e.g. $O_2 + e \longrightarrow O^- + O$) as the vibrational state plays a strong role in auto-ionization and dissociation, impacting the survival probability of intermediate negative ions (O_2^{-*}) [142, 143].

Vibrationally excited $N_2(\nu)$ is an important species to consider as it stores 70 - 90 % of the discharge energy [144]. In non-thermal plasmas, the vibrational temperature is usually much higher than the translational temperature [145–147]. Much of this energy is released after the discharge pulse by vibrational-to-translational (V-T) energy and may cause a post discharge increase in temperature [148], [149–152].

The vibrational distribution of $N_2(\nu)$ does not immediately equilibrate after the

discharge pulse and studies have found that the density of N_2 ($\nu = 0$ to deviate from the equilibrium and those were ν was greater than or equal to one to approximately achieve equilibrium [153–156]. The non-equilibrium distribution relaxes through vibration-to-vibration (V-V) energy transfer in the time between discharges. Consequently the densities of lower vibrational levels increase after the discharge pulse by V-V then decrease by V-T process. It was also shown in that the vibrational temperature of N_2 was strongly affected by additives such as O_2 and NO [157, 158].

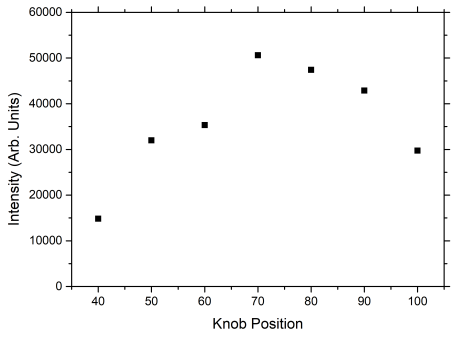

Figure 4.11: Variation of the OES signal at 337 nm for each of the knob positions measured.

In N_2/O_2 mixtures such as air, the rate of V-T is very low, however when the ambient gas is humidified the rate increases [159]. Humid air allows $N_2(\nu)$ to release it's energy through rapid V-V process with H_2O

$$N_2(\nu) + H_2O(0\,0\,0) \longrightarrow N_2(\nu - 1) + H_2O(0\,1\,0) \tag{4.23}$$

The resulting excited $H_2O(0\,1\,0)$ state then rapidly relaxes through the V-T process

$$H_2O(0\,1\,0) + H_2O(0\,0\,0) \longrightarrow H_2O(0\,0\,0) + H_2O(0\,0\,0) \tag{4.24}$$

The time scale of this reaction is on the order of 40 ns at room temperature [160] on the same time scale as the discharge pulse of the plasma. This value is more than six orders of magnitude faster than V-T processes in an $N_2{-}N_2$ system and as a result the V-T rate of $N_2(\nu)$ is approximately three orders of magnitude higher in humid air [159].

Simulations have also shown that rapid heating during the discharge pulse is caused by electron impact dissociation of O_2 and quenching of $N_2(B^3\Pi_g, C^3\Pi_u)$ and $O(^1D)$ in dry air [151]. In humid air, rapid heating is caused by V-T transitions of H_2O and enthalpy of OH formation, although this has not been experimentally confirmed [144].

The spatial distribution of excited $N_2(\nu)$ is also of importance, as they will change along with the vibrational levels of the molecules. Molecules with lower vibrational levels are typically distributed uniformly between the point anode to the plane cathode, while molecules with higher vibrational levels are distributed mainly near the anode [161].

Figure 4.12 shows how the emission intensity from atomic oxygen at 844 nm varies as a function of voltage position, while figure 4.13 shows the same for atomic nitrogen emission at 870 nm. The signal intensity appears to have two distinct trends. At lower knob positions (40 - 60 %) the signal intensity decreases as the knob position is increased. At higher knob positions the trend remains the same although the signal intensity is higher than the lower positions, indicating a change in the plasma behaviour.

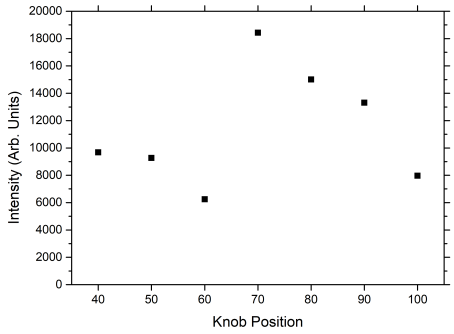

Figure 4.12: Variation of the OES signal from atomic oxygen at 844 nm.

A similar trend is observed for atomic nitrogen emissions at 870 nm as shown in figure 4.13. Again we see a jump in emission intensity as the voltage knob was changed from 60 % to 70 %.

The emission at 844 nm was chosen due to the emissions at this wavelength only being due to atomic oxygen transitions. The more intense atomic oxygen emission at 777 nm is caused by dissociative emission of molecular oxygen and direct impact emission from atomic oxygen [128].

Atomic oxygen is produced through dissociation of pre-dissociated electronic states [162–164]

$$O_2\, X^1\,\Sigma_g^+ \; + \mathrm{e} \longrightarrow O_2\,(A^3\,\Sigma_\mathrm{u}^+, C^3\,\delta_\mathrm{u}, c^1\,\Sigma_u^-) + \mathrm{e} \tag{4.25}$$

$$\longrightarrow \mathrm{O}(^3P) + \mathrm{O}(^3P) + \mathrm{e} \tag{4.26}$$

$$O_2X^1\Sigma_g^+ + e \longrightarrow O_2(B^3\Sigma_u^-) + e \tag{4.27}$$

$$\longrightarrow O(^3P) + O(^1D) + e \tag{4.28}$$

while dissociative attachment reaction is also important reaction for the production of atomic oxygen [165, 166]

$$O_2(\nu) + e \longrightarrow O_2^-(^2\Pi_u) \longrightarrow O^-(^3P) + O(^3P) \tag{4.29}$$

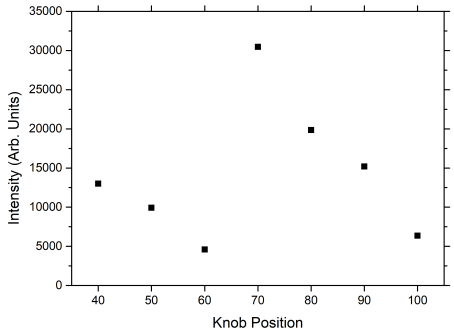

Figure 4.13: Variation of the OES signal from atomic nitrogen at 870 nm.

Atomic nitrogen on the other hand is produced by the following reactions [164, 166]

$$(N_2X^1\Sigma_g^+,\nu) + e \longrightarrow N_2^* + e \tag{4.30}$$

$$\longrightarrow N(^4S) + N(^2D) + e \tag{4.31}$$

$$N_2^* = N_2(b^1\,\Pi_u, c^1\,\Pi_u, o^1\,\Pi_u, e^1\,\Pi_u, b^1\,\Sigma_u^+, c^1\,\Sigma_u^+, e^1\,\Sigma_u^+) \tag{4.32}$$

Other reactions involving direct electronic mechanism are also considered. These reactions assumed that the excitation of vibrational levels above ν' leans only to dissociation and may or may not be perfectly valid means of N production. In [166] it was concluded that a two-step dissociation through the vibrational states is the predominant production source of N in an atmospheric pressure streamer discharge similar to the one under investigation in this study.

Helium emissions at 588 nm were also monitored at each voltage position and the emission trends are shown in figure 4.14. The emission intensity was strongest when the voltage knob was set to 100 %, however the intensity dropped to much lower levels once the voltage was decreased below 100 % and remained relatively stable after this. The plasma source gas used throughout was air and contained no excess He beyond what is found naturally in air, so the increase in He emission intensity must be attributed to some change in the plasma behaviour and not due to any increase in the amount of He present within the plasma, i.e. a threshold reached by which more He can be excited to an energetically allowable state. It was expected that He would remain constant throughout the experiment and the cause of the He increase in the emission is unknown.

Figure 4.15 shows the emission trend from OH at 309 nm. As the voltage was decreased the signal remained relatively stable before decreasing after the voltage knob position was decreased below 70 %. OH is primarily formed through the reactions [167, 168]

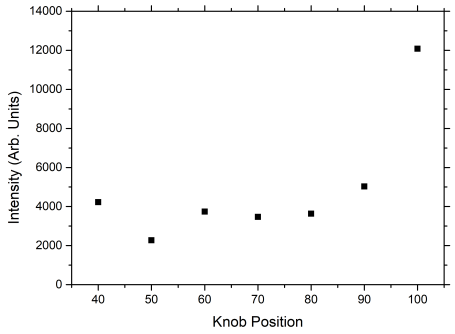

Figure 4.14: Variation of the OES signal from helium at 588 nm.

$$H_2O + e \longrightarrow H + OH + e \tag{4.33}$$

$$H_2O + e \longrightarrow H^- + OH + e \tag{4.34}$$

$$O(^1D) + H_2O \longrightarrow OH + OH \tag{4.35}$$

In [169] it was shown that the reaction rate of $O(^1D)$ is much faster than 4.33 and 4.34. Therefore the major production mechanism of OH radicals is through reaction 4.35. However this conclusion did not explain previous experimental work that showed similar levels of OH produced in both a humid-nitrogen and humid-air discharges [170]. To explain this discrepancy in results, $N_2(a) + H_2O$ was first proposed by Fresnet *et at* [171] as an important reaction mechanism for the production of OH. Therefore OH radicals are mainly produced through the dissociative reactions of [144]

$$O(^1D) + H_2O \longrightarrow OH + OH \tag{4.36}$$

$$N_2(a'^1\Sigma_u^-) + H_2O \longrightarrow N_2 + H + OH \tag{4.37}$$

Electron dissociation of reactions involving H_2O contribute less to OH radical production due to the cross-section of these reactions being lower in the energy range than those involving $O(^1D)$ and $N_2(a)$.

Furthermore, the levels of H_2O in the plasma play an important role in OH production. In [171] it was concluded that the decomposition rate of NO decreased as humidity increased due to the quenching reaction of $N_2(a)$ by H_2O because $N_2(a)$ plays the main part in the NO removal process.

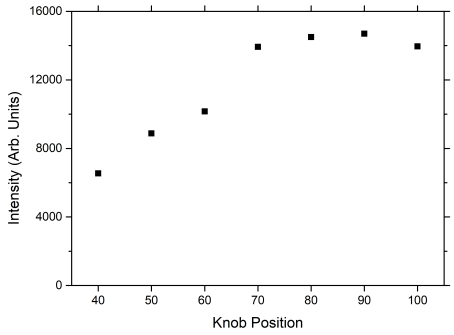

Figure 4.15: Variation of the OES signal from OH at 309 nm .

Finally loss mechanisms must also be considered. According to [169] OH goes through a complicated reaction process involving 16 reactions and three processes: (1) OH-production, (2) OH-cycle and (3) OH-recombination. Losses also occurred in two phases. The first decrease through reactions

$$OH + N(^4S) \longrightarrow NO + HOH + O(^3P) \longrightarrow O_2 + H \tag{4.38}$$

These reactions are part of the so called cycle-phase as they involved some reactions that contribute to further reactions in the second loss phase, but also include productive

reactions

$$O(^3P) + HO_2 \longrightarrow OH + O_2 \tag{4.39}$$

$$H + HO_2 \longrightarrow 2\,OH \tag{4.40}$$

and are responsible for a plateau in observed OH levels in [169].

The second phase, which is more complicated as it involves reactions created in the OH-cycle phase, water related radicals such as HO_2 and H and also through OH-recombination.

$$OH + OH + N_2 \longrightarrow H_2O_2 + N_2 \tag{4.41}$$

$$OH + OH + O_2 \longrightarrow H_2O_2 \tag{4.42}$$

$$OH + OH + H_2O \longrightarrow H_2O_2 + H_2O \tag{4.43}$$

$$OH + OH \longrightarrow H_2O_2 + H_2O \tag{4.44}$$

$$OH + OH \longrightarrow H_2O + O(^3P) \tag{4.45}$$

Overall it was concluded that OH recombination increased as the square of water concentration and that counter-intuitively OH decays faster at higher OH concentrations [144]. This is offered as an explanation as to the the plateau in OH emissions at

higher voltages observed in figure 4.15, although a further diagnostic technique such as TALIF would be required to confirm this hypothesis.

The hydrogen emissions at 656 nm are shown in figure 4.16. The emission trend is similar to those observed for O and N with two distinct phases observed again. It is interesting to speculate as to the source of H in the plasma. As discussed previously direct impact dissociation of H_2O was probably not a major contributing factor for OH production, although this may not be the case for H. However this does not rule the direct decomposition of water vapour through electron impact through the reaction

$$H_2O \longrightarrow H_2 + \frac{1}{2} O_2 \tag{4.46}$$

as a means to produce hydrogen.

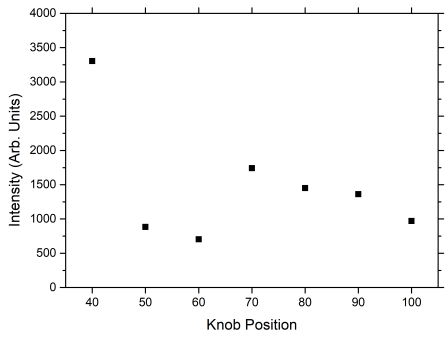

Figure 4.16: Variation of the OES signal at 656 nm due to hydrogen.

It is not possible to conclude that the majority of the H detected in the plasma are from secondary processes, typically to do with OH. N_2(a) was discussed as a possible reaction path for the production of OH and a H atom is released in the process. H is also produced when excited N and O react with OH.

4.4.2 Plume Spectrum

OES measurements were also taken of the plume region of the jet. The signal in this region was much less intense than the plasma region and as such a higher acquisition time was required to take the measurement. The spectra are shown in figure 4.17 for the plasma jet system (figure 4.17 (a)) and that produced by a microwave driven plasma jet (figure 4.17 (b)).

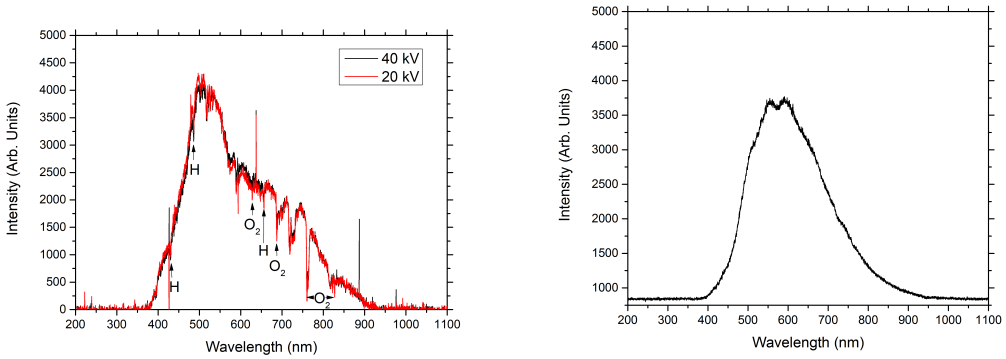

Figure 4.17: OES of the plume region of the plasma jet. (a) Spectra of plumes produced by kHz driven plasma jet, showing a spectra taking at two different voltage settings (b) Spectrum of the plume produced by a microwave driven plasma jet.

In both cases, the spectra were very broadband in their nature. The kHz driven APPJ used throughout this investigation resembled that of the Fraunhofer spectrum observed through air. Dips in intensity associated with H and molecular O_2 were the main features observed.

The spectrum was largely invariant under all conditions tested, with the belief that no more chemical reactions are taking place within the plume region. Most of the energy has been quenched and transferred to translational energy, believed to primarily

nitrogen as nitrogen contains most of the energy of the system.

The microwave spectrum shown in figure 4.17 (b) is similar to the kHz driven plasma but much hotter. There were no outstanding features present in the spectrum recorded, except for a dip centred around 620 nm caused by molecular O_2. It is the belief that since this plasma was much hotter than the kHz driven plasma that the increased energy has been transferred to translational energy of the particles that obscures any features present in the plume.

4.5 Conclusions

Throughout this chapter we have discussed optical emission spectroscopy as a diagnostic tool to determine excited species within the plasma. Initially a brief description of the theory behind spectroscopy was introduced, outlining the main processes involved and types of spectroscopy, absorption or emission, selection rules and distinction between atomic and molecular spectra including both absorption and emission spectroscopy. The key features of an emission were also discussed briefly. A small section on the methods used to disperse light into it's constituent features so that it could be spatially resolved was also given.

Measurements of the plasma revealed a complex spectrum, with emissions all across the spectrum. Emissions were detected from many excited species including atomic species H, He, and O H, He, N and O and molecular species N_2, OH and O_2. Emissions from other excited molecules such as $COand CO_2$ and atomic species C are also believed to be within the spectrum but were not fully explored within this study. Interestingly,

no emissions from NO were detected due to the casing of the plasma being optically opaque below 300 nm, where an NO band is located. It was the belief that 4 should be present in the plasma so a laser induced fluorescence investigation was conducted, see chapter 5.

For simplification, the spectrum was divided into two regions, where emission were strongest. The near-UV and blue region of the spectrum between 290 and 410 nm. This region of the spectrum was dominated by emissions from roto-vibrationally excited $N_2(\nu)$ from the second positive system. Within this region there was also emissions detected from vibrationally excited OH and from the nitrogen first negative system.

The second region of interest was located in the red and near-IR region of the spectrum located between 500 and 1100 nm. This region was dominated by emissions from excited atomic species O and N. Also within this region was the roto-vibrationally excited state of N_2 first positive system, emissions from excited H and molecular oxygen O_2.

Within this region emissions from atomic oxygen were detected at 615, 777, 844 and 926 nm. The lines at 615, 844 and 926 were caused by direct electron impact while the line at 777 is caused by dissociative excitation and direct electron. Complex multiplets associated with atomic nitrogen emission were also detected at 746, 821, 869, 939 and 1011 nm. These emissions were also believed to be caused by direct electron impact. Also within this region were emissions from hydrogen at 656 nm and helium at 588 nm.

An investigation into the influence of voltage on the spectra was conducted. It

revealed that by varying the position of the voltage it was possible to manipulate the spectrum and possibly the overall chemistry of the plasma. The trends identified support the hypothesis presented in chapter 3 that the plasma operates in two different modes and the results reflect that observation although it was not possible to verify experimentally.

In total the emissions from five excitations were monitored as the voltage varied. Emissions from the nitrogen second positive system and an emission from that band at 339 nm, atomic oxygen at 844 nm, atomic nitrogen at 870 nm, hydrogen at 656 nm, helium at 588 nm and OH at 310 nm were all monitored. For each emission monitored, a more detailed description of their possible origin and role in the plasma was given based on evidence presented from APPJs similar to the one in this investigation. These explanations are speculative in their nature and need experimental or simulation evidence to confirm this hypothesis.

The trend observed from N_2 was that the signal intensity peaked when the voltage was set to 70 % and decreased when the voltage was increased or decreased. This could be explained as more energy coupling into the vibrational bands of nitrogen at lower voltages, peaking and then more energy is used to enable further more complex reactions.

The trends observed from the atomic species all followed a similar pattern. There were two distinct phases observed as the voltage was varied. At lower voltages as the voltage was increased the trend was for the signal to decrease in intensity. Once the voltage position was set to 70 % the signal intensity jumped before decreasing again in

intensity as the was further increased. This furthermore indicates two distinct modes of operation.

The trend for helium was to remain relatively stable throughout, except for an increase in intensity when the voltage knob position was set to 100 %.

The trends observed for OH emissions was different than the atomic emissions. The intensity increased as the voltage was increased before appearing to saturate at the higher knob positions. This is believed to be caused by OH decaying at higher concentrations. The importance of water vapour was also discussed with regard to OH formation and removal.

Overall it can be concluded that APPJ under investigation has a complex spectrum with emissions primarily from atomic oxygen and nitrogen, and molecular nitrogen. By varying the operational parameters of the plasma jet it may be possible to control the chemistry and fine tune it for specific applications. We have seen that the most important species in the gas is N_2 as it contains most of the thermal energy of the system, while it's spatial distribution may explain the behaviour of the jet between modes. The influence of water vapour is also especially important as it has a large impact overall in the chemical species present in the plasma and many of the reactions observed may not be possible without its presence.

Table 1: Transitions of the second positive system of nitrogen [6].

Sequence	Transition	Wavelength (nm)
$\Delta\nu$ =-4	0-4	434.3
	1-5	427.0
	2-6	420.0
	3-7	414.1
$\Delta\nu$ =-3	0-3	405.9
	1-4	399.8
	2-5	394.3
	3-6	389.5
$\Delta\nu$ =-2	0-2	380.5
	1-3	375.5
	2-4	371.0
	3-5	367.2
$\Delta\nu$ =-1	0-1	357.7
	1-2	353.6
	2-3	350.0
$\Delta\nu$ =0	0-0	337.1
	1-1	333.9
	2-2	330.9
	3-3	328.5
$\Delta\nu$ =+1	1-0	315.9
	2-1	313.6
	3-2	311.6
	4-3	310.4
$\Delta\nu$ =+2	2-0	297.7
	3-1	296.2
	4-2	295.3
$\Delta\nu$ =+3	3-0	281.4
$\Delta\nu$ =+4	4-0	268.7

Table 2: Transitions of the first negative system of nitrogen [6].

Sequence	Transition	Wavelength (nm)
$\Delta\nu$=-1	0-1	427.8
	1-2	423.6
	2-3	419.9
	3-4	416.7
	4-5	414.0
$\Delta\nu$=0	0-0	391.4
	1-1	388.4
	2-2	385.8
$\Delta\nu$=+1	1-0	358.2
	2-1	356.3
	3-2	354.8
	4-3	353.8

Table 3: Main transition lines observed in OES of oxygen plasma [7–10].

Oxygen species	Transition line	Wavelength (nm)
O	$3\,p^5P \longrightarrow 3\,s^5S$	777.4
	$3\,p^3P \longrightarrow 3\,s^3S$	844.6
	$3\,d^5D \longrightarrow 3\,p^5P$	926.6
	$4\,d^5D \longrightarrow 3\,p^5P$	615.9
O_2^+	$b_4\Sigma_g^- \longrightarrow a_4\Pi_u$	559.1
	$b_4\Sigma_g^- \longrightarrow a_4\Pi_u$	525.7
	—	598.2
	—	636.2
O^+	—	678.9
	$3\,p^4D \longrightarrow 3\,s^4P$	464.7
	—	435.3
	$3\,d^4F \longrightarrow 3\,p^4D$	407.2

Table 4: Summary of atomic nitrogen emission lines [11].

Transistion	Total Angular Momentum J	Wavelength (nm)
$3s^4P \longrightarrow 3p^4S^0$	1/2 - 3/2	742.36
	3/2 - 3/2	744.23
	5/2 - 3/2	746.83
$3s^4P \longrightarrow 3p^4P^0$	3/2 - 3/2	818.48
	1/2 - 3/2	818.80
	1/2 - 1/2	820.03
	3/2 - 3/2	821.07
	5/2 - 5/2	821.63
	3/2 - 1/2	822.31
	5/2 - 3/2	824.24
$3s^2P \longrightarrow 3p^2P^0$	1/2 - 3/2	856.77
	1/2 - 1/2	859.40
	3/2 - 3/2	862.92
	3/2 - 1/2	865.59
$3s^4P \longrightarrow 3p^4D^0$	5/2 - 7/2	868.03
	3/2 - 5/2	868.34
	1/2 - 3/2	868.62
	1/2 - 1/2	870.32
	3/2 - 3/2	871.17
	5/2 - 5/2	871.88
	3/2 - 1/2	872.89
	5/2 - 3/2	874.73

5 Nitric Oxide Density Detection Using Laser Induced Fluorescence

While optical emission spectroscopy as described in section 4 is technically the most simple and non-intrusive method to record information about the species present within the plasma, the information provided is line of sight integrated and seldom provides quantitative information. In addition, OES can only provide information about excited particles within the plasma. Populations of excited particles are typically order of magnitudes lower than the ground state populations, requiring a theoretical model to approximately determine the link to the ground state.

Absorption spectroscopy and laser induced fluorescence are two techniques that have direct access to the ground state population and in addition metastable populations. While absorption spectroscopy requires line of sight integration, LIF can provide spatially resolved information in view of the angle between the exciting laser beam and the optical detection path, defining a scattering volume determined by the overlap of both. A second advantage of the LIF technique over absorption is that the fluorescence signal is free from the intense background of the irradiated laser light.

Several basic prerequisites are needed to preform LIF measurements. The species under investigation must have bound states states accessible according to optical selection rules. Excitation should not result in direct ionisation or dissociation with certain expectations [100]. The gaseous medium must be sufficiently optically transparent for the laser radiation and fluorescence radiation.

5.1 Introduction

Fluorescence is defined as luminescence caused by the absorption of radiation at one wavelength, followed by the near immediate re-radiation, typically at a different wavelength. Fluorescence has the distinct advantage of absorbing higher energy, ultraviolet (UV) light and emitting lower energy, visible light. Fluorescence has a number of practical applications including mineralogy [172], gemology [173, 174], chemical sensing [175, 176], labelling [177] and dyes [178, 179], and detectors for biological applications [180]. The most common application is fluorescent lighting. Due to many advantages fluorescence has been widely developed as the premise of a laser-based diagnostic.

Laser induced fluorescence (LIF) is the spontaneous emission of light from atoms or molecules that have been excited by laser radiation. The phenomenon of induced fluorescence was first observed and described by Wood *et al* in 1905, although this was several decades before the invention of the laser, or indeed before Einstein's theory on light gave scientists the theoretical framework to create a laser.

It was not until 1968 that LIF was first reported by Zare *et al* [181]. In their work they successfully used a He−Ne laser to show the LIF phenomenon using potassium dimer molecules K_2, while also observing higher vibrational-rotational levels of the K_2 molecule never observed before [182].

Since then LIF has become a standard technique used in the combustion industry for gas detection [183–186]. LIF may be used to detect many atomic, see table 5 and molecular species, see table 6.

LIF has also become an important diagnostic technique in atmospheric pressure plasmas as a way of determining gaseous species generated by the plasma. In [187] Uddi *et al* were able to determine nitric oxide levels in a nanosecond pulse discharge. Van Gessel *et al* investigated NO production in an RF plasma jet at atmosphere in [188] and [189].

In atmospheric pressure plasmas LIF also has been used to detect CH [190], CN [191], NO [187–189, 192, 193] and OH molecules, with various degrees of accuracy, ranging from simple detection to relative and absolute measurements.

OH is by far the most studied molecule in the literature due to its relevance in the combustion industry and high reactivity, although it suffers from well known calibration issues due to its complex rotational structure typically probed by LIF measurements, requiring a five level model to accurately calibrate and determine absolute number densities.

OH levels produced by atmospheric pressure helium plasma jet were investigated in [194] as well as atomic oxygen densities using the similar technique two-photon absorption laser induced fluorescence (TALIF) see chapter 6. Similar work was undertaken in [195], quantifying OH levels produced by a plasma jet for applications in oncology [196]. OH levels were also investigated using a corona discharge in [197]. A DBD was also the subject of LIF investigation for OH levels in [198].

Atom	Transition	λ laser (nm)	λ fluorescence (nm)
Al	$3p\ ^2P^0 \longrightarrow 4s\ ^2S$	394	396
As	$4p^3\ ^4S^0 \longrightarrow 5s\ ^4P$	193	245
Cu	$4s\ ^2S \longrightarrow 4p\ ^2P^0$	325	325, 510
Fe	$a\ ^5D \longrightarrow y\ ^5D^0$	302	382
Ge	$3p^2\ ^3P_0 \longrightarrow 4s\ ^3P_1$	265	275
Mo	$a\ ^7S \longrightarrow\ ^7P^o$	313	317
Si	$3p^2\ ^3P_0 \longrightarrow 4s\ ^3P_1^o$	251	253
Zn	$4s^2\ ^1S \longrightarrow 4p\ ^1P^o$	214	214

Table 5: Allowable atomic laser induced fluorescence transitions for various atoms showing the atomic transition, absorption and emission wavelength.

5.2 Single photon LIF

LIF spectroscopy is an active optical method with the ability to measure populations densities and velocity distributions of atoms, molecules and ions. It can also measure electric fields in some cases [199, 200]. Narrow-bandwidth tunable laser radiation is used to excite particles through absorption of a photon into a higher energy state. The fluorescence radiation emitted when the particle makes a transition to an energetically lower state, is analysed in order to obtain information about the population, the life-time of the upper state and the velocity distribution of the particles. The comparable high cross section of the fluorescence process when combined with the high amplification capabilities of modern photo detectors make LIF a powerful diagnostic technique.

Along with modern lensing that are more than capable of providing focusing and modern laser systems (ps, fs, As etc) that can provide pulsing parameters that meet all requirements with respect to space and time resolutions in plasma discharges.

5.2.1 Mechanism

Single photon LIF is based on the absorption of a single photon by an atomic or molecular species produced by laser radiation and the subsequent emission of a photon. This process is shown schematically for a polyatomic molecule in figure 5.1. A photon produced by a laser with an energy that matches the energy separation between the ground state and an excited electronic state is absorbed by the molecule, which then excites an electron to a higher energy level.

Subsequently, the molecule relaxes back to the ground state through the emission of a fluorescent photon. There are however a number of other energy transfer processes that limit the number of emitted fluorescent photons by depopulating the excited state. These depopulation processes, also shown in figure 5.1 include stimulated emission, collisional quenching, ionization and photo-dissociation, internal and external conversion and inter-system crossing.

There are two ways in which LIF spectroscopy can applied: dispersion and excitation. In the case of dispersion, the laser wavelength is fixed at one absorption wavelength of the species under investigation. The fluorescence spectrum is then recorded by scanning the spectrometer wavelength. The resulting fluorescence spectrum corresponds to all allowable radiative transitions towards lower energy levels of the species under investigation.

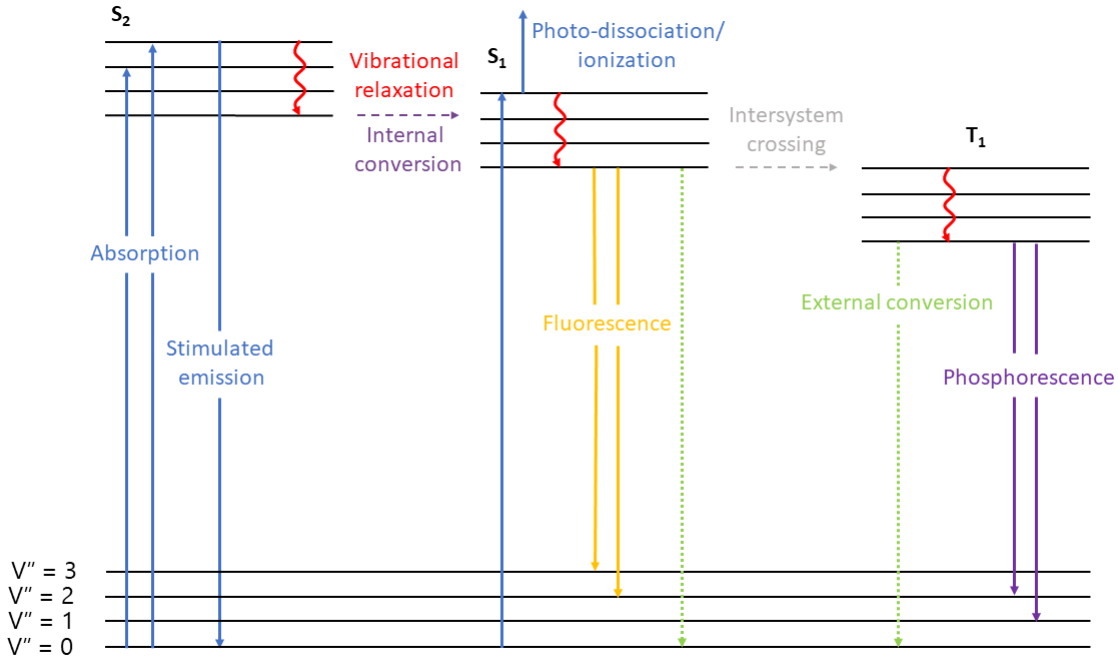

Figure 5.1: Jablonski diagram of a hypothetical molecule showing absorption and deactivation processes typically found in LIF.

For the case of excitation spectrum, the laser wavelength is scanned through a wavelength range. A particular band or range of wavelengths of the resulting fluorescence is recorded by using an optical filter or low-resolution spectrometer. Fluorescence will only be detected when the wavelength of the laser matches a resonant absorption state between two energetic levels. Using this method very high spectral resolution can be achieved as the linewidth of the laser used is typically much smaller than the species absorption profile.

5.2.2 LIF rate equations

Quantitative analysis of single-photon LIF can be approximated as a two level system with the ground state as state 1 and the excited state as state 2. The excitation process as shown in figure 5.2 leads to the spontaneous emission or fluorescence of a photon A_{21} in figure 5.2. In this simple model, only stimulated emission b_{21} and collisional quenching Q_{21} are assumed to affect the excited state population. Other processes that might remove population from the excited state and limit the number of emitted fluorescent photons are neglected. Ionization W_{2i} and photo-dissociation P are also assumed to have negligible impact if the incident laser fluency is kept sufficiently low.

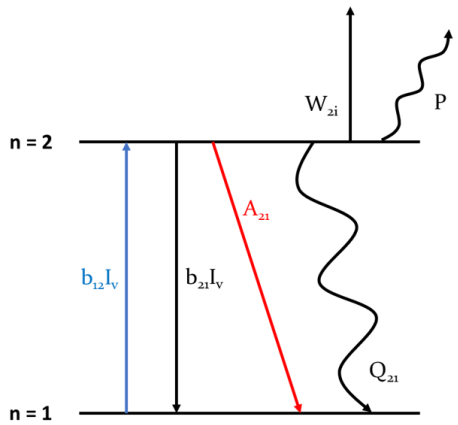

Figure 5.2: Energy level diagram of the laser induced fluorescence phenomenon. Initially a laser photon is absorbed by a LIF active atom or molecule, followed by the spontaneous emission of a fluorescence photon.

There are four assumptions that are necessary when using the two level model to describe the LIF process. (1) The laser beam must be uniform and linearly polarized. (2) The population of the particle under investigation must be in the ground level

before laser excitation. (3) The fluorescent signal is measured when the population in the excited state reaches steady state. (4) The fluorescence occurs only at one wavelength that corresponds to a specific electronic transition.

LIF if used to determine the absolute number density of a given radical within a system. For this to be possible a relationship must be established between the collected signal and the total number of absorbing radicals within the collection volume. It is well known that the fluorescence signal observed is proportional to the product of the of probability of fluorescent photon emission from the excited state and the number of radicals in the excited state

$$S_{LIF} = N_2 A_{21} V \frac{\Omega}{4\pi} \eta \tag{5.1}$$

where N_2 is the population of the excited species under investigation, A_{21} is the Einstein coefficient A for the rate of spontaneous emission from the excited state to the ground the state, V is the volume of illumination by the laser, η is the collection efficiency and Ω is the collection solid angle.

For a relationship between the number of excited state radicals and the total number of radicals in the collection volume a rate analysis between the ground and excited state is preformed. For any given instant in time, the rate of change of the ground and excited state population are governed by a balancing process between populating and depopulating each state, known as rate equations. Simplified rate equations are shown in equation 5.2 for the ground state and equation 5.3 for the excited state. Note that for this analysis, processes such as ionization and inter-system crossing are neglected.

$$\frac{\delta N_1(t)}{\delta t} = -N_1(t)b_{12}I_v + N_2(t)(A_{21} + Q_{21} + b_{21}I_v) \tag{5.2}$$

$$\frac{\delta N_2(t)}{\delta t} = N_1(t)b_{12}I_v - N_2(t)(A_{21} + Q_{21} + b_{21}I_v) \tag{5.3}$$

In the steady state condition, the time dependence is zero and a relation between the populations in state one and two can be formed and is given by:

$$N_2 = N_1 \frac{b_{12}I_v}{A_{21} + Q_{21} + b_{21}I_v} \tag{5.4}$$

From equation 5.4, we can see there are two limits to the equation: weak excitation and strong excitation. In the weak excitation limit, the induced or stimulated emission rate is much lower than the sum of the collisional quenching and spontaneous emission rates and in the strong excitation limit the induced emission rate is much greater, such that the populations in both states are approximately equal $N_1 \approx N_2$. In this work, the weak excitation scenario is of more interest as it results in a linear relation between the incident laser fluence and measured fluorescence signal.

In the weak excitation regime, the excited state population is much lower than the ground state, due to depopulation rates being much higher than the excitation rate. Due to this, we can assume that the total population is equal to the population of the ground state $N_{total} = N_1$. We also assume that stimulated emission b_{21} is typically very small and can also be neglected. Using these assumptions, we can determine a relation between the measured excited state and the total population given by

$$N_2 = N_{Total}\frac{b_{12}I_v}{A_{21}+Q_{21}} \tag{5.5}$$

Substituting equation 5.5 into equation 5.1 yields

$$S_{LIF} = N_{Total}\frac{A_2}{A_{21}+Q_{21}}b_{12}I_vV\frac{\Omega}{4\pi}\eta \tag{5.6}$$

5.2.3 Strengths of LIF

LIF offers a number of advantages over other laser based diagnostics such as scattering or OES. The most significant of these is the ability for species-selective excitation. It is possible for the wavelength of the laser to be tuned such that the bandwidth of the laser overlaps with an absorption line or band of a given atom or molecule. These features are typically discrete in nature allowing for specific excitation of a single transition that has a large cross-section, resulting in a selective excitation of a particular transition and emission of a photon that is specific to that atom or molecule.

The fluorescence signal can then be spectrally or temporally filtered from other background signals such as the laser or background emission, creating a large signal-to-noise ratio for most applications, when appropriate filters are used. These techniques have been refined and used for very low detection of particles ranging from a few parts-per-million to parts-per-billion, meaning LIF is a viable technique for the detection of minor or trace species in many applications.

Another strength of LIF is that the signal is spatially resolved. The signal generated is produced only from the volume of the laser, and very little interaction outside the beam. The fluorescence created is isotropic in nature and emitted in all directions,

allowing for orthogonal collection with no loss in signal, or interference from the laser or plasma source, which is not possible in absorption spectroscopy for example. This allows for light to be detected from very specific regions of interest.

Finally, because the laser can be tuned to a specific electronic transition of an atom or molecule, it is possible to measure the temperature or certain temperature sensitive rotational lines with accuracy of $\pm$ 25 K.

5.2.4 Weaknesses of LIF

LIF of course is not without its weaknesses. One of its main limitations is the inherent complication of non-radiative decay; not every atom or molecule that is excited will emit a fluorescent photon. There are many non-radiative decay processes that an excited particle can undergo, outlined in figure 5.1, such as quenching, stimulated emission, inter-system crossing or internal conversion. Therefore, the fluorescence signal detected is not a a direct measurement of the ground state population as typically desired in LIF experiments. LIF signals and the ground state populations depend strongly on temperature, pressure and gas composition. This can significantly complicate some measurements since temperature, pressure and composition can change within the laser illumination volume.

Additionally, not all atomic and molecular species fluoresce, not all excited states fluoresce and it is not always possible for transitions to absorb at accessible wavelengths. Further complications such as photo-induced chemistry e.g. photolysis of molecular oxygen, or light-trappings in molecular species should also be considered.

Finally, since LIF is a spontaneous emission technique, signal levels may be much

smaller than stimulated techniques depending on experimental conditions.

5.3 Experimental

Experiments involving LIF were set up as in figure 5.3. An Innolas Spitlight 600 Nd:YAG laser system that has a bandwidth of < 0.03 cm^{-1} operating at a frequency of 10 Hz was used to pump a Radiant Dyes Narrowscan dye laser. The second harmonic of the Nd:YAG laser that produces 8 ns pulses at 532 nm was used to pump a dye mixture of of DCM/Pyridine 1 in a methanol solution to produce a useful lasing wavelength range of 640 - 705 nm. This light was passed through a series of doubling and tripling crystals before finally passing through a Pellin Broca prism system to separate the desired UV radiation at 226 nm from the dye fundamental and doubled wavelengths.

The laser output was passed through a series of UV grade fused silica prisms and a 100 μm iris to reduce the beam diameter and directed towards the plasma jet, mounted on a movable platform located in a fume cupboard. The laser light was directed such that it passed perpendicularly through the plasma jet afterglow approximately 1 mm from the jet orifice.

A back reflection from the prism was steered towards a Thorlabs Det210 fast photo diode, connected to a 10 dB amplifier and used to trigger the oscilloscope. A Hamamatsu R636-10 photomultiplier tube (PMT) positioned orthogonally to the laser beam and plasma jet was used to collect the fluorescence generated by the interaction between the laser beam and NO molecules. A LOT-Oriel optical bandpass filter with a central wavelength of 250 nm $\pm$ 3 nm, 11 nm FWHM, was placed over the PMT

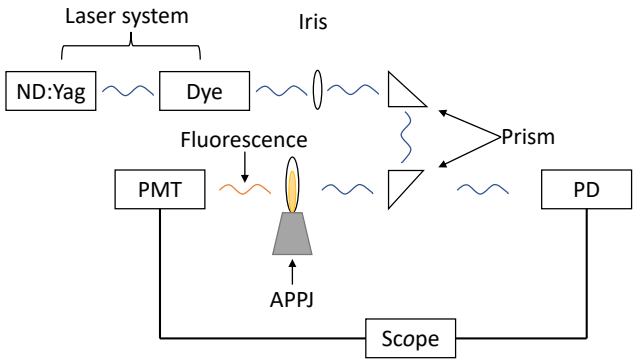

Figure 5.3: Schematic representation of the LIF experimental set up.

to filter out all background and laser light (226 nm), allowing only the fluorescence wavelength of 247 nm to reach the PMT. As the fluorescence and laser wavelengths were very close, it was vital to ensure only the fluorescence was detected by the PMT.

The laser wavelength was scanned over a range of wavelengths, while recording the laser intensity and fluorescence to determine the peak LIF signal as per [187]. This wavelength was then used for further LIF experiments.

Once the central peak was determined, the laser wavelength was moved to a local minima and the signal strength was recorded as the background signal. This signal was then subtracted from any measured LIF so that the measurement only contained light from the NO fluorescence.

5.3.1 Temperature dependence

The spectrum intensity $I_\lambda(\lambda)$ depends on the rotational distribution of the NO $X(v = 0)$ ground state and therefore depends on the rotational temperature T_{rot}. However, the temperature dependence of the intensity does not depend on temperature, as some rotational lines increase with temperature and some decrease. Therefore, it is possible to select a range of wavelengths, whereby the intensity change of lines is compensated by an opposite change of other lines. As a result the total wavelength integrated intensity I is effectively temperature independent.

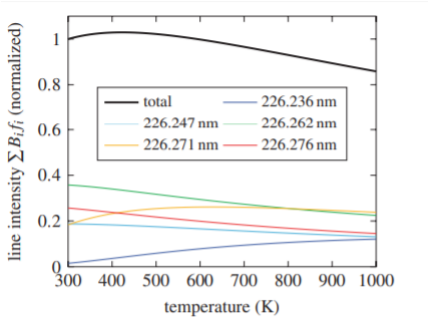

Figure 5.4: Temperature dependence of the LIF intensity or rotational lines of NO(X) for the excitation wavelength int the range 226.23 - 226.28 nm as produced by Van Gessal.

Van Gessal *et al* showed that for NO this range is 226.23 - 226.28 nm, see figure 5.4 [188] and therefore all experiments are undertaken within this range.

5.3.2 Calibration

To calculate the absolute number density n from the LIF signal, the set-up has to be calibrated using a gas mixture with known density of NO. For this a gas mixture of N_2/NO with 40 ppm NO was used. LIF was preformed using this gas mixture at a flow rate of 5 slm, located 1 mm from the jet orifice. Van Gessel *et. al* [188] had shown that at these distances and flow rates, dilution of the has mixture from ambient conditions was negligible and that the gas composition was of the calibration measurement was equal to that of the premixed gas.

The difference in quenching between the calibration measurement and the plasma measurement is taken into account by the decay time τ. In practice this was achieved by taking the natural log of the tail of the curve and applying a linear fit. The decay time τ was then determined by taking the inverse of the slope of this curve. Laser energy E is measured to account for fluctuations in the laser power. The absolute number density n of the NO(X) ground state is then given by: [189]

$$n = \frac{n_{cal} E_{cal} \tau_{cal}}{I_{cal}} \frac{I_{lif}}{E_{lif} \tau_{lif}} \tag{5.7}$$

τ in both cases is determined by fitting an exponential fit to the tail part of the fluorescence signal.

5.4 Quenching

After the laser pulse, the density n_{exc} decays exponentially with decay time τ. The quenching rate Q is the total rate of all collisional processes that depopulate the states

from which the fluorescence signal is monitored. These processes typically include electronic energy transfer (EET), vibrational energy transfer (VET) and ionization.

Q can be calculated using equation 5.8 and the rate coefficients listed in table **??**. A_u is given by the natural lifetime τ_0 of the NO A state in equation 5.9. The calculated natural lifetime of the $\nu = 0$ band is $\tau_0 = 205$ ns [188], while experimental values of $\tau_0 = 192.6$ ns have been measured [201].

$$Q = \Sigma n_i q_i \tag{5.8}$$

$$A_u = \Sigma_l A_{ul} = \frac{1}{\tau_0} \tag{5.9}$$

The decay time is directly measured by applying an exponential fit of the time resolved LIF signal. Van. Gessel et al also showed that for each rotational line, the decay times were randomly distributed around an average value of $\tau = 54.5$ ns. This value was found to be consistent with measurements found in this study, with an average value of $\tau = 50$ ns.

Rotational energy transfers are typically much faster than VETs, at a rate of about 6.0 x $10^9 s^{-1}$ for both air and helium. These RETs occur at time scales much smaller than the laser pulse duration. However, since the fluorescence of the full vibrational band is monitored RET does not cause a loss of signal and can therefore be ignored in the quenching.

5.4.1 Linearity

Saturation effects become important when the laser power is so high that the populations of the states involved are substantially affected by the laser radiation. Photon absorption and stimulated photon emission can then begin to dominate. When the stimulated photon emission rate equals the absorption rate, the spontaneous emission rate is negligible, further increase of the laser power will not change the balance between the population of the states consideration. Full saturation of the fluorescence signal is then reached.

To measure NO densities, the LIF signal must not be saturated. $n_u << n_l$ so that effects from stimulated emission can be neglected. Van Gessel et. al. showed that at laser energies less than 1.5 μJ the LIF signal is proportional to the laser signal. In all cases within this work typical laser energies were 0.5 - 1.0 μJ to avoid saturation and ensure the LIF signal is proportional to the laser energy.

5.5 Results and discussion

Figure 5.5 shows the excitation spectrum of the plasma plume taken at a distance of 1 mm from the jet orifice. The scan was taken over a range of 21 pm from 226.313 nm to 226.334 nm. The scan was started at a region known to be outside the excitation band associated with the NO transition and finish at a another local minima past the excitation maxima. Scans were taken in 0.5 pm intervals while the LIF signal was recorded at each wavelength.

The LIF signal starting from approximately zero, began to increase in intensity as the laser wavelength began to match the excitation transition of the NO band, until it reached a maximum at approximately 226.320 nm. After passing the maxima the LIF signal began to decrease until the laser wavelength passed the transition region.

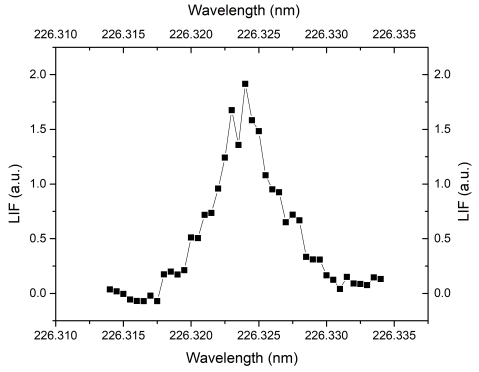

Figure 5.5: Excitation spectrum of the plasma plume taken over a range of 226.324 nm to 226.335 nm. The graph shows how the LIF signal initially starts at zero before increasing as the laser frequency moves towards the excitation peak, which was 226.323 nm before decreasing as it passes the peak.

Figure 5.6 shows the excitation spectrum recorded while passing the NO/N_2 cali-

bration gas through plasma jet at a distance of 1 mm from the jet orifice. The scan was taken over a range of 21 mm from 226.313 nm to 226.334 nm. The scan was started at a region known to be outside the NO transition and finish at another local minima outside past the excitation maxima. Scans were taken in 0.5 pm intervals while recording the LIF signal intensity at each wavelength.

The scan maximum in this case was found to be 226.320 nm. The discrepancy between this and the result recorded in figure 5.5 was due to day to day variations in the laser performance. The temperature of the laser housing would cause small fluctuations in the laser performance that would result in small drifts in the laser.

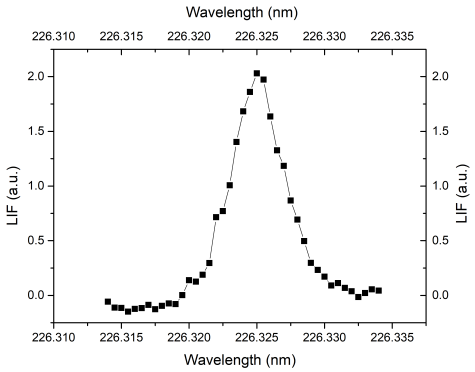

Figure 5.6: Excitation spectrum of the NO/N_2 calibration gas taken over a range of 223.324 nm to 226.335 nm.

Figure 5.7 shows an example of a temporal LIF signal produced by the plasma at 1 mm from the jet orifice. The graph presented shows the raw data collected during an experiment without any further analysis. Figure 5.8 shows the corresponding laser signal recording while preforming the measurement. The pulse width is approximately 15 ns at FWHM.

Figure 5.9 shows an example of a temporal LIF signal recorded while flowing the

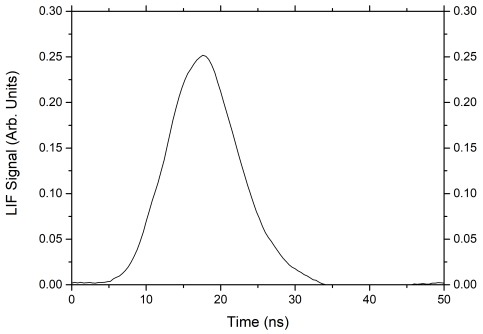

Figure 5.7: An example of the LIF temporal signal produced by the plasma.

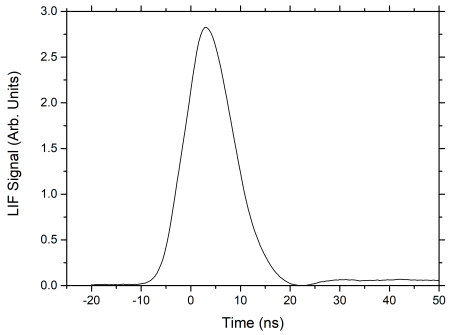

Figure 5.8: Laser signal recorded while measuring the LIF signal.

NO/N_2 calibration gas through the jet. The signal is normalised to the laser intensity, which was recorded simultaneously. After an initial rise time of approximately 20 ns the LIF signal reaches its maximum. The signal then decays exponentially over a time scale of 350-375 ns. The calibration decay times are typically two to three times longer than those recorded from the plasma jet. This is due to the relative lack of oxygen in the calibration case than ambient air used to ignite the plasma. Oxygen acts as a strong quencher for NO gas so accordingly reduces the signal length.

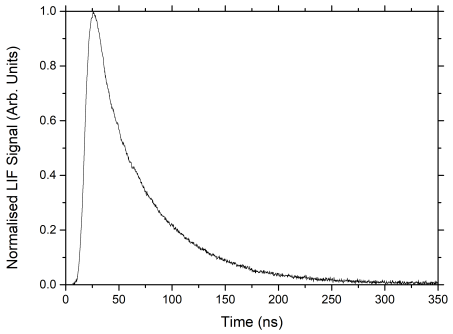

Figure 5.9: An example of the LIF temporal signal produced by the NO/N_2 calibration mixture.

5.5.1 Spatial distribution

LIF measurements were taking along the plasma jet afterglow region. Starting at a distance of approximately 1 mm from the jet orifice, measurements were taken in 5 mm steps over a range of 50 mm, the limit allowable by the stage.

Care was taken to ensure that the laser beam crossed the afterglow region by running a simulation of the test, with a piece of fluorescent paper to show the position of the beam relative to the jet effluent. Starting at the jet orifice, the jet was slowly retracted along the adjustable stand while monitoring the position of the beam relative to the jet.

If the beam drifted in the vertical axis as the translational stage was moved, the angle of the jet was adjusted such that the beam intersected the plasma plume again.

Figure 5.10 shows how the NO absolute density varies along the afterglow region of the plasma jet. Densities are highest closest to the orifice and remain relatively stable up to a distance of 20 mm before decreasing linearly the further away form the jet

measurements were taken.

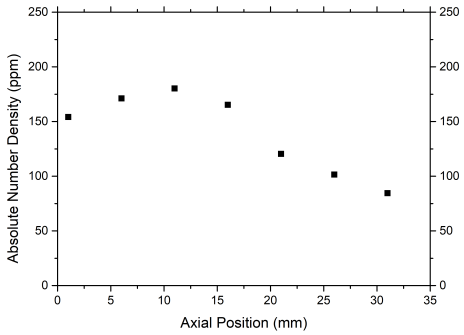

Figure 5.10: Spatial distribution of NO density moving away from the plasma jet.

Close to the jet orifice, the plasma is most dense, containing the most amount of energetic particles, allowing a greater amount of NO to be present. The initial small increase in NO density moving away from is due to the structure of the effluent as it leave the orifice. Further away from the jet the signal decreases as the NO is quenched and diffuses into the ambient.

5.5.2 Influence of airflow

LIF measurements were taken while varying the airflow through the plasma jet. Airflow was varied from 6 L/min to 12 L/min in 3 L/min intervals. Results are shown in figure 5.11.

It was found that for the airflows tested, flow rate had very little influence in the NO densities within the plasma plume region. The NO density remained stable between 200 - 210 ppm at all flow rates tested.

This result was surprising as both atomic oxygen levels and the electrical behaviour of the jet were influenced by the flow rate of the jet, indicated more stable chemistry

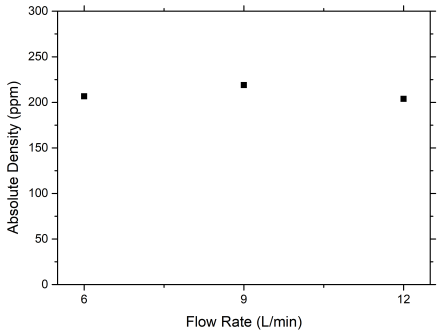

Figure 5.11: Absolute NO density as a function of flow rate.

involved and a long lifetime of the NO when compared to the much more reactive atomic oxygen.

5.5.3 Influence of voltage

Further LIF measurements were taken while varying the voltage delivered to the plasma jet. Measurements were taken varying the voltage from 70 - 100 as per the dial on the PSU, corresponding to the percentage of the power supplied as per section. This was the range in which the plasma could be reliably run for the length of a LIF experiment. Results are shown in figure 5.12.

NO densities increased linearly as the percentage of the power delivered to the jet increased. This result was again surprising when compared to the OES and TALIF measurements

5.6 Discussion on NO production and loss mechanisms

There are three main reaction mechanisms that produce NO [15]. (1) The Zeldovich, thermal NO mechanism, (2) the N_2O-intermediate mechanism and (3) the prompt-

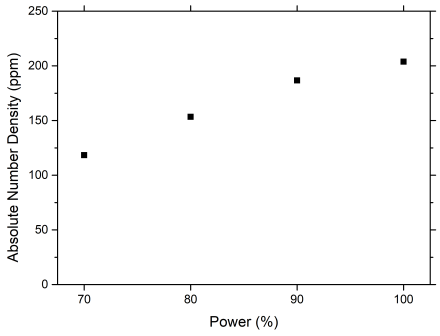

Figure 5.12: Results showing the influence power supply voltage has on NO density in the plasma plume. Higher voltages resulted in higher levels of NO detected.

NO mechanism. The amount of NO produced by each of these mechanisms typically depends on the plasma gas temperature and pressure and electron temperature.

There are three primary reactions involved in the Zeldovich mechanism:

$$O + N_2 \longrightarrow NO + N \tag{5.10}$$

$$N + O_2 \longrightarrow NO + O \tag{5.11}$$

$$N + OH \longrightarrow NO + H \tag{5.12}$$

The Zeldovich mechanism requires the breaking of strong molecular bonds, and are therefore typically thermal in their nature. However due to the non-thermal nature of APPJs the required energy to break the inter-molecular bonds is provided through fast thermal electrons.

The are four reactions involved in the N_2O-intermediate mechanism.

$$N_2 + O + M \longrightarrow N_2O + M \tag{5.13}$$

$$N_2O + O \longrightarrow NO + NO \tag{5.14}$$

$$N_2O + O \longrightarrow N_2 + O_2 \tag{5.15}$$

$$N_2O + H \longrightarrow N_2 + OH \tag{5.16}$$

As the name suggests, the N_2O-intermediate mechanism involves the initial production of nitrous oxide, followed by a subsequent reaction with involving atomic O or H with N_2O to form NO or reforming N_2.

The third main pathway for NO production is the prompt-NO mechanism. The prompt mechanism does not directly form NO, but rather involves the reaction of hydrocarbon species with N_2 to form cyano compounds such as HCN and atomic nitrogen which react to form NO.

Table 7 outlines the relevant chemical reactions involving the production and loss mechanisms of NO as described by Dorai and Kushner [202]. Reactions (7) - (9) require the presence of atomic species N or O. Both of these species were experimentally confirmed in OES experiments, see section 4, created in the main active plasma region of the jet. Reaction (8) which uses O as the atomic species is common in combustion systems, but has a negligible impact at temperatures T $<$ 1400 K [203]. This is consistent with TALIF experiments showing high levels of atomic oxygen detected in the afterglow, see section 6, implying that atomic oxygen levels are not being depleted

through this reaction. Eliminating reaction (8) the main production method of NO must be either reaction (7) or (9). Both of these reactions require atomic nitrogen to form NO, while reaction (9) in addition requires water vapour.

Van Gessal *et al* [189] reported that adding O_2 to their mix was significantly less efficient at producing NO when compared to adding N_2 to the mixture. The required O_2 needed to form NO as per reaction (7) was believed to originate through diffusion with ambient air. Reaction (9) is much more efficient than (7) but the production of OH requires water vapour and it's quantities within the plasma system were unknown.

NO loss mechanisms are more complicated than the production route, as NO acts a precursor molecule for more complicated NO_x reactions. NO reacts readily with both atomic oxygen and ozone to produce NO_2 through reactions (11) and (12). Reactions (11) and (12) are fast typically resulting in quick depletion of NO into O_3 as reported by [202] and [189].

The so far discussed reactions however do not delve into the specifics of the molecular behaviour. It is assumed that the vast majority of productive reactions have taken place in the plasma proper and that no reactions take place within the plume that will add to the overall levels of NO. In [204] the ratio of $N_2(A^3\Sigma_U^+,\nu)$ quenching by O was studied, and they found two reaction channels

$$N_2(A^3\Sigma_U^+) + O(^3P) \longrightarrow N_2 + O(^1S) \tag{5.17}$$

$$N_2(A^3\Sigma_U^+ + O(^3P) \longrightarrow NO + N(^2D) \tag{5.18}$$

At lower vibrational levels reaction 5.17 was the main reaction channel for quenching, while at higher vibrational levels ($\nu > 2$) reaction 5.18 dominates.

A further reaction channel was proposed in [205] to explain the dynamics of fast gas heating of nitrogen-oxygen mixtures with high degrees of dissociation of O_2 molecules

$$N_2(B^3\Pi_g) + O(^3P) \longrightarrow NO + N(^4S,^2D) \tag{5.19}$$

$$N_2(C^3\Pi_g) + O(^3P) \longrightarrow NO + N(^4S,^2D) \tag{5.20}$$

$$N_2(a'^1\Pi_g) + O(^3P) \longrightarrow NO + N(^4S,^2D) \tag{5.21}$$

These reactions were used in [206–208] to describe the temporal behaviour of $O(^3P)$, $N(^4S)$ and NO number densities in the afterglow region of a pulsed nanosecond discharge in air.

Relaxation of the electronic excitation of N_2^* is also important to consider as much of the energy will couple to gas heating and vibrational excitation of both $NO(\nu)$ and $N_2(\nu)$.

Relaxation of the electronic excitation of N_2^*=$N_2(A^3\Sigma_u^+,B^3\Pi_g,C^3\Pi_u,a'^1\Sigma_u^-)$ molecules can be described by the following [209]

$$N_2^* + O(^3P) \longrightarrow NO(\nu) + N(^2D) \tag{5.22}$$

$$N(^2D) + O(^3P) \longrightarrow N(^4S) + \ + O(^3P) \tag{5.23}$$

$$N(^2D) + NO \longrightarrow N_2(\nu) + O(^3P) \tag{5.24}$$

$$N(^4S) + NO \longrightarrow N_2(\nu) + O(^3P) \tag{5.25}$$

These reactions can be summarized as as single summary process that leads to the loss of electronic excitation of $N_2(A^3\Sigma_u^+, B^3\Pi_g, C^3\Pi_u, a'^1\Sigma_u^-)$ molecules

$$N_2^* + O(^3P) \longrightarrow N_2(\nu) + O(^3P) + \Delta E \tag{5.26}$$

therefore all the energy of $(B^3\Pi_g, C^3\Pi_u, a'^1\Sigma_u^-)$ electronic excitation, in the set of the reactions 5.22 - 5.25 going to vibrationally excitation of $NO(\nu)$ 5.22, $N_2(\nu)$ 5.24 and 5.25 and gas heating. The percentage of energy converted to gas heating through these reactions is rather high and much higher than in reactions involving the quenching of $N_2(B^3\Pi_g, C^3\Pi_u, a'^1\Sigma_u^-)$ states by oxygen as much of the energy is spent dissociating O_2 molecules.

As discussed in [209], the presence of a high concentration of O atoms in the discharge makes for very effective production of nitrogen oxides. In [210] and [211] calculations were preformed following the dynamics of $O(^3P)$, $N(^4S)$ atoms and NO molecules. The calculations were preformed with and without taking into account reactions involving 5.19 - 5.21. It was found that the difference in density for $O(^3P)$ was relatively small, but there was a six fold difference in the difference in NO densities indicating a significant additional production of NO mechanism in reactions involving quenching of $N_2(B^3\Pi_g, C^3\Pi_u, a'^1\Sigma_u^-)$ states by O.

[209] used reactions derived from [212] to deduce that the main processes involved in the formation and destruction of NO were

$$e + N_2 \longrightarrow e + N(^4S) + N(^2D) \tag{5.27}$$

$$N(^2D) + O_2 \longrightarrow NO + O(^3P,^1D) \tag{5.28}$$

$$N(^4S) + NO \longrightarrow N_2 + O(^3P) \tag{5.29}$$

One of the N atoms in 5.27 was involved in NO formation and the other in NO destruction. This also explains the energy efficiency of NO production reported in [209] as higher power is associated with an increase in the rate constant of the reaction

$$N(^4S) + O_2 \longrightarrow NO + O(^3P) \tag{5.30}$$

due to a rise in gas temperature, while at lower input powers, the role of 5.30 increases due to the decrease in the contribution of of reaction 5.29 associated with NO density reduction.

When reactions 5.19 - 5.21 were included, the results changed. Even at low input energies and dissociation degree of O_2 molecules, the reactions

$$N_2(A^3\Sigma_u^+ + O(^3P) \longrightarrow NO + N(^2D) \tag{5.31}$$

$$N(^2D) + O_2 \longrightarrow NO + O(^3P,^1D) \tag{5.32}$$

actually determine the nitrogen oxide production in air discharge plasmas.

5.7 Conclusions

Throughout this chapter we have investigated, using the spectroscopic technique laser induced fluorescence, the generation of nitric oxide molecules by the APPJ and their abundance within the afterglow region of the APPJ. The various control parameters of the APPJ were investigated, along with the concentrations along the axial plume position of the jet.

Initially, an introduction to the topic of LIF was given. In it the basic underlying principle of LIF was introduced as well as other processes that are involved in the LIF process such as quenching, photo-ionization and stimulated emission. Rate equations for a two level model were also developed.

A brief description of the strengths and weaknesses of LIF were also discussed. Strengths included the species selective excitation, the ability to choose appropriate optical filters to allow a large signal to noise ratio, the ability to spatially resolve a signal and finally allow rough temperature measurements if an appropriate rotational band is excited.

Weaknesses included complications due to non-radiative decay paths that a particle may undergo. These included quenching, stimulated emission, inter-system crossing and internal conversion. Additionally not all particles will fluoresce and it is also not always possible for particles to absorb at the wavelength range being used. Finally, LIF due to its spontaneous nature may not produce as strong a signal as other techniques that use stimulated emission for example.

A description of the experimental procedure was given. This included a brief sum-

mary of laser system and the optical components used to steer the beam. Using this processes it was possible to detect a signal that was caused by laser induced fluorescence of NO created by the plasma. To determine the peak of the signal, a wavelength range scan was used while the signal was recorded. This scan also allowed a background signal to be determined that contained no light from any LIF process. This background was subtracted from the subsequent LIF signal so that the LIF signal only contained light from fluorescence and background light was minimized. The laser signal was also monitored throughout to ensure that LIF signal behaved in the linear region and did not move into the saturation region.

To determine the absolute number density of the signal calibration was necessary. This was done by using a calibration gas with a known number density of NO. By comparing the calibration signal to the un-calibrated signal created by the plasma it was possible to determine the absolute number density of NO created by the plasma.

Once it was established that it was possible to detect NO the influence of various operating parameters were investigated. The absolute number density along the plume was initially investigated. It was found that the it was possible to detect NO up to 30 mm away from the jet at levels up to 100 ppm. Closer to the jet orifice the number density of NO remained stable at levels around 200 ppm up to 15 mm away from the orifice, beyond this distance the number densities decreased.

An investigation into the influence of airflow should that the number density of NO remained stable and was unaffected by airflow. This could be explained as the particles being replaced as quickly as they are removed from the interaction region of the laser

and not to do with any internal chemistry within the plasma.

a further investigation into the influence of voltage revealed that the absolute number density of NO increased as the voltage knob was increased indicating that there is some internal chemistry taking place within the plasma affecting the levels of NO created.

Finally, a discussion was given into the possible NO production and removal processes were given. Thermal influences are of great importance into the formation of NO in flames, but in non-thermal plasmas, direct electron impact can be used to create the necessary atomic species for NO formation. A detailed description of further production processes was also outlined involving a study into the impact of vibrationally excited nitrogen and its influence on NO formation.

Atom	Transition	λ laser (nm)	λ fluorescence (nm)
BCl	A $^1\Pi \longrightarrow$ X $^1\Sigma^+$	272	272
CCl	A $^2\Delta \longrightarrow$ X $^2\Pi$	278	278
CF	B $^2\Delta \longrightarrow$ X $^2\Pi$	193	194
CF_2	$\tilde{A}$ ^{1}A $\longrightarrow$ $\tilde{X}$ ^{1}A	248, 266	257, 271
Cl_2^+	A $^2\Pi \longrightarrow$ X$^2\Pi$	386	396
CH	B $^2\Sigma^- \longrightarrow$ X $^2\Pi$	387	390
CH	A $^2\Delta^- \longrightarrow$ X $^2\Pi$	413	430
CH	C $^2\Sigma^- \longrightarrow$ X $^2\Pi$	314	314
CN	B $^2\Sigma \longrightarrow$ X $^2\Sigma$	388	421
FeO	$B_0 \longrightarrow X_0$	579	609
N_2^+	B $^2\Sigma_u^+ \longrightarrow$ X $^2\Sigma_g^+$	391	428
NH	A $^3\Pi \longrightarrow$ X $^3\Sigma^-$	336	336
NO	A $^2\Sigma^- \longrightarrow$ X $^2\Pi$	226	248
OH	A $^2\Sigma^+ \longrightarrow$ X $^2\Pi$	281, 284	312
SiCl	B $^2\Sigma \longrightarrow$ X $^2\Pi$	275, 395	280, 320
SiH	A $^2\Delta \longrightarrow$ X $^2\Pi$	413	413
SiH_2	$\tilde{A}$ ^{2}B $\longrightarrow$ $\tilde{X}$ ^{1}A	580	618
SiN	$\tilde{B}$ $^2\Sigma \longrightarrow$ $\tilde{X}$ $^2\Sigma$	396	414
SiO	A $^1\Pi \longrightarrow$ X $^1\Sigma$	221	248

Table 6: Examples of molecular LIF transitions with molecular transitions, absorption and fluorescence wavelengths.

Species	EET	RET	VET
He	0.0020	2.3	0.013
O_2	1.51	1.7	0.024
N_2	0.0037	2.9	0.20
Air	0.30	2.5	0.16
NO	2.49	4.4	8.8

(7)	$N + O_2 \longrightarrow NO + O$	$3.4x10^{-21}$	12
(8)	$O + N_2 \longrightarrow NO + N$	$3.3x10^{-53}$	12
(9)	$N + OH \longrightarrow NO + H$	$4.6x10^{-17}$	12
(10)	$NO + N \longrightarrow O + N_2$	$3.2x10^{-17}$	12
(11)	$NO + O \longrightarrow NO_2$	$3.4x10^{-17}$	12
(12)	$NO + O_3 \longrightarrow NO_2 + O_2$	$1.2x10^{-19}$	12
(13)	$NO + OH + M \longrightarrow HNO_2 + M$	$3.3x10^{-43}m^6s^{-1}$	12
(14)	$NO + HO_2 \longrightarrow NO_2 + OH$	$6.0x10^{-18}$	12

Table 7: Prduction and loss mechanisms of NO.

6 Atomic Oxygen densities using two-photon absorption laser induced fluorescence

6.1 Introduction

Radials such as H, N, O and F have a major role in plasma chemistry due to their high reactivity [15], with H, N and O the most important species for atmospheric pressure plasmas. The ability to measure locally the density, velocity and temperature of such atomic species is therefore of particular relevance to gain a better understanding of both the dynamics and the kinetics of a given plasma environment.

Using the LIF technique presented in chapter 5 it was possible to determine spatially resolved densities of the molecule NO. However, due to the relatively large energy spacings typically found in atomic species, monitoring of ground state atoms requires the use of highly energetic photons of which generation is experimentally demanding, while other issues such as UV absorption and changing plasma composition in the beam path also exist [100]. The problems associated with single-photon excitation can be over come with the application of a multi-photon excitation scheme. In this chapter, the two-photon absorption laser induced fluorescence (TALIF) is presented as a diagnostic tool to monitor the ground state densities of atomic oxygen produced by the APPJ presented in chapter 3.

6.2 History

The theory of two-photon absorption was first develop in 1931 by Marie Göppert-Mayer [213] in her doctoral dissertation, however like the case described in the LIF chapter, the invention of the laser would not allow the theory to be tested for several decades. In her work based on the theory of two-photon quantum transitions in atoms, she correctly predicted the potential for high intensity light to trigger non-linear interactions.

Experimental work in non-linear optics began in 1961 by Franken *et al.* [214] who showed that when light from a ruby laser at wavelength λ, propagates through a quartz crystal, it generates light at the second harmonic frequency with a wavelength of $\lambda/2$.

The first confirmed case of two-photon absorption was made by Kaiser and Garret in 1961 [215] as they measured a two-photon absorption resonance in a doped calcium crystal ($CaF_2 : Eu_2^+$). Further work also demonstrated that it was possible to use two-photon excitation to excite organic dyes to produce fluorescence. Many examples of two-photon excitation processes have been demonstrated in molecular spectroscopy [216–218], while two-photon spectroscopy has become an important tool to study the electronic structure of molecular excited states [219, 220]. Examples of three-photon excitation have also been demonstrated [221, 222]. The continued increase in commercial laser systems intensities has and will lead to an increase in the range of applications and capabilities of two- and multi-photon excitation processes.

Atom	Transition	λ laser (nm)	λ fluorescence (nm)	Reference
C	$2p^2\ ^3P \longrightarrow {}_3p\ ^3D$	280	910	[223]
Cl	$3p^5\ ^2P^0 \longrightarrow 4p'\ ^2F^0$	210	904	[224]
Cl	$3p^5\ ^2P^0 \longrightarrow 4p\ ^4S^0$	233	725,775	[225]
F	$2p^5\ ^2P^0 \longrightarrow 3p^2D^0$	170	776	[226]
H	$1s\ ^2S \longrightarrow 3d\ ^2D^0$	205	656	[227]
N	$2p^3\ ^4S^0 \longrightarrow 3p\ ^4D^0$	211	869	[228]
N	$2p^3\ ^4S^0 \longrightarrow 3p\ ^4S^0$	207	752	[229]
O	$2p^4\ ^3P \longrightarrow {}_3p\ ^3P$	226	845	[228]
S	$3p^4\ ^3P \longrightarrow {}_4p\ ^3P$	288	VUV	[230]
I	$5p^5\ ^2P^0 \longrightarrow {}_2D^0$	304	VUV	[231]
Xe	$5p^6\ ^1S \longrightarrow {}_6p[\frac{3}{2}]$	250	828	[232]

TALIF was first demonstrated in 1981 by Boker *et al.* [233] for atomic hydrogen and deuterium, and chlorine [234] by the same group in 1982. In the same year, TALIF was also used to detect ground state atomic oxygen and nitrogen by Bischel *et al.* [228]. Since then, TALIF has become a significantly important diagnostic method in low-temperature plasma research and also in the combustion industry.

Table 6.2 gives detailed information about various atomic species detected using TALIF such as the transition probed, laser wavelength and fluorescence wavelength [223–232].

6.3 Mechanism

TALIF is a variation on conventional single-photon LIF. As described in section 5 photon absorption results in the transition of a bound electron from one state to a higher state. The electron in the higher state then spontaneously decays either to its original state, or to a different state. If the electron decays to its original state, a photon of energy equal to the one absorbed is emitted. This is known as resonant fluorescence and is a two-level scheme. If the electron decays to a different state, between the ground state and excited state, a photon of energy equal to the difference between the second and third state is emitted. This is a non-resonant fluorescence and is a three-level state as shown in figure 6.1.

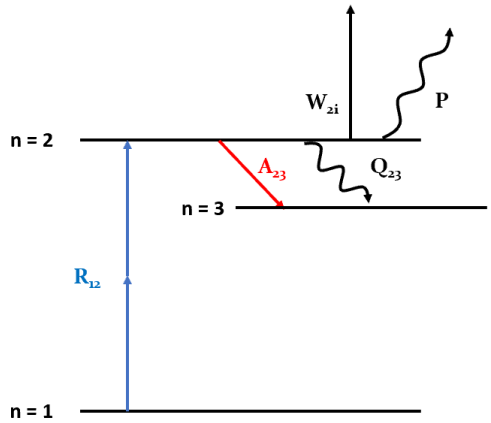

Figure 6.1: Simple three level diagram showing the key processes in two-photon absorption laser induced fluorescence

The absorption of the two photons can be considered simultaneous as the two photons are absorbed within $\sim$ 10 fs of each other. Absorption of the two photons is what pumps the transition. Absorption of the first photon pumps the electron to

a “virtual” state. The second absorption pumps the electron from the virtual state to a real upper state. The virtual state is a linear combination of the wave function of all real atomic levels that combine with the initial state by allowable single-photon transitions. Therefore, there is no requirement for single-photon linked states in order for two-photon absorption transitions. The emission for single- and two-photon LIF is always through a single photon, either back to its original state or to a third.

6.4 TALIF rate equations

Similarly to the single photon LIF discussed in section 5 a relation between the fluorescence signal from species excited by the absorption of two photons and the population of the ground state can be calculated. Like the LIF scenario, the derivation begins with rate equations, however, unlike LIF a three level system is required. A simplified version of this three level system is shown in figure 6.1. A ground state particle is excited from state 1 to 2 through the absorption of two photons at a rate R_{12} and the resulting fluorescence from state 2 to 3 with a rate A_{23}

Assumptions similar to the single photon LIF are also made including negligible photo-ionisation, stimulated emission and inter system crossing. It is also assumed that there is very weak excitation such that the population the ground state, N_1, is assumed to be the total population of the whole three-level system, i.e. $N_1 >> N_2$, N_1 is unchanged. With these assumptions, the change of population rate equations for state 1 and 2 are given by equations 6.1 and 6.2 where A_2 is the total emission rate from the excited state $n = 2$.

$$\frac{\delta N_1(t)}{\delta t} = -N_1(t)R_{12}(t) \tag{6.1}$$

$$\frac{\delta N_2(t)}{\delta t} = N_1(t)R_{12}(t) - N_2(t)(A_2) \tag{6.2}$$

The steady state solution then gives a relation between the measured population in the excited state and the total population

$$N_2 = \frac{R(t)N_1}{A_2} = N_{Total}\frac{R(t)}{A_2} \tag{6.3}$$

It is possible to express the two-photon excitation rate $R(t)$ in terms of the generalized two photon excitation cross-section $\sigma^{(2)}$ [235] given in equation 6.4 where $G^{(2)} = 2$ is the photon statistical factor [236, 237] and $g(\Delta\nu)$ is the normalised line profile given by equation 6.5.

$$R(t) = G^{(2)}\sigma^{(2)}g(\Delta\omega)\left(\frac{I_0}{h\nu}\right)^2 \tag{6.4}$$

$$g(\Delta\nu = 2\nu_L - \nu_A) = g_A(2\nu - \nu_A) * g_L(\nu - \nu_L) * g_L(\nu - \nu_L) \tag{6.5}$$

Integrating equation 6.1 and 6.2 gives new rate equations 6.6 and 6.7 respectively.

$$N_1(t) = N_0 exp\left(-\int_0^t R(t')dt'\right) \approx N_0 \tag{6.6}$$

$$N_2(t) = N_0\int_0^t R(t')exp\{-A_2(t-t')dt'\} \tag{6.7}$$

The optical branching ratio, $a_{23} = \frac{A_{23}}{A_2}$ is defined as the ratio of the number of photons emitted during the transition from the excited state to the third state via fluorescence to the total number of photons emitted form the excited state. It is then possible to obtain the number of photons per unit volume for the fluorescence transition given by equation 6.8.

$$N_F = A_{23} \int_0^\infty N_2(t)dt = N_0 a_{23} \frac{G^{(2)}\sigma^{(2)}}{(h\nu)^2} g(\Delta\nu) \int_0^\infty I_0^2(t)dt \tag{6.8}$$

Finally, if we assume a similar two-photon relationship to the single-photon given by equation , the total fluorescence signal is given by

$$S_{LIF} = V\frac{\Omega}{4\pi}\eta N_{total} a_{23} R(t) \ = V\frac{\Omega}{4\pi}\eta N_{total} a_{23} G^{(2)}\sigma^{(2)} g(\Delta\omega) \left(\frac{I_0}{h\nu}\right)^2 \tag{6.9}$$

Equation 6.9 appears more complicated than the equivalent single-photon fluorescence equation. It has the same total population N_{Total}, fluorescence quantum yield a_{23}, laser excitation transition probability $G^{(2)}\sigma^{(2)}g(\Delta\omega)$, photon flux scaling $(\frac{I_0}{h\nu})^2$ and collection parameters $V\frac{\Omega}{4\pi}\eta$. The only major difference between the single- and two-photon equations is the signal scaling as the square of the laser intensity, which stems from the two-photon excitation process.

6.5 Single photon verses two photon

TALIF has a number of advantages over single photon LIF. TALIF allows direct access to energetic transitions that are linked to the ground state, pumping otherwise forbidden transitions and the possibility of providing Doppler-free measurements. Optical

thickness of is also no longer a concern as there are no single-photon transitions at the laser wavelength. The laser will travel unabsorbed through the medium until the beam intensity becomes sufficient to pump the transition, through beam focusing or overlapping counter propagating beams.

Most atomic ground state transitions lie in the VUV range (<200 nm). Light sources with the ability to produce the wavelengths necessary to pump these transitions are difficult to find, while optical components necessary to control these wavelengths are even more difficult to find and rather expensive. To overcome these challenges, with two-photon absorption, each photon provides a portion on the energy required to pump the transition. The two photons do not have to have equal wavelengths. As long as the sum of the energies from each photon equals the transition energy, such that $E_1 + E_2 = E_T$, where E_1 is the energy of one photon, E_2 the energy of the second photon and E_T the energy of the transition given $E = \frac{hc}{\lambda}$. For example, a 193 nm and 218 nm photon was used to pump the Ly_β transition in hydrogen. Such an experiment requires two lasers. In practice it is much more simpler and practicable to use a single laser producing two photons of equal wavelength. Using two photons makes it possible to access high energy transitions from the ground state that are not normally reachable with a single-photon source.

6.5.1 Strengths of TALIF

Two-photon LIF has a number of advantages over single single-photon experiments. TALIF offers the ability to access transitions that lie in the vacuum ultraviolet (VUV) region of the spectrum. Many commercial laser systems are now able to produce

tunable radiation to 200 nm and below. There are however many atomic and molecular species of interest to many disciplines including combustion, biomedical and materials processing that have very large single-photon cross-sections that lie below the 200 nm threshold in the VUV. This constraint is made more prohibitive if the application is in an oxygen rich environment due to the strong absorption of molecular oxygen in this spectral range. The solution to this is to utilize a multi-photon excitation scheme.

Rather than using a single photon with transition energy

$$E = h\nu_{1photon} = \frac{hc}{\lambda_{1photon}} \tag{6.10}$$

two photons with half the frequency or twice the wavelength are used such that

$$E = h\frac{\nu_{2photon}}{2} = \frac{hc}{2\lambda_{2photon}} \tag{6.11}$$

which can be generalised to $\nu_{1photon} = 2\nu_{2photon} = \ldots = n\nu_{n-photon}$ up to n photons. This is shown graphically in figure 6.2 for atomic oxygen. Two- and three-photon excitation at 225.58 nm and 338.37 nm, respectively, are used to excite the $n = 1$ to $n = 2$ that pass through virtual states and result in subsequent fluorescence to the $n = 2$ state. These UV photons are not as readily absorbed as lower wavelengths, while also are more easily produced. There are however different selection rules for each excitation scheme. In equation 6.4 we saw that the excitation rate is a product of both excitation intensity and absorption cross-section. To overcome the small absorption cross-section, very intense laser pulses are required, which can result in the TALIF signal no longer being linear with respect to laser intensity, while also impacting the reliability of the calibration procedure, see section 6.8. Using focussing optics and high

quantum efficiency collection devices such as a photo-multiplier tubes (PMT), it is possible for sufficiently high laser intensity to be generated at the laser focal volume for a signal to be generated and detected.

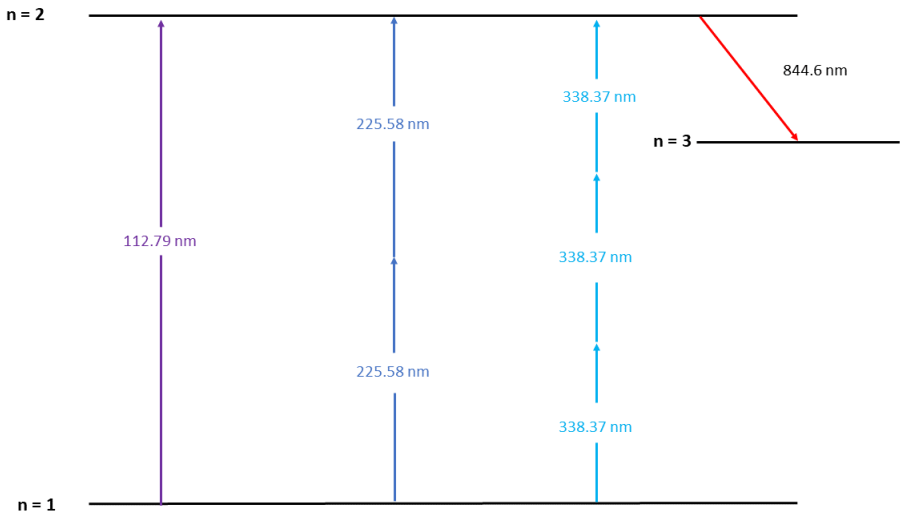

Figure 6.2: Energy level diagram for single-, and multi-photon excitation approaches for the n = 1 to n = 2 excitation for atomic oxygen. Each approach has the same excitation energy that subsequently results in the fluorescence to the n = 3 state.

6.5.2 Weaknesses of TALIF

The strengths of multi-photon absorption also lead into its weakness. It is typically easier for most commercial lasers to produce longer wavelength photons than those in the UV region with shorter wavelengths. However, moving from single-photon to multi-photon excitation results in the absorption cross-section becoming increasingly smaller. The resulting trend is so significant that the production of two or three photons for excitation is so inefficient that the benefit of more efficient photon production is

outweighed by the inefficient excitation.

6.6 Selection rules

The case for single-photon absorption, a single quantum of momentum is absorbed. The selection rules are therefore $\delta l \pm 1$, with l is the quantum number for orbital angular momentum. For two-photon absorption, two quanta of momentum are absorbed and the selection rules change to $\delta l = 0, \pm 2$. This therefore allows transitions between states that are not coupled by single photon transitions, i.e. $ns- > ms$ and $ns- > md$, where n and m are the principle quantum numbers and s and d are the orbital angular momentum quantum numbers.

The selection rules are satisfied by the laser polarisation. Absorption of two photons with a single polarization satisfies $\delta l = 2$, while the absorption of two photons with opposite polarization satisfies $\delta l = 0$. This can be important when two or more transitions lie near each other. Even with narrow bandwidth lasers, if the transition is too small, the laser will pump both transitions, leading to broadening of the absorption line width. However, due to the polarization dependent selection rules, it is possible for only one transition to be pumped and therefore remove the extra broadening.

6.7 Experimental set-up

Within this section the experimental set-up for TALIF measurements is described. The two-photon transition used to measure the TALIF signal on atomic oxygen is the $2p^3p_2 \rightarrow 3p^3P_2$ transition with a corresponding wavelength of 225.582 nm [238]. The

measured fluorescence signal is from the $3p^3P_2 \rightarrow 3s^3S_1$ transition with a corresponding wavelength of 844.6 nm

6.7.1 Laser system

To produce the necessary wavelength required to pump the TALIF transition, an Innolas Spitlight 600 Nd:YAG laser system was used. The laser has a bandwidth of < 0.03 cm^{-1} and operates at a frequency of 10 Hz. This laser produces light at a wavelength of 1064 nm. The second harmonic of the Nd:YAG laser was used to pump a Radiant Dyes Narrow Scan dye laser. The second harmonic produces light at a wavelength of 532 nm with a pulse width of ~ 8 ns.

A dye mixture of DCM/Pyridine 1 in methanol was used in the Dye laser. This produced a useful lasing wavelength range of 640-750 nm. This output radiation passed through a set of frequency doubling and tripling crystals before passing through a Pellin Broca prism system that separated out the required UV radiation of approximately 225.582 nm from the fundamental and doubled wavelengths.

6.7.2 Optics and beam control

Due to the confinements of the laboratory and the location of the laser relative to the fume cupboard it was necessary to navigate the beam towards the plasma jet. To guide the beam towards the plasma system two UV graded optical prisms were used. Optical prisms allowed the beam to be guided towards the plasma jet with minimal losses in laser power when compared to a similarly graded mirror. The transmission at 226 nm for UV fused silica is 90 % while a similarly graded mirror has a reflectance less than

80 %. A schematic representation of the experimental set-up is shown in figure 6.3.

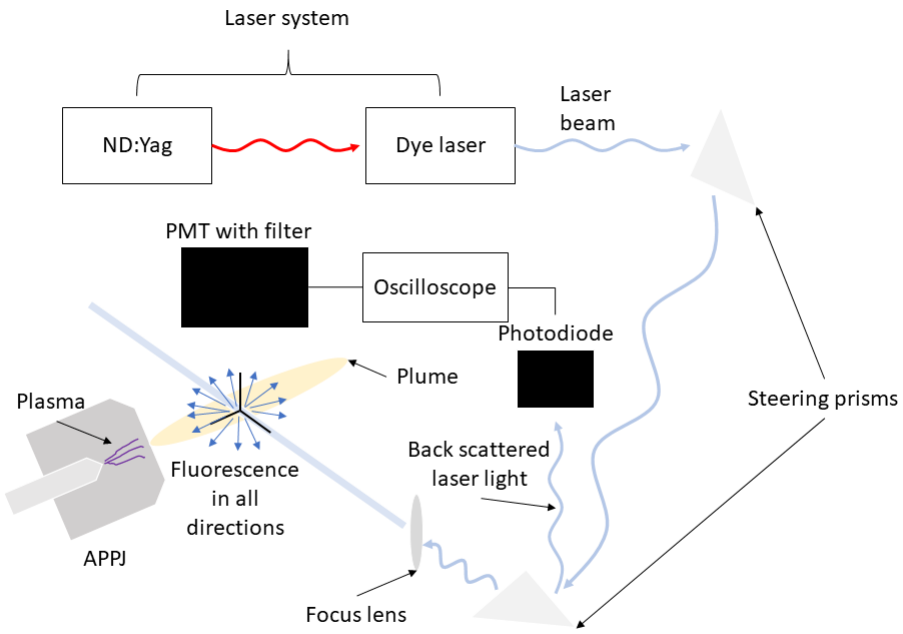

Figure 6.3: Schematic representation of the TALIF experimental setup.

The beam was focused into the plasma plume at a distance of approximately 1 mm from the jet orifice using a UV graded garde fused silica plano-convex lens with a focal length of 438 mm. A back reflection from the focusing lens was steered towards a ThorLabs Det210 fast photo-diode connected to an oscilloscope. The signal detected by the photo diode was used to trigger the oscilloscope while also monitoring the laser intensity for normalisation of the TALIF signal. A Hammamatsu R636-10 photomultiplier tube (PMT) with a rise time of 2.2 ns orientated orthogonally to the laser beam path and plasma plume, was used to detect light that was generated through the TALIF process. A LOT-Oriel optical bandpass filter centred at 844 nm with a 0.8 nm bandwidth was placed at the entrance of the PMT to attenuate all light except at

the fluorescence wavelength. The PMT signal was recorded on an oscilloscope.

6.8 Calibration

Similarly to the LIF work in order to determine an absolute number density, calibration must be preformed. The typical method used to calibrate is to use a noble gas scheme first proposed by Döbele et. al. A noble gas with excitation and fluorescent transitions similar to the gas under investigation is chosen. For atomic oxygen, xenon is used, atomic nitrogen uses krypton and for the case of atomic nitrogen both argon and atomic fluorine are sufficient.

The two-photon resonant states of the reference gases must be sufficiently close to those of the gas under investigation in order to properly assume identical excitation conditions. The conditions of excitation and detection should be as similar as possible, including the laser output properties and the optical set-up. Only the unsaturated quadratic signal response gives a qualitative comparison.

For atomic oxygen xenon gas is used. Xenon gas has similar excitation and fluorescent wavelengths to atomic oxygen.

There are however a number of known problems associated with this calibration technique. One requirement is that the laser power dependence of the TALIF signal be the same for both the measurement and calibration processes. To ensure this is the case, the laser must operate in the linear region, where the TALIF signal varies in a quadratic manner with laser power during both calibration (Xe) and measurement (O). Typically low laser pulse energies (10 s - 100 s μJ per pulse) are used to ensure

this. At low pressures this method works well, however at atmospheric pressure, strong quenching of the excited state depletes the population in the upper level before emission is possible, thereby significantly reducing the TALIF signals [239]. To compensate for the reduced TALIF signal the laser power can be increased, but may result in the signal moving outside the TALIF quadratic region, complicating the analysis as the calibration and measurement TALIF signals many no longer have the same laser power dependence [100]. Two-photon absorption laser induced stimulated emission (TALISE), ground state depletion and resonance enhanced multi-photon ionization (REMPI) are also present at high laser powers. In oxygen rich environments photolysis of molecular oxygen can also lead to an increase in signal as these laser produced molecules can also be excited and produce fluorescence.

Therefore it is vitally important that the excitation of the ground state atoms, the resonance transition of the reference species is sufficiently close to the resonance transition of the probed species. This will allow for the assumption to be made that identical excitation conditions for the spatial, temporal and spectral intensity of the laser radiation. In addition, the laser intensity must be kept sufficiently low so that the signal intensity as a function of laser energy obeys the same scaling laws for both the reference transition and the probed transition [235].

When these conditions are met, the unknown atomic ground state number density n_x is given by

$$n_\chi = \frac{T_R \eta_R}{T_\chi \eta_\chi} . \frac{\sigma_R^{(2)}}{\sigma_\chi^{(2)}} . \frac{a_R}{a_\chi} (\frac{h\nu_\chi}{h\nu_\chi})^2 \frac{S_{chi}}{S_R} n_R = \chi \frac{S_\chi}{S_R} n_R \tag{6.12}$$

with S the normalised fluorescence signal (integrated over fluorescence wavelength, excitation wavelength and interaction time and normalised to the square of the laser pulse energy), photon energy $h\nu$, the effective branching ratio a of the observed fluorescence transition, T the transmission of the detection optics, the detectors quantum efficiency η and the two-photon excitation cross section $\sigma^{(2)}$.

Another method that can be used to calibrate the TALIF signal is through the use of photolysis as outlined by Conway *et al* [100]. In this method the species under investigation is both the calibration and measurement species, which has several advantages. Since both the calibration and measurement procedures are preformed using identical wavelengths; the spatial, temporal and spectral intensity distributions will be the same in both cases. As a result there will be no issue with variations in the laser performance when operated at different wavelengths.

The fluorescence wavelength produced by both the calibration and experiment will also be the same, therefore eliminating the associated error due to different detector sensitivity at different wavelengths. In addition the optical bandpass filter used to attenuate background light from reaching the detector will only have to cater for one wavelength, therefore meaning the that the bandwidth of the filter need only be wide enough to accommodate the line width (FWHM $<$ 1 nm) of the resulting fluorescent line. A narrower bandwidth also increases the signal-to-noise ratio by reducing the amount of background light entering the detector.

A final advantage to this calibration approach is allowing the laser to operated at higher powers. Any saturation affects such as REMPI, that occur will be identical

in both the calibration and experiment procedure. The laser power dependence of the TALIF signal will remain the same even at higher laser powers. Operating the laser at higher energies will also produce stronger TALIF signals, counteracting the issue of weak TALIF signals typically encountered by ns pulsed lasers that use xenon calibration in atmospheric pressure plasma systems.

The dissociative energy of molecular oxygen is 5.17 eV, and when photons with this energy or more are absorbed by O_2, the dissociation rate is 100 %. The atom oxygen density produced by a laser pulse during the photolysis is given by the expression:

$$[O] = 2[O_2](1 - e^{(-\sigma\phi))} \tag{6.13}$$

where σ is the photo-dissociation cross section at a given laser wavelength (λ_{laser}), and ϕ is the photon fluence given by the equation:

$$\phi = \int_0^t \frac{I_0(t)}{hf} = \frac{E_{pulse}}{hfA} \tag{6.14}$$

where E_{pulse} is the laser pulse energy, f is the laser frequency, h is Planks constant, A is the area of the laser focal spot and $I_0(t)$ the laser beam intensity. Single photon absorption in the Herzberg continuum results in photo-dissociation of O_2 producing two ground state O($^3P_2$) atoms. For a laser intensity of 2 x 10^4 W m^{-2} per pulse, the laser photolysis yields an oxygen density $[O]_{cal}$ of 7.12 x 10^{19} m^{-3} per pulse with an estimated error of 21 % caused mainly by laser fluctuations.

Using equation 6.15, the fluorescence photon density η_{fCal} due to a steady state uniform oxygen density can be determined [100] which also takes into account the fact

the atomic oxygen density produced by photolysis will increase over the course of the laser pulse.

$$n_f = \frac{A_{ij}}{A_i + Q_i} \frac{\sigma^{(2)}}{(hf)^2} G^{(2)}(\omega) \, [O] \int_0^t I_0^2(t) dt \tag{6.15}$$

where A_{ij} is the transition rate of the upper level for the fluorescence wavelength, A_i is the total transition rate from the upper level i, Q_i the quenching coefficient of the upper level, f the laser frequency, $\sigma^{(2)}$ is the two-photon absorption cross section, $G^{(2)}$ the photon statistic factor, $g(\omega)$ is the normalised line profile, $[O]$ is the atomic oxygen density and $I_0(t)$ is the laser intensity.

The atomic oxygen density [O] can be determined using photolysis by

$$[O] = \chi \frac{S_O}{R_z R_t S_{Cal} [O]_{Cal}} \tag{6.16}$$

where S_O and S_{Cal} are the atomic oxygen TALIF signals integrated with respect to time, fluorescent wavelength, excitation wavelength and normalised to the square of the laser pulse energy, S_O is the TALIF signal produced by atomic oxygen in the plume and S_{Cal} is the TALIF signal produced by the photolysis calibration. $[O]_{Cal}$ is the total atomic oxygen density generated at the focal point by the laser. R_z and R_t are correction factors for the spatial and temporal variations in the photolysis atomic oxygen density.

6.8.1 REPMI

Resonance enhanced multi photon ionization (REMPI) is always present in TALIF experiments and may be used as an alternative method for atomic detection. The process

is caused by the absorption of a third laser photon in the same laser pulse after initial excitation to a higher electronic state which ionizes the particle creating an electron ion pair. The resulting electron can be detected through avalanche multiplication using the opto-galvanic technique in the discharge or directly when the atom is detection is performed in a flowing discharge in a region without the plasma []. Charges created as a result of REMPI can be related to the ground state species concentration as described in the modelling of laser-atom interactions.

6.8.2 TALISE

Another process that is always present in TALIF experiments is two-photon absorption laser induced stimulated emission (TALISE). TALISE occurs in TALIF experiments when laser flux is sufficient to create a population inversion between in the $n = 3$ and $n = 2$ states. The TALISE effect is from the amplification of TALIF emission in an active medium in a preferential direction.

In TALIF experiments TALISE introduces an additional mechanism for the de-population of excited level n_3 that is added to the spontaneous emission, ionization and collisional quenching and in certain conditions may create non-linear dependence between TALIF and the population of the ground state atoms or molecules.

6.9 Results and discussion

The results of the TALIF investigation are presented in this section. As mentioned in the calibration section, it was not possible to detect a TALIF signal from the laser induced photolysis as a means to calibrate the signal due to losses in the steering optics.

As such the results are un-calibrated and instead show trends in how the atomic oxygen signal behaved while varying the various parameters investigated.

6.9.1 Axial position

As per the NO measurements discussed in section 5, the APPJ was positioned on an adjustable translational stage. The beam was initially aligned such that it passed as close to the jet orifice as possible without hitting the jet nozzle. In practice this was achieved by starting with the jet far away from the beam and then drawing it in towards the beam while monitoring the beam position, relative to the jet. Once the beam to jet position was established, the plano-conex was lens was roughly aligned. The focal point of the beam was then found by using initially using laser paper to view the beam, and then a metallic strip to hear scintillations produced by the beam interacting the strip. The lens position was then adjusted so that the focal point of the beam crossed where the plasma would be once ignited.

An alignment procedure was then preformed to ensure that the plasma did not drift relative to the beam, see figure 6.4. A piece of laser paper was placed behind the plasma and at an angle. When the both the plasma and laser were turned on it was possible to see both and their relative positions. Then as the plasma jet was pulled away from the beam using the translational stage it was possible to determine if any drift occurred during the displacement which could be adjusted by altering the laser beam, jet angle or tilt based on the drift.

Initially the atomic oxygen levels were investigated along the plume in 5 mm intervals but it was found that signal dropped off too quickly, so this was revised to 1 mm

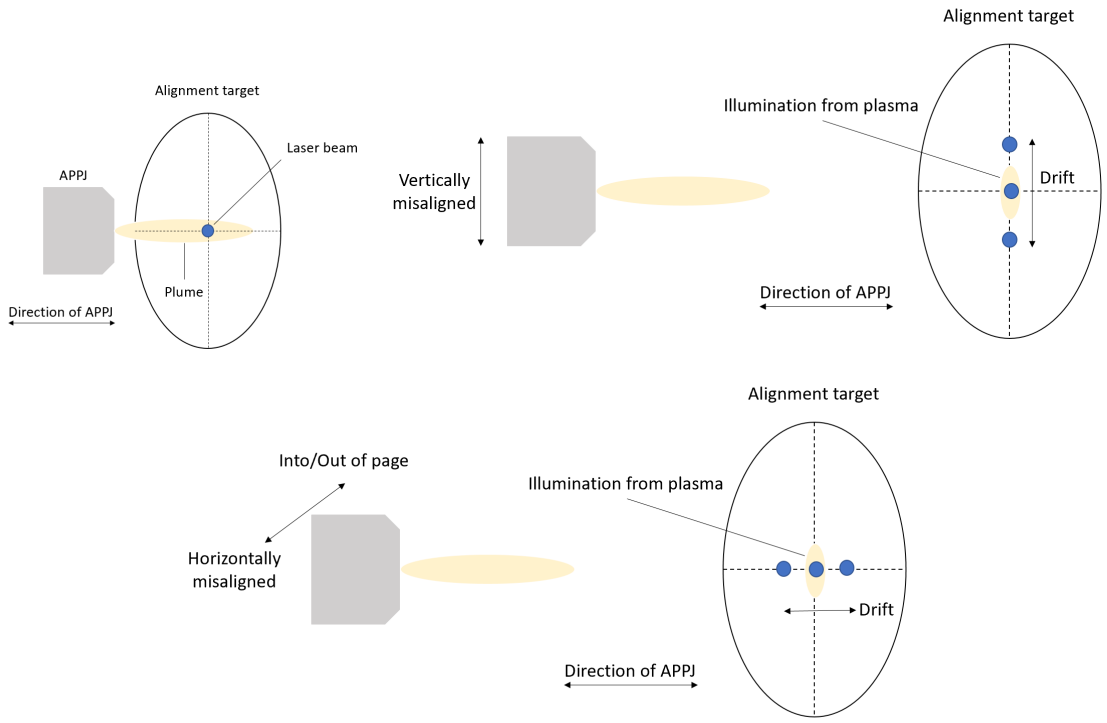

Figure 6.4: Alignment procedure to ensure that the laser beam intersected with the plasma plume during TALIF experiments.

intervals, until the signal dropped off. This was found to be approximately 8 mm from the jet orifice, depending on the experimental conditions.

The TALIF signal trends are shown in figure 6.5. The signal peaks 2 mm from the jet orifice before plateauing 3-4 mm from the orifice and then gradually declining further from the jet, eventually extinguishing beyond 8 mm from the APPJ.

Atomic oxygen is a highly reactive atom, involved in many atmospheric many reactions, so it was not expected to last very long outside of the plasma and the results verify this. The OES experiments showed that atomic oxygen was created by the plasma.

It is interesting to speculate whether or not atomic oxygen is being generated in the

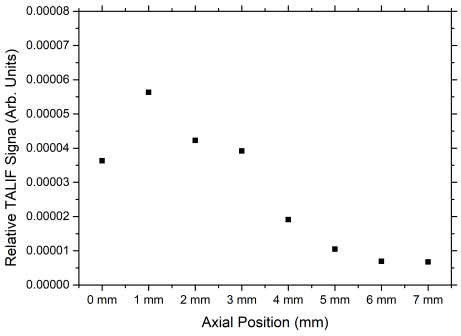

Figure 6.5: TALIF signal trends for atomic oxygen along the plume in 1 mm intervals. The signal peaks 2 mm from the jet orifice before gradually decreasing in intensity further from the jet. Beyond 8 mm from the jet it was no longer possible to detect a TALIF signal

APPJ plume, or the particles detected are transported from the inside of the jet. The lower signal close to jet orifice could indicate that oxygen is being split in the plume region, creating more atomic oxygen. A possible cause in the reduction in the signal is reflections from the jet itself or some of the solid angle being cut off as the jet is too close to the beam, reducing the overall signal.

If atomic oxygen is being generated in the plume region an energy mechanism must be considered. The laser beam itself is excluded from discussion due to always being present in experiments but also since no photolysis signal was detected. Ions and electrons can also be ruled out. The recombination rate for electrons and ions is 10^{-6} cm^3 s^{-1} [240–242] at atmospheric pressure. The ion and electron density decreases too quickly for their to be a notable influence on atomic oxygen generation in the plume region of the plasma.

Metastable species are worth considering as a means of energy transport into the

plasma plume region. Metastables are excited species with long life times due to their resonant radiative transitions into the ground state being prohibited. For most work involving atmospheric pressure plasmas, helium is the dominant metastable. Helium metastables carry energy greater than 19 eV and therefore have sufficient energy for excitation of ground state atomic oxygen ($E_{o(3p^5P)} > 10$ eV). However, even in pure helium environments, at atmospheric pressure the effective lifetime of He$*$ has been experimentally shown to be as short as 6.7 μs due to collisions with helium ground state atoms and formation of helium excimers [243, 244]. Furthermore the presence of impurities such as N_2 reduces the mean lifetime to 2 μs [245]. The presence of oxygen also rapidly de-excites metastable helium states [246], so that the effective lifetime drops below 0.1 μs [237]. It can therefore be concluded that helium metastates are not responsible for the generation of atomic oxygen within the plume region of the plasma.

Another possible source of energy to generate atomic oxygen in the plume region is VUV radiation from the discharge region of the plasma. In [247] it was concluded that the generation atomic oxygen in the effluent of the APPJ was caused by VUV created in the discharge region of the APPJ. In their work radiation as low as 120 nm was detected, while atomic oxygen particles were detected as far away as 10 cm from the APPJ nozzle using TALIF and excited atomic oxygen was also detected using OES also as far away as 10 cm. They also reported number densities in the order of 10^{16} cm^{-3} close to the jet's nozzle. O_2 dissociates at energies ≥ 5.16 eV, corresponding to a wavelength $\lambda \leq 240$ nm. A likely source of this radiation is the Schumann-Runge bands of O_2 and the atomic oxygen line at $\lambda = 120$ nm [247].

In this work, OES measurements showed no VUV radiation in the plume region, so it can be concluded that the plume is not a source of radiation in the UV region. The spectrometer used in the OES experiments does not have the required optical range to detect any radiation below 200 nm, so a different method is required to measure deep UV radiation. This could be possible by directing the light through a UV transparent window, such as UV fused silica or MgF_2, located in front of a monochromater and placing a photomultiplier tube at the excite of the monochromator. Using this method it could be possible to detect the signal intensity as a function of wavelength in the deep UV region of the spectrum. Although, the monochromater may need to be in vacuum to detect these photons.

In all likely hood, atomic oxygen is unlikely to be generated in the plume region of the plasma, due to the steep drop off in TALIF signal intensity beyond 7-8 mm from the APPJ orifice and the lack of detection of excited atomic oxygen species within in the plume region.

6.9.2 Power

Again, similarly to the single-photon LIF, the power delivered to the APPJ was investigated. From the plume measurements, it was determined that the optical place for the beam to be placed was 2 mm from the jet orifice. TALIF measurements were then preformed while varying the voltage to the plasma. This was done in 10 step intervals from 100 % to 60 %.

The trends detected doing the voltage measurements are shown in figure 6.6. The signal was strongest when the voltage dial was set to 100 % and decreased as the

voltage was decreased. This trend does not follow the observation made in the OES chapter, although OES does not provide any information about the number density of unexcited species unlike TALIF. The measurements were also taken at two different regions of the APPJ; OES in the plasma proper and TALIF in the plume region.

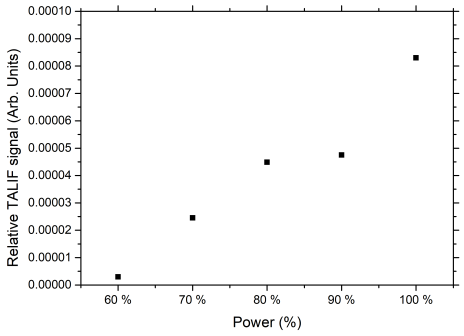

Figure 6.6: TALIF atomic oxygen trends while varying the power delivered to the APPJ.

It was expected that higher voltages would produce a higher amount of O and the trends confirm this. This is believed to be due to electrons gaining higher energies through higher voltages, resulting in higher levels of O_2 dissociation through direct electron impact and also molecular dissociation. As the voltages were decreased then electrons gained less energy and were therefore less able to create atomic oxygen.

There is also the possibility that there may be a slight plateau observed between 80 - 90 % that may also indicate that some internal chemistry is taken place affecting the amount of O reaching the plume.

6.9.3 Flow rate

Figure 6.7 shows the trends observed while varying the flow rate through the APPJ. Unlike the case with the NO LIF in section 5 airflow had a defined impact on the amount of light emitted. At lower flow rates the signal was most intense and decreased as the airflow increased.

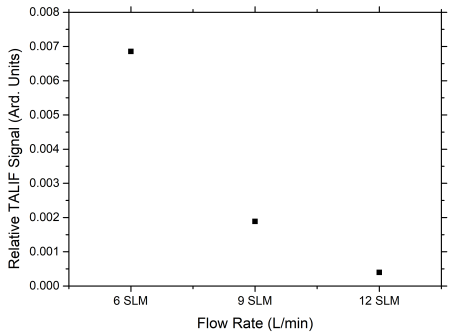

Figure 6.7: TALIF atomic oxygen trends while varying the gas flow rate through the APPJ.

It can be argued that this is either due to atomic oxygen moving faster through the laser system than it is replaced unlike the case with NO or other processes such as quenching or some chemical reaction. O leaving the laser interaction volume quicker than it can be replaced at higher flow rates is the simplest solution. O is lighter than NO so should travel faster, as velocity scales as the square root of mass. The interaction volume of the laser was also smaller for TALIF than it was for LIF so there is the possibility that atoms close to the interaction volume are unaffected, and then pass through the volume between laser pulses due to their increased speed. This however is unlikely as the relative change in velocity will probably not be large enough to have

any notable impact.

Instead quenching or some chemical reaction is more likely the cause of the decrease in signal. NO levels remained relatively stable while the airflow was varied, so it is unlikely that O is being lost to this process. There are two reactions important to the role of NO and O recombination

$$O(^3P) + NO + M \longrightarrow NO_2 + M$$

$$O(^3P) + NO_2 \longrightarrow NO + O_2$$

These reactions could explain the relativity stable behaviour of NO and the reduction of O levels as NO is both removed and then subsequently reformed in the reactions, while O is removed. There is also the consideration that O is bonding with O_2 to create ozone also reducing the signal.

6.10 Conclusions

Throughout this chapter we have investigated two-photon absorption laser induced fluorescence as an experimental method to detect atomic oxygen in the plume region of an atmospheric pressure plasma jet. Initially an introduction to the topic was given including the historical development laser induced fluorescence. The mechanism of TALIF was also introduced and a set of rate equations developed.

The differences between signal and two-photon LIF were also discussed, outlining the key differences between the two and when it is useful to use one over the other, typically this is when the energy of the transition to be probed is too high to be generated using conventional laser systems. The strengths and weaknesses of TALIF

were also discussed with the key strengths being that it is possible to probe transitions that lie in VUV region that would not be possible using a single photon. The main weakness being that the cross-section for two-photon absorption is typically much smaller than it is for a single photon transition.

The experimental set-up was also discussed included the method used to calibrate the signal. A brief description of the laser system and the steering optics were given. Processes that can result in the signal strength varying such as REMPI and TALISE were also described.

Using the TALIF method it was possible to detect a signal emitted from atomic oxygen, however it was not possible to produce a calibration signal and therefore all results shown are trends in the signal and not absolute number densities.

It was however found that the signal diminished quickly once the laser moved away from the APPJ indicating that atomic oxygen does not travel far from the orifice unlike the case with NO. By varying the voltage and airflow it was also possible to observe a change in the trend in the light emitted as LIF.

For the flow rate experiment it was that increasing the airflow through the APPJ the signal trends decreased. Several explanations were offered to explain this trend, but without calibration it is not possible to say conclusively which it is, although it is the belief that some chemical reaction involving NO, NO_2 or O_3 is responsible.

By varying the voltage it was also possible to change the signal strength observed. At higher voltages the signal detected was largest and decreased as the voltage was decreased. A possible plateau was observed which could indicate a change in the

plasma behaviour and chemistry or may be an experimental error. Again, though without calibration it is not possible to say conclusively what the cause of this trend is.

7 Conclusions and Future Work

Throughout this work an atmospheric pressure plasma jet was designed and built, while it's chemical, optical and electrical characteristics were investigated.

In chapter 2 the physics and background of APPs were presented. This work was undertaking to explain the basic underlying principles of plasmas with an onus on those at atmospheric pressure. The underlying theory surrounding how plasmas develop was presented and then expanded to account for those that operated at atmospheric pressure. The parameters that define a plasma were also presented: Debye length, plasma frequency and plasma parameter.

In chapter 3 the plasma jet used throughout this study was introduced. The components used to run the APPJ such as the high voltage power supply and the air flow control were described.

Three modes of operation were observed throughout the investigation. A non-plasma capacity load was observed electrically when the APPJ was operating at voltages too low to ignite a plasma. While the plasma was active two modes of operation were observed and named the noisy and quite modes based off their observed audible behaviour. Electrical characterisation revealed the difference features of both of these modes. While in the quite mode of operation the plasma experienced one voltage drop per voltage cycle with a corresponding current peak. The voltage drop occurred during the negative half cycle of the voltage cycle. While in the noisy mode of operation the plasma experienced two voltage drops per voltage cycle, one in the positive half cycle and one in the negative half cycle each with their own corresponding current spike.

In chapter 4 the emission properties of the plasma were investigated using the experimental method optical emission spectroscopy.

Initially the basics of radiative emission theory was presented and the key components that make up a spectroscopic system. The unique spectra of the APPJ was presented and the major features were described. Experiments varying the control parameters of the jet showed that it was possible to control the intensity of the emissions from the plasma.

Five peaks were monitored as the control parameters were altered and it was found that the APPJ again seemed to have two distinct operating modes. In the case of each peak monitored a description of the various paths of formation and removal was discussed.

In chapter 5 the experimental procedure laser induced fluorescence was presented in order to detect nitric oxide within the plume region of the plasma.

Initially the theory of laser induced fluorescence was presented and this included the derivation of set of rate equations. In this chapter it was experimentally confirmed that nitric oxide was present in the plume region of the plasma. By calibrating the the signal it was also possible to calculate the absolute number density of nitric oxide in the plasma. It was also confirmed experimentally that it was possible to alter this level by varying the control parameters of the plasma.

In chapter 6 the experimental procedure of two-photon absorption laser induced fluorescence. Similarly to the LIF chapter the basic theory of the TALIF was presented and a set of rate equations derived. The differences between TALIF and LIF

was also outlined and the strengths and weaknesses of TALIF. Experimentally it was confirmed that atomic oxygen was present in the plume region of the plasma. An alternative approach to calibration was utilized by photolysis generated by the laser plume, however this approach was unsuccessful and it was not possible to determine the absolute number density of atomic oxygen in the plume region. It was however possible to detect trends in the signal strength by again varying the control parameters of the atmospheric pressure plasma jet.

7.1 Future work

The electrical study of the APPJ was interesting due to the unique behaviour of the APPJ and should be expanded. The current spike measurements that were completed for the airflow should be expanded for both voltage and electrode position to complete the picture. It was envisioned to also preform these measurements while OES measurements were being made so as to attempt to link the two behaviours and identify any trends.

A numerical simulation of the APPJ could reveal the behaviour of the charged particles produced by the plasma and their location between the powered and ground electrode throughout the voltage cycle. Of most importance is to try and understand the distribution of charged particles. Knowing this will make it possible to determination the electric field within the plasma and could explain the difference between the noisy and quite modes of operation or the voltage drop observed after the current spike.

The OES measurements were quite revealing but can also be expanded. The resolution of the spectrometer used was too large to provide any meaningful information about the plasma such as gas temperature, electron temperature and ion density. To do this a higher resolution spectrometer is needed, to allow the smaller scale features of the nitrogen second positive system to be resolved. This will allow the rotational temperature to be determined by comparing the ratios of certain peaks within the spectrum. At atmospheric pressure, the rotational temperature of nitrogen molecules is approximately equal to the gas temperature. This could be achieved by using a monochrome to select a specific wavelength and measuring the light using a PMT. By using the monochromator to tune the specific wavelength of light measured it may be possible to build up a profile of the intensity of the light verses wavelength with high enough resolution to calculate the gas temperature.

In addition to this, it will be a worthwhile endeavour to do temporal OES measurements of the plasma if possible. By understanding the temporal behaviour of the plasma, i.e. how the light emitted from the plasma varies over the course of the applied voltage cycle it may be possible to understand the mechanics of the plasma better. As discussed in the OES section, many of the excited species detected arise from secondary or later reactions within the plasma. By determining if there is a temporal behaviour of the excited species, it should be possible to understand how the plasma chemistry changes. For example, we know through OES and TALIF measurements that atomic oxygen is produced by the plasma and is present within the plume region. We also know through LIF measurements that the plasma produces NO. For example is all the

energy of the electrons initially coulped to vibrational states of nitrogen, before being released through emissions,

Unfortunately the calibration method used for the TALIF atomic oxygen measurements was unsuccessful for recording absolute number densities. Not enough optical power was focused into the one point to produce both cathylsis of molecular oxygen into atomic oxygen and also excite the atomic oxygen as per the TALIF method.

Two potential solutions exist to calibrate the data. Increasing the optical power of the laser beam within the focal point of the beam or using the traditional but more expensive Xenon gas calibration method. Increasing the optical power of the laser can be achieved in several ways. Increasing the supply voltage of the flash lamp while increase the optical output but at cost of potential damage to the flash lamp. The dye laser can be fully optimized over a very narrow window to produce optimal signals. The laser was also in the process of undergoing a realignment process before the Coronavirus pandemic, which would have also increased the lasers output. Furthermore, more optics could have reduced the beam waist of the laser, resulting in a narrower, tightly compacted focal point with more energy per unit volume.

Increasing the optical output of the laser is the preferred method for calibration. However if this cannot be achieved then it might be worthwhile to consider the traditional method of calibration using Xenon gas.

It is possible to expand the LIF and TALIF work to incorporate further gaseous species. OH is extensively studied in the literature. However calibration is difficult, often requiring a further experimental procedure to correctly calibrate. It is also possi-

ble to use the TALIF method to detect atomic nitrogen although this method typically requires pico second lasers or better.

Preliminary absorption experiments produced promising initial results. Two LEDs, 250 nm and 310 nm, chosen so their peak emission corresponding to an absorption peak of OH (310 nm) and O_3 (255 nm) were initially picked for this work. A feasibility study using two LEDs with wavelengths of 250 nm and 310 nm showed a noticeable drop in signal intensity when light from the LEDs passed through the plume and was collected using a spectrometer.

The 310 nm LED, used in conjunction with OH LIF would give a very strong indication of OH levels in the plume. 255 nm is also possible to detect ozone. Ozone and NO are competing chemical molecules so an abundance of one molecule should result in a depletion of the other and the formation of NO_2 and atomic oxygen.

References

[1] Kelly S. Generation and control of reactive species in low temperature atmospheric pressure plasma sources. Dublin City University; 2014.

[2] Raizer YP. Gas Discharge Physics. Berlin: Springer; 1991.

[3] Lu X, Naidis GV, Laroussi M, Ostrikov K. Guided ionization waves: Theory and experiments. Phys Rep. 2014;540:123–166.

[4] Leal-Quirós E. Plasma processing of municipal solid waste. Brazilian J Phys. 2004 dec;34(4b):1587–1593.

[5] Levitin G, Reinhardt K, Hess DW. Plasma Cleaning for Electronic, Photonic, Biological, and Archeological Applications. In: Dev. Surf. Contam. Clean. Contam. Remov. Monit. Elsevier Inc.; 2012. p. 55–121.

[6] Lofthus A, Krupenie PH. The spectrum of molecular nitrogen. J Phys Chem Ref Data. 1977 jan;6(1):113–307.

[7] Nascimento JC, Aragão ECBB, Fernandes AD, Barbosa FTF, Costa LMS, Sousa DC, et al. Optical Measurements of an Atmospheric Pressure Microplasma Jet Aiming Surface Treatment. Am J Condens Matter Phys. 2014 jun;4(3A):8–18.

[8] Wiese WL, Smith MW, Glennon BM. Atomic Transition Protablities Volume I. Washington, DC: United States Department of Commerce, National Bureau of Standards; 1966.

[9] Abbasi-Firouzjah M, Hosseini SI, Shariat M, Shokri B. The effect of TEOS plasma parameters on the silicon dioxide deposition mechanisms. J Non Cryst Solids. 2013 may;368:86–92.

[10] Lock EH, Fernsler RF, Slinker S, Walton SG. Experimental and Theoretical Estimation of Excited Species Generation in Pulsed Electron Beam-Generated Plasmas Produced in Pure Argon, Nitrogen, Oxygen, and Their Mixtures; 2011.

[11] Mavadat M, Turgeon S, Ricard A, Laroche G. Infrared optical actinometry to determine N- and H-atom density in a N 2 –H 2 microwave discharge. J Phys D Appl Phys. 2012 aug;45(31):315201.

[12] Charoux CMG, Free L, Hinds LM, Vijayaraghavan RK, Daniels S, O'Donnell CP, et al. Effect of non-thermal plasma technology on microbial inactivation and total phenolic content of a model liquid food system and black pepper grains. LWT. 2020 jan;118:108716.

[13] Kearney AD, Boyle MA, Babu SK, Fallon M, Segurado R, Codd M, et al.. Challenges in assessing contamination levels and novel decontamination technologies in the critical care setting. Cambridge University Press; 2020.

[14] Langmuir I. Oscillations in ionized gases. Proc Nat Acad Sci USA. 1928;14(8)(627).

[15] Fridman A. Plasma Chemistry. Cambridge University Press; 2008.

[16] Abe H, Yoneda M, Fujiwara N. Developments of plasma etching technology for fabricating semiconductor devices. Jpn J Appl Phys. 2008 mar;47(3 PART 1):1435–1455.

[17] Chu PK, Qin S, Chan C, Cheung NW, Larson LA. Plasma immersion ion implantation - A fledgling technique for semiconductor processing. Mater Sci Eng R Reports. 1996 nov;17(6-7):207–280.

[18] Conrad JR, Radtke JL, Dodd RA, Worzala FJ, Tran NC. Plasma source ion-implantation technique for surface modification of materials. J Appl Phys. 1987 dec;62(11):4591–4596.

[19] Halfmann H, Bibinov N, Wunderlich J, Awakowicz P. A double inductively coupled plasma for sterilization of medical devices. J Phys D Appl Phys. 2007 jul;40(14):4145–4154.

[20] Graves DB. Low temperature plasma biomedicine: A tutorial review. Phys Plasmas. 2014 aug;21(8):080901.

[21] Fridman AA, Kennedy LA. Plasma physics and engineering. CRC Press; 2011.

[22] Roth JR. Industrial Plasma Engineering: Volume 1: Principles. vol. 1. London: Taylor and Francis; 1995.

[23] Min JH, Lee J, Ayman MT, Kim HN, Park YJ, Yoon DH. Plasma etching properties of various transparent ceramics. Ceram Int. 2020 feb;46(3):2895–2900.

[24] Prakash C, Singh S, Sharma S, Garg H, Singh J, Kumar H, et al. Fabrication of aluminium carbon nano tube silicon carbide particles based hybrid nanocomposite by spark plasma sintering. In: Mater. Today Proc.. vol. 21. Elsevier Ltd; 2020. p. 1637–1642.

[25] Huang Y, Liao M, Wang Z, Guo X, Jiang C, Yang Q, et al. Ultrathin silicon oxide prepared by in-line plasma-assisted N2O oxidation (PANO) and the application for n-type polysilicon passivated contact. Sol Energy Mater Sol Cells. 2020 may;208:110389.

[26] Freeland B, McCann R, Foley G, Brabazon D. High-efficiency generation of nanomaterials via laser ablation synthesis in solution with in-situ diagnostics for closed-loop control. In: Kabashin AV, Dubowski JJ, Geohegan DB, editors. Synth. Photonics Nanoscale Mater. XVII. vol. 11269. SPIE; 2020. p. 22.

[27] Maier AR, Kirchen M, Grüner F. Brilliant light sources driven by laser-plasma accelerators. In: Synchrotron Light Sources Free. Lasers Accel. Physics, Instrum. Sci. Appl. Springer International Publishing; 2020. p. 245–270.

[28] Faure J, Glinec Y, Pukhov A, Klselev S, Gordienko S, Lefebvre E, et al. A laser-plasma accelerator producing monoenergetic electron beams. Nature. 2004 sep;431(7008):541–544.

[29] Sprangle P, Esarey E, Ting A. Nonlinear theory of intense laser-plasma interactions. Phys Rev Lett. 1990 apr;64(17):2011–2014.

[30] Gibbon P, Förster E. Short-pulse laser-plasma interactions. IOP Publishing; 1996.

[31] Lieberman MA, Lichtenberg AJ. PRINCIPLES OF PLASMA DISCHARGES AND MATERIALS PROCESSING Second Edition;.

[32] Kunhardt EE. Generation of large-volume, atmospheric-pressure, nonequilibrium plasmas. IEEE Trans Plasma Sci. 2000;28(1):189–200.

[33] Engel Av, Seeliger R, Steenbeck M. Uber die Glimmentladung bei hohen Drucken. Zeitschrift fur Phys. 1933 mar;85(3-4):144–160.

[34] Kanazawa S, Kogoma M, Moriwaki T, Okazaki S. Stable glow plasma at atmospheric pressure. J Phys D Appl Phys. 1988 may;21(5):838–840.

[35] Massines F, Mayoux C, Messaoudi R, Rabehi A. Experimental study of an atmospheric pressure glow discharge application to polymers surface treatment. 1992;p. 730–733.

[36] Roth JR, Laroussi M, Chaoyu Liu. Experimental Generation Of A Steady-state Glow Discharge At Atmospheric Pressure. In: IEEE Conf. Rec. - Abstr. 1992 IEEE Int. Conf. Plasma. IEEE; 1992. p. 170–171.

[37] Mildren RP, Carman RJ. Enhanced performance of a dielectric barrier discharge lamp using short - pulsed excitation. J Phys D Appl Phys. 2001;34:1–6.

[38] Packan D, Yu L, Laux CO, Kruger CH. Repetitively-pulsed DC glow discharge in atmospheric pressure air: modeling and experiments with a 12 kV, 10 Ns,

100 kHz pulse generator. In: IEEE Conf. Rec. - Abstr. PPPS-2001 Pulsed Power Plasma Sci. 2001. 28th IEEE Int. Conf. Plasma Sci. 13th IEEE Int. Pulsed Power Conf. (Cat. No.01CH37255). IEEE;. p. 259.

[39] Duten X, Packan D, Yu L, Laux CO, Kruger CH. DC and pulsed glow discharges in atmospheric pressure air and nitrogen. IEEE Trans Plasma Sci. 2002 feb;30(1):178–179.

[40] Laroussi M, Lu X, Kolobov V, Arslanbekov R. Power consideration in the pulsed dielectric barrier discharge at atmospheric pressure. J Appl Phys. 2004 sep;96(5):3028–3030.

[41] Laroussi M. Sterilization of contaminated matter with an atmospheric pressure plasma. IEEE Trans Plasma Sci. 1996 jun;24(3):1188–1191.

[42] Kelly-Wintenberg K, Montie TC, Brickman C, Roth JR, Carr AK, Sorge K, et al. Room temperature sterilization of surfaces and fabrics with a One Atmosphere Uniform Glow Discharge Plasma. J Ind Microbiol Biotechnol. 1998 jan;20(1):69–74.

[43] Laroussi M, Akan T. Arc-Free Atmospheric Pressure Cold Plasma Jets: A Review. Plasma Process Polym. 2007 nov;4(9):777–788. Available from: http://doi.wiley.com/10.1002/ppap.200700066.

[44] Wu S, Lu X, Liu D, Yang Y, Pan Y, Ostrikov K. Photo-ionization and residual electron effects in guided streamers. Phys Plasmas. 2014 oct;21(10):103508.

[45] Laroussi M, Lu X. Room-temperature atmospheric pressure plasma plume for biomedical applications. Appl Phys Lett. 2005 sep;87(11):113902.

[46] Jarrige J, Laroussi M, Karakas E. Formation and dynamics of plasma bullets in a non-thermal plasma jet: influence of the high-voltage parameters on the plume characteristics. Plasma Sources Sci Technol. 2010 dec;19(6):065005.

[47] Shashurin A, Shneider MN, Dogariu A, Miles RB, Keidar M. Temporal behavior of cold atmospheric plasma jet. Appl Phys Lett. 2009 jun;94(23):231504.

[48] Kim HC, Iza F, Yang SS, Radmilovi-Radjenovi M, Lee JK. Particle and fluid simulations of low-temperature plasma discharges: benchmarks and kinetic effects. J Phys D Appl Phys J Phys D Appl Phys. 2005;38(38):283–301.

[49] Douat C, Bauville G, Fleury M, Laroussi M, Puech V. Dynamics of colliding microplasma jets. Plasma Sources Sci Technol. 2012 jun;21(3):034010.

[50] Xiong Q, Lu XP, Ostrikov K, Xian Y, Zou C, Xiong Z, et al. Pulsed dc- and sine-wave-excited cold atmospheric plasma plumes: A comparative analysis. Phys Plasmas. 2010 apr;17(4):043506.

[51] Kramer A, Lademann J, Bender C, Sckell A, Hartmann B, Münch S, et al. Suitability of tissue tolerable plasmas (TTP) for the management of chronic wounds. Clin Plasma Med. 2013 jun;1(1):11–18.

[52] Laroussi M, Lu X, Malott CM. A non-equilibrium diffuse discharge in atmospheric pressure air*. Plasma Sources Sci Technol. 2003 feb;12(1):53–56.

[53] Leipold F, Stark RH, El-Habachi A, Schoenbach KH. Electron density measurements in an atmospheric pressure air plasma by means of infrared heterodyne interferometry. J Phys D Appl Phys. 2000 sep;33(18):2268–2273.

[54] Kalghatgi S, Kelly CM, Cerchar E, Torabi B, Alekseev O, Fridman A, et al. Effects of Non-Thermal Plasma on Mammalian Cells. PLoS One. 2011 jan;6(1):e16270.

[55] Kim MC, Yang SH, Boo JH, Han JG. Surface treatment of metals using an atmospheric pressure plasma jet and their surface characteristics. Surf Coatings Technol. 2003;174(175):839–844.

[56] Kojima S, Funahashi T, Sakamoto T, Miyamoto S, Soejima H, Hokamaki J, et al. The variation of plasma concentrations of a novel, adipocyte derived protein, adiponectin, in patients with acute myocardial infarction. Heart. 2003 jun;89(6):667.

[57] Xian Y, Lu X, Wu S, Chu PK, Pan Y. Are all atmospheric pressure cold plasma jets electrically driven? Appl Phys Lett. 2012 mar;100(12):123702.

[58] Wu S, Lu X, Xiong Z, Pan Y. A Touchable Pulsed Air Plasma Plume Driven by DC Power Supply. IEEE Trans PLASMA Sci. 2010;38(12).

[59] Leipold F, Kusano Y, Hansen F, Jacobsen T. Decontamination of a rotating cutting tool during operation by means of atmospheric pressure plasmas. Food Control. 2010 aug;21(8):1194–1198.

[60] Braithwaite NSJ. Introduction to gas discharges. Plasma Sources Sci Technol. 2000;9(00):517–527.

[61] Paschen F. Ueber die zum funkenubergang in luft, wasserstoff und kohlensaure bei verschiedenen drucken erforderliche potentialdifferenz. Ann Phys. 1889;273(5):69.

[62] Fridman AA, Kennedy LA. Plasma physics and engineering. Taylor and Francis; 2004.

[63] Loeb LB. Significance of Formative Time Lags in Gaseous Breakdown. Phys Rev. 1959 jan;113(1):7–12.

[64] Meek JM. A Theory of Spark Discharge. Phys Rev. 1940 apr;57(8):722–728.

[65] Palmer AJ. A physical model on the initiation of atmospheric pressure glow discharges. Appl Phys Lett. 1974 aug;25(3):138–140.

[66] Schutze A, Jeong JYY, Babayan SEE, Selwyn GSGS, Hicks RFRF, Park J, et al. The atmospheric-pressure plasma jet: a review and comparison to other plasma sources. Plasma Sci IEEE Trans. 1998;26(6):1685–1694.

[67] Lieberman MA, Lichtenberg AJ. Principles of plasma discharges and materials processing. Wiley-Interscience; 2005.

[68] Kogelschatz U. Dielectric-barrier discharges: Their History, Discharge Physics, and Industrial Applications; 2003.

[69] Tendero C, Tixier C, Tristant P, Desmaison J, Leprince P. Atmospheric pressure plasmas: A review. Spectrochim Acta Part B At Spectrosc. 2006 jan;61(1):2–30. Available from: http://apps.webofknowledge.com/full{_}record.do?product=UA{&}search{_}mode=GeneralSearch{&}qid=1{&}SID=W2YwQXYK1Bnl8c4Mibo{&}page=2{&}doc=17.

[70] Roth JR, Rahel J, Dai X, Sherman DM. The physics and phenomenology of One Atmosphere Uniform Glow Discharge Plasma (OAUGDP™) reactors for surface treatment applications. J Phys D Appl Phys. 2005 feb;38(4):555–567.

[71] Seidelmann L, Bradley J, Ratova M, Hewitt J, Moffat J, Kelly P. Reel-to-Reel Atmospheric Pressure Dielectric Barrier Discharge (DBD) Plasma Treatment of Polypropylene Films. Appl Sci. 2017 mar;7(4):337. Available from: http://www.mdpi.com/2076-3417/7/4/337.

[72] Shao T, Liu F, Hai B, Ma Y, Wang R, Ren C. Surface modification of epoxy using an atmospheric pressure dielectric barrier discharge to accelerate surface charge dissipation. IEEE Trans Dielectr Electr Insul. 2017;24(3):1557–1565.

[73] Ren Y, Xu L, Wang C, Wang X, Ding Z, Chen Y. Effect of dielectric barrier discharge treatment on surface nanostructure and wettability of polylactic acid (PLA) nonwoven fabrics. Appl Surf Sci. 2017 dec;426:612–621.

[74] Galmiz O, Pavliňák D, Zemánek M, Brablec A, Černák M. Hydrophilization of outer and inner surfaces of Poly(vinyl chloride) tubes using surface dielectric

barrier discharges generated in ambient air plasma. Plasma Process Polym. 2017 sep;14(9):1600220.

[75] Iervolino G, Vaiano V, Palma V. Enhanced removal of water pollutants by dielectric barrier discharge non-thermal plasma reactor. Sep Purif Technol. 2019 may;215:155–162.

[76] Mustafa MF, Fu X, Liu Y, Abbas Y, Wang H, Lu W. Volatile organic compounds (VOCs) removal in non-thermal plasma double dielectric barrier discharge reactor. J Hazard Mater. 2018 apr;347:317–324.

[77] Abou Saoud W, Assadi AA, Guiza M, Bouzaza A, Aboussaoud W, Ouederni A, et al. Study of synergetic effect, catalytic poisoning and regeneration using dielectric barrier discharge and photocatalysis in a continuous reactor: Abatement of pollutants in air mixture system. Appl Catal B Environ. 2017 sep;213:53–61.

[78] Köhler J. Dielectric barrier discharge pumped N2 laser. Appl Opt. 1994;33(18).

[79] Azarov AV, Mit'ko SV, Ochkin VN. A Xe laser pumped by fast electrons generated in a barrier discharge. Quantum Electron. 2002;32(8):675–680.

[80] Azarov A, Mitko S, Ochkin V. Open barrier discharge as Xe laser pumping source. In: Int. Conf. Lasers. Moscow; 2003. .

[81] Eliasson B, Kogelschatz U. UV excimer radiation from dielectric-barrier discharges. Appl Phys B Photophysics Laser Chem. 1988 aug;46(4):299–303.

[82] Subedi DP, Joshi UM, Wong CS. Dielectric barrier discharge (DBD) plasmas and their applications. In: Plasma Sci. Technol. Emerg. Econ. An AAAPT Exp. Springer Singapore; 2017. p. 693–737.

[83] Khan TM, Khan SUD, Khan SUD, Ahmad A, Abbasi SA. A new strategy of using dielectric barrier discharge plasma in tubular geometry for surface coating and extension to biomedical application. Rev Sci Instrum. 2020 jul;91(7):073902.

[84] Shahbazi Rad Z, Abbasi Davani F. Non-thermal atmospheric pressure dielectric barrier discharge plasma source construction and investigation on the effect of grid on wound healing application. Clin Plasma Med. 2016 dec;4(2):56–64.

[85] Lee KH, Kim S, Jo H, Son BK, Shin MS, Cho G. Plasma skincare device based on floating electrode dielectric barrier discharge. Plasma Sci Technol. 2019 oct;21(12):125403.

[86] Dzimitrowicz A, Bielawska-Pohl A, Jamroz P, Dora J, Krawczenko A, Busco G, et al. Activation of the Normal Human Skin Cells by a Portable Dielectric Barrier Discharge-Based Reaction-Discharge System of a Defined Gas Temperature. Plasma Chem Plasma Process. 2020 jan;40(1):79–97. Available from: https://doi.org/10.1007/s11090-019-10039-0.

[87] He T, Liu D, Wang B, Wang W, Liu Z, Guo L, et al. Surface patterns of reactive species on model tissue treated by a surface air discharge. J Phys D Appl Phys. 2019 mar;51(20):20LT01.

[88] Kim J, Ghimire B, Lim S, Choi EH, Park HK, Kaushik NK. Coagulation, deformability, and aggregation of RBCs and platelets following exposure to dielectric barrier discharge plasma with the use of different feeding gases. J Phys D Appl Phys. 2019 feb;52(15):155202.

[89] Ding C, Huang P, Feng L, Jin T, Zhou Y, He Y, et al. Immediate intervention effect of dielectric barrier discharge on acute inflammation in rabbit's ear wound. AIP Adv. 2020 feb;10(2):025008.

[90] Xu X. Dielectric barrier discharge - Properties and applications. Thin Solid Films. 2001 jun;390(1-2):237–242.

[91] Yue Y, Kondeti VSSK, Bruggeman PJ. Absolute atomic hydrogen density measurements in an atmospheric pressure plasma jet: Generation, transport and recombination from the active discharge region to the effluent. Plasma Sources Sci Technol. 2020 mar;29(4):04LT01.

[92] Norberg SA, Johnsen E, Kushner MJ. Formation of reactive oxygen and nitrogen species by repetitive negatively pulsed helium atmospheric pressure plasma jets propagating into humid air. Plasma Sources Sci Technol. 2015 may;24(3):035026.

[93] Jiang C, Carter C. Absolute atomic oxygen density measurements for nanosecond-pulsed atmospheric-pressure plasma jets using two-photon absorption laser-induced fluorescence spectroscopy. Plasma Sources Sci Technol. 2014 dec;23(6):065006.

[94] Li X, Jia P, Yuan N, Fang T, Wang L. One atmospheric pressure plasma jet with two modes at a frequency of several tens kHz. Phys Plasmas. 2011 apr;18(4):043505.

[95] Gidon D, Curtis B, Paulson JA, Graves DB, Mesbah A. Model-Based Feedback Control of a kHz-Excited Atmospheric Pressure Plasma Jet. IEEE Trans Radiat Plasma Med Sci. 2017 oct;2(2):129–137.

[96] Hofmans M, Viegas P, Rooij OV, Klarenaar B, Guaitella O, Bourdon A, et al. Characterization of a kHz atmospheric pressure plasma jet: Comparison of discharge propagation parameters in experiments and simulations without target. Plasma Sources Sci Technol. 2020 mar;29(3):034003.

[97] Popović D, Bišćan M, Milošević S. Laser induced breakdown in pulsed helium atmospheric pressure plasma jet. Plasma Sources Sci Technol. 2019 may;28(5):55009.

[98] Ning W, Dai D, Zhang Y, Han Y, Li L. Effects of trace of nitrogen on the helium atmospheric pressure plasma jet interacting with a dielectric substrate. J Phys D Appl Phys. 2018 mar;51(12):125204.

[99] Jõgi I, Talviste R, Raud S, Raud J, Plank T, Moravský L, et al. Comparison of two cold atmospheric pressure plasma jet configurations in argon. Contrib to Plasma Phys. 2020 mar;60(3):e201900127.

[100] Conway J, Gogna G, Daniels S, Conway J, Gogna G, Daniels S. Two-photon absorption laser induced fluorescence measurement of atomic oxygen density in an air atmospheric pressure plasma jet. APS. 2016;p. MW6.066.

[101] Xaubet M, Baudler JS, Gerling T, Giuliani L, Minotti F, Grondona D, et al. Design optimization of an air atmospheric pressure plasma-jet device intended for medical use. Plasma Process Polym. 2018 aug;15(8):1700211.

[102] Roy NC, Talukder MR, Chowdhury AN. OH and O radicals production in atmospheric pressure air/Ar/H2O gliding arc discharge plasma jet. Plasma Sci Technol. 2017 dec;19(12):125402.

[103] Winter J, Brandenburg R, Weltmann KD. Atmospheric pressure plasma jets: An overview of devices and new directions. Plasma Sources Sci Technol. 2015 oct;24(6):064001. Available from: https://iopscience.iop.org/article/10.1088/0963-0252/24/6/064001https://iopscience.iop.org/article/10.1088/0963-0252/24/6/064001/meta.

[104] Walsh JL, Kong MG. Contrasting characteristics of linear-field and cross-field atmospheric plasma jets. Appl Phys Lett. 2008 sep;93(11):111501.

[105] Kolb JF, Mohamed AAH, Price RO, Swanson RJ, Bowman A, Chiavarini RL, et al. Cold atmospheric pressure air plasma jet for medical applications. Appl Phys Lett. 2008 jun;92(24):241501.

[106] Kim SJ, Chung TH. Cold atmospheric plasma jet-generated RONS and their selective effects on normal and carcinoma cells. Sci Rep. 2016 jan;6:20332.

[107] Hirst AM, Frame FM, Arya M, Maitland NJ, O'Connell D. Low temperature plasmas as emerging cancer therapeutics: the state of play and thoughts for the future. Tumor Biol. 2016 jun;37(6):7021–7031.

[108] Xu D, Luo X, Xu Y, Cui Q, Yang Y, Liu D, et al. The effects of cold atmospheric plasma on cell adhesion, differentiation, migration, apoptosis and drug sensitivity of multiple myeloma; 2016.

[109] Scholtz V, Pazlarova J, Souskova H, Khun J, Julak J. Nonthermal plasma — A tool for decontamination and disinfection. Biotechnol Adv. 2015;33(6):1108–1119.

[110] Edelblute CM, Malik MA, Heller LC. Antibacterial efficacy of a novel plasma reactor without an applied gas flow against methicillin resistant Staphylococcus aureus on diverse surfaces. Bioelectrochemistry. 2016;112:106–111.

[111] Kalghatgi S, Kelly CM, Cerchar E, Torabi B, Alekseev O, Fridman A, et al. Effects of Non-Thermal Plasma on Mammalian Cells. PLoS One. 2011 jan;6(1):e16270.

[112] Xinpei Lu, Yinguang Cao, Ping Yang, Qing Xiong, Zilan Xiong, Yubin Xian, et al. An RC Plasma Device for Sterilization of Root Canal of Teeth. IEEE Trans Plasma Sci. 2009 may;37(5):668–673.

[113] Teschke M, Kedzierski J, Finantu-Dinu EG, Korzec D, Engemann J. High-speed photographs of a dielectric barrier atmospheric pressure plasma jet. IEEE Trans Plasma Sci. 2005 apr;33(2):310–311.

[114] Lu X, Laroussi M. Dynamics of an atmospheric pressure plasma plume generated by submicrosecond voltage pulses. J Appl Phys. 2006 sep;100(6):063302.

[115] Mericam-Bourdet N, Laroussi M, Begum A, Karakas E. Experimental investigations of plasma bullets. J Phys D Appl Phys. 2009 feb;42(5):055207.

[116] Xiong Q, Lu X, Xian Y, Liu J, Zou C, Xiong Z, et al. Experimental investigations on the propagation of the plasma jet in the open air. J Appl Phys. 2010 apr;107(7):073302.

[117] Xiong Q, Lu X, Ostrikov K, Xiong Z, Xian Y, Zhou F, et al. Length control of He atmospheric plasma jet plumes: Effects of discharge parameters and ambient air. Phys Plasmas. 2009;16(4).

[118] Singh Gogna G, Kelly S, Daniels S. Reactive species and thermal characteristics of a constricted arc plasma air jet . In: 32nd ICPIG. Iasi, Romania; 2015. .

[119] Lu X, Laroussi M, Puech V. On atmospheric-pressure non-equilibrium plasma jets and plasma bullets. Plasma Sources Sci Technol. 2012 jun;21(3):034005.

[120] Xiao D, Cheng C, Shen J, Lan Y, Xie H, Shu X, et al. Characteristics of atmospheric-pressure non-thermal N2 and N2/O2 gas mixture plasma jet. J Appl Phys. 2014;115:33303.

[121] Miao C, Shi D, Ma C, Ren C, Lu W, Zhang Q, et al. Mode transition and related discharge phenomena of a tube plasma source operating in low-pressure pure nitrogen atmosphere. IEEE Trans Plasma Sci. 2015 feb;43(2):544–551.

[122] Czerwiec T, Greer F, Graves DB. Nitrogen dissociation in a low pressure cylindrical ICP discharge studied by actinometry and mass spectrometry. J Phys D Appl Phys. 2005 dec;38(24):4278–4289.

[123] Czerwiec T, Graves DB. Mode transitions in low pressure rare gas cylindrical ICP discharge studied by optical emission spectroscopy. J Phys D Appl Phys. 2004 oct;37(20):2827–2840.

[124] Dai D, Hou HX, Hao YP. Influence of gap width on discharge asymmetry in atmospheric pressure glow dielectric barrier discharges. Appl Phys Lett. 2011 mar;98(13):131503.

[125] Ning W, Dai D, Zhang Y, Hao Y, Li L. Transition from symmetric discharge to asymmetric discharge in a short gap helium dielectric barrier discharge. Phys Plasmas. 2017;24:73509.

[126] Luo H, Liang Z, Lv B, Wang X, Guan Z, Wang L. Observation of the transition from a Townsend discharge to a glow discharge in helium at atmospheric pressure. Appl Phys Lett. 2007;91:221504.

[127] Mangolini L, Anderson C, Heberlein J, Kortshagen U. Effects of current limitation through the dielectric in atmospheric pressure glows in helium. J Phys D Appl Phys. 2004 apr;37(7):1021–1030.

[128] Simek M, Debenedictis S, Dilecce G, Bruggeman P, Brandenburg R, Nijdam S, et al. Optical diagnostics of streamer discharges in atmospheric gases. J Phys D Appl Phys;47.

[129] Bayram SB, Freamat MV. Vibrational spectra of N 2 : An advanced undergraduate laboratory in atomic and molecular spectroscopy. Am J Phys. 2012 aug;80(8):664–669.

[130] Bayram SB, Arndt PT, Freamat MV. Rotational spectra of N2+: An advanced undergraduate laboratory in atomic and molecular spectroscopy. Am J Phys. 2015 oct;83(10):867–872.

[131] Macko P, Veis P. Time resolved O2(b1Sigma g+) rotational temperature measurements in a low-pressure oxygen pulsed discharge. Simple and quick method for temperature determination. J Phys D Appl Phys. 1999 feb;32(3):246–250.

[132] Schmiedt L, Kaňka A, Hrachová V. Study of rotational temperature of oxygen molecules in H and T forms of DC glow discharge sustained in pure oxygen. Vacuum. 2011 jun;85(12):1093–1095.

[133] Rezaei F, Abbasi-Firouzjah M, Shokri B. Investigation of antibacterial and wettability behaviours of plasma-modified PMMA films for application in ophthalmology. J Phys D Appl Phys. 2014 feb;47(8):085401.

[134] Rezaei F, Abbasi-Firouzjah M, Shokri B. Investigation of antibacterial and wettability behaviours of plasma-modified PMMA films for application in ophthalmology. J Phys D Appl Phys. 2014 feb;47(8):085401.

[135] Krstulović N, Labazan I, Milošević S, Cvelbar U, Vesel A, Mozetič M. Optical emission spectroscopy characterization of oxygen plasma during treatment of a PET foil. J Phys D Appl Phys. 2006 sep;39(17):3799–3804.

[136] Striganov AR, Sventitskii NS. Tables of Spectral Lines of Neutral and Ionized Atoms. Boston, MA: Springer US; 1968.

[137] Richards WGWG, Scott PRPR. Structure and spectra of atoms. Wiley; 1976.

[138] Lide DR. CRC Handbook of Chemistry and Physics. Boca Raton, FL: CRC Press; 2005.

[139] Cacciatore M, Capitelli M, Gorse C. Non-equilibrium dissociation and ionization of nitrogen in electrical discharges: The role of electronic collisions from vibrationally excited molecules. Chem Phys. 1982 apr;66(1-2):141–151.

[140] M Capitelli, C M Ferreira, B F Gordiets AIO. Plasma Kinetics in Atmospheric Gases;.

[141] Guerra V, Sá PA, Loureiro J. Kinetic modeling of low-pressure nitrogen discharges and post-discharges. Eur Phys J Appl Phys. 2004 nov;28(2):125–152.

[142] Henderson WR, Fite WL, Brackmann RT. Dissociative attachment of electrons to hot oxygen. Phys Rev. 1969 jul;183(1):157–166.

[143] O'Malley TF. Calculation of dissociative attachment in hot O2. Phys Rev. 1967 mar;155(1):59–63.

[144] Ono R. Optical diagnostics of reactive species in atmospheric-pressure nonthermal plasma. J Phys D Appl Phys To. 2016;49(083001).

[145] Hartmann G, Gallimberti I. The influence of metastable molecules on the streamer progression. J Phys D Appl Phys. 1975;8(6):670–680.

[146] Baeva M, Luo X, Pfelzer B, Uhlenbusch J. Theoretical investigation of pulsed microwave discharge in nitrogen. Plasma Sources Sci Technol. 1999 aug;8(3):404–411.

[147] Baeva M, Gier H, Pott A, Uhlenbusch J, Höschele J, Steinwandel J. Pulsed microwave discharge at atmospheric pressure for NOx decomposition. Plasma Sources Sci Technol. 2002 feb;11(1):1–9.

[148] Ono R, Oda T. Measurement of gas temperature and OH density in the afterglow of pulsed positive corona discharge. J Phys D Appl Phys. 2008 feb;41(3):035204.

[149] Nakagawa Y, Ono R, Oda T. Density and temperature measurement of OH radicals in atmospheric-pressure pulsed corona discharge in humid air. J Appl Phys. 2011 oct;110(7):073304.

[150] Eichwald O, Yousfi M, Hennad A, Benabdessadok MD. Coupling of chemical kinetics, gas dynamics, and charged particle kinetics models for the analysis of NO reduction from flue gases. J Appl Phys. 1997 nov;82(10):4781–4794.

[151] Komuro A, Ono R. Two-dimensional simulation of fast gas heating in an atmospheric pressure streamer discharge and humidity effects. J Phys D Appl Phys. 2014 apr;47(15):155202.

[152] Plasma Sources Science and Technology Recent citations. 2020;.

[153] Teramoto Y, Ono R. Measurement of vibrationally excited N2(v) in an atmospheric-pressure air pulsed corona discharge using coherent anti-Stokes Raman scattering. J Appl Phys. 2014 aug;116(7):073302.

[154] Simek M, DeBenedictis S, Dilecce G, Babický V, Clupek M, Sunka P. Time and space resolved analysis of N2(C3Pi u) vibrational distributions in pulsed positive corona discharge. J Phys D Appl Phys. 2002 aug;35(16):1981–1990.

[155] Lo A, Cessou A, Boubert P, Vervisch P. Space and time analysis of the nanosecond scale discharges in atmospheric pressure air: I. Gas temperature and vibrational distribution function of N 2 and O2. J Phys D Appl Phys. 2014 mar;47(11):115201.

[156] Lo A, Cléon G, Vervisch P, Cessou A. Spontaneous Raman scattering: A useful tool for investigating the afterglow of nanosecond scale discharges in air. Appl Phys B Lasers Opt. 2012 apr;107(1):229–242.

[157] Baeva M, Dogan A, Ehlbeck J, Pott A, Uhlenbusch J. Cars diagnostic and modeling of a dielectric barrier discharge. Plasma Chem Plasma Process. 1999;19(4):445–466.

[158] Baeva M, Gier H, Pott A, Uhlenbusch J, Höschele J, Steinwandel J. Pulsed microwave discharge at atmospheric pressure for NOx decomposition. Plasma Sources Sci Technol. 2002 feb;11(1):1–9.

[159] Ono R, Teramoto Y, Oda T. Effect of humidity on gas temperature in the afterglow of pulsed positive corona discharge. Plasma Sources Sci Technol. 2010 nov;19(1):015009.

[160] Finzi J, Hovis FE, Panfilov VN, Hess P, Bradley Moore C. Vibrational relaxation of water vapor. J Chem Phys. 1977 aug;67(9):4053–4061.

[161] Komuro A, Takahashi K, Ando A. Vibration-to-translation energy transfer in atmospheric-pressure streamer discharge in dry and humid air. Plasma Sources Sci Technol. 2015 sep;24(5):055020.

[162] Eliasson B, Kogelschatz U. Electron impact dissociation in oxygen. J Phys B At Mol Phys. 1986;19(8):1241–1247.

[163] Eliasson B, Hirth M, Kogelschatz U. Ozone synthesis from oxygen in dielectric barrier discharges. J Phys D Appl Phys. 1987;20(11):1421–1437.

[164] Popov NA. Fast gas heating in a nitrogen-oxygen discharge plasma: I. Kinetic mechanism. J Phys D Appl Phys. 2011 jul;44(28):285201.

[165] Ono R, Takezawa K, Oda T. Two-photon absorption laser-induced fluorescence of atomic oxygen in the afterglow of pulsed positive corona discharge. J Appl Phys. 2009 aug;106(4):043302.

[166] Komuro A, Ono R, Oda T. Numerical simulation for production of O and N radicals in an atmospheric-pressure streamer discharge. J Phys D Appl Phys. 2012 jul;45(26):265201.

[167] Gentile AC, Kushner MJ. Reaction chemistry and optimization of plasma remediation of N xOy from gas streams. J Appl Phys. 1995 aug;78(3):2074–2085.

[168] Lowke JJ, Morrow R. Theoretical Analysis of Removal of Oxides of Sulphur and Nitrogen in Pulsed Operation of Electrostatic Precipitators. IEEE Trans Plasma Sci. 1995;23(4):661–671.

[169] Komuro A, Ono R, Oda T. Behaviour of OH radicals in an atmospheric pressure streamer discharge studied by two dimensional numerical simulation. J Phys D Appl Phys. 2013;46(175206).

[170] Ono R, Oda T. Dynamics of ozone and OH radicals generated by pulsed corona discharge in humid-air flow reactor measured by laser spectroscopy. J Appl Phys. 2003 may;93(10 1):5876–5882.

[171] Fresnet F, Baravian G, Magne L, Pasquiers S, Postel C, Puech V, et al. Influence of water on NO removal by pulsed discharge in N2/H2O/NO mixtures. Plasma Sources Sci Technol. 2002 apr;11(2):152.

[172] Frese M, Gloy G, Oberprieler RG, Gore DB. Imaging of jurassic fossils from the talbragar fish bed using fluorescence, photoluminescence, and elemental and mineralogical mapping. PLoS One. 2017 jun;12(6).

[173] Moses TM, Reinitz IM, Johnson ML, King JM, Shigley JE. A Contribution to Understanding the Effect of Blue Fluorescence on the Appearance of Diamonds. Gemol Gems. 1997;XXXIII(Winter 1997).

[174] Shenderova OA, Shames AI, Nunn NA, Torelli MD, Vlasov I, Zaitsev A. Review Article: Synthesis, properties, and applications of fluorescent diamond particles. J Vac Sci Technol B. 2019 may;37(3):030802.

[175] Ibañez GA, Escandar GM. Fluorescence and phosphorescence chemical sensors applied to water samples. In: Smart Sensors, Meas. Instrum.. vol. 4. Springer International Publishing; 2013. p. 45–64.

[176] Zhang M, Feng G, Song Z, Zhou YP, Chao HY, Yuan D, et al. Two-dimensional metal-organic framework with wide channels and responsive turn-on fluorescence for the chemical sensing of volatile organic compounds. J Am Chem Soc. 2014 may;136(20):7241–7244.

[177] Wang M, Zhang D, Zhang G, Tang Y, Wang S, Zhu D. Fluorescence turn-on detection of DNA and label-free fluorescence nuclease assay based on the aggregation-induced emission of silole. Anal Chem. 2008 aug;80(16):6443–6448.

[178] Umezawa K, Nakamura Y, Makino H, Citterio D, Suzuki K. Bright, color-tunable fluorescent dyes in the visible-near-infrared region. J Am Chem Soc. 2008 feb;130(5):1550–1551.

[179] Koide Y, Urano Y, Hanaoka K, Piao W, Kusakabe M, Saito N, et al. Development of NIR fluorescent dyes based on Si-rhodamine for in vivo imaging. J Am Chem Soc. 2012 mar;134(11):5029–5031.

[180] Berezin MY, Achilefu S. Fluorescence lifetime measurements and biological imaging. Chem Rev. 2010 may;110(5):2641–2684.

[181] Tango WJ, Link JK, Zake RN. Spectroscopy of K2using laser-induced fluorescence. J Chem Phys. 1968 nov;49(10):4264–4268.

[182] Zare RN. My Life with LIF: A Personal Account of Developing Laser-Induced Fluorescence. Annu Rev Anal Chem. 2012 jul;5(1):1–14.

[183] Tamura M, Berg PA, Harrington JE, Luque J, Jeffries JB, Smith GP, et al. Collisional Quenching of CH(A), OH(A), and NO(A) in Low Pressure Hydrocarbon Flames. Combust Flame. 1998 aug;114(3-4):502–514.

[184] Mouton T, Mercier X, Wartel M, Lamoureux N, Desgroux P. Laser-induced incandescence technique to identify soot nucleation and very small particles in low-pressure methane flames. Appl Phys B Lasers Opt. 2013 sep;112(3):369–379.

[185] Wu L, Lane J, Cernansky NP, Miller DL, Fridman AA, Starikovskiy AY. Plasma-assisted ignition below self-ignition threshold in methane, ethane, propane and butane-air mixtures. Proc Combust Inst. 2011 jan;33(2):3219–3224.

[186] Bejaoui S, Batut S, Therssen E, Lamoureux N, Desgroux P, Liu F. Measurements and modeling of laser-induced incandescence of soot at different heights in a flat premixed flame. Appl Phys B Lasers Opt. 2015 jan;118(3):449–469.

[187] Uddi M, Jiang N, Adamovich IV, Lempert WR. Nitric oxide density measurements in air and air/fuel nanosecond pulse discharges by laser induced fluorescence. J Phys D Appl Phys. 2009 apr;42(7):075205.

[188] Van Gessel AFH, Hrycak B, Jasiński M, Mizeraczyk J, Van Der Mullen JJAM, Bruggeman PJ. Temperature and NO density measurements by LIF and OES on an atmospheric pressure plasma jet. J Phys D Appl Phys. 2013 mar;46(9):095201.

[189] Van Gessel AFH, Alards KMJ, Bruggeman PJ. NO production in an RF plasma jet at atmospheric pressure. J Phys D Appl Phys. 2013 jul;46(26):265202.

[190] Dilecce G, Ambrico PF, De Benedictis S. CH spectroscopic observables in He-CH4 and N2-CH 4 atmospheric pressure dielectric barrier discharges. J Phys D Appl Phys. 2010 mar;43(12):124004.

[191] Dilecce G, Ambrico PF, Scarduelli G, Tosi P, De Benedictis S. CN(B2 sigma+) formation and emission in a N2-CH4 atmospheric pressure dielectric barrier discharge. Plasma Sources Sci Technol. 2009 feb;18(1):015010.

[192] Dilecce G, Ambrico PF, De Benedictis S. N2(A3 Sigma u) density measurement in a dielectric barrier discharge in N2 and N2 with small O2 admixtures. Plasma Sources Sci Technol. 2007 aug;16(3):511–522.

[193] Schmidt JB, Jiang N, Ganguly BN. Nitric oxide PLIF measurement in a point-to-plane pulsed discharge in vitiated air of a propane/air flame. Plasma Sources Sci Technol. 2014 aug;23(6):065005.

[194] Yonemori S, Ono R. Flux of OH and O radicals onto a surface by an atmospheric-pressure helium plasma jet measured by laser-induced fluorescence. J Phys D Appl Phys. 2014 mar;47(12):125401.

[195] Yue YF, Mohades S, Laroussi M, Lu X. Measurements of Plasma-Generated Hydroxyl and Hydrogen Peroxide Concentrations for Plasma Medicine Applications. IEEE Trans Plasma Sci. 2016 nov;44(11):2754–2758.

[196] Pei X, Wu S, Xian Y, Lu X, Pan Y. On OH density of an atmospheric pressure plasma jet by laser-induced fluorescence. IEEE Trans Plasma Sci. 2014 may;42(5):1206–1210.

[197] Ono R, Oda T. Measurement of gas temperature and OH density in the afterglow of pulsed positive corona discharge. J Phys D Appl Phys. 2008 feb;41(3):035204.

[198] Dilecce G, Ambrico PF, Simek M, De Benedictis S. LIF diagnostics of hydroxyl radical in atmospheric pressure He-H 2O dielectric barrier discharges. Chem Phys. 2012 apr;398(1):142–147.

[199] Bukshtab M. Laser Spectroscopy. vol. 209 of Advanced Texts in Physics. Berlin, Heidelberg: Springer Berlin Heidelberg; 2019.

[200] Greenberg KE, Hebner GA. Electric-field measurements in 13.56 MHz helium discharges. Appl Phys Lett. 1993 dec;63(24):3282–3284.

[201] Settersten TB, Patterson BD, Humphries WH. Radiative lifetimes of NO A 2 sigma + (v =0,1,2) and the electronic transition moment of the A 2 sigma +-X Pi 2 system. J Chem Phys. 2009 sep;131(10):104309.

[202] Dorai R, Kushner MJ. A model for plasma modification of polypropylene using atmospheric pressure discharges. J Phys D Appl Phys. 2003 mar;36(6):666–685.

[203] Baulch DL, Pilling MJ, Cobos CJ, Cox RA, Frank P, Hayman G, et al. Evaluated Kinetic Data for Combustion Modeling. Supplement I. J Phys Chem Ref Data. 1994 nov;23(6):847–848.

[204] Thomas JM, Kaufman F. An upper limit on the formation of no(x2hr) in the reactions N2(A3i:) + O(3P) and N2(A) + O2(X3Lg) at 298 K. J Phys Chem. 1996;100(21):8901–8906.

[205] Klochko AV, Lemainque J, Popov NA, Booth JP, Starikovskaya SM. Study of fast gas heating in a capillary nanosecond discharge in air. TALIF O atoms measurements and kinetic modeling. In: 51st AIAA Aerosp. Sci. Meet. Incl. New Horizons Forum Aerosp. Expo. 2013; 2013. .

[206] De Benedictis S, Dilecce G. Rate constants for deactivation of N2(A) v=2-7 by O, O2, and NO. J Chem Phys. 1997 oct;107(16):6219–6229.

[207] Burnette DD, Shkurenkov I, Adamovich IV, Lempert WR. An examination of nitric oxide kinetics in a plasma afterglow with significant vibrational loading. In: 52nd Aerosp. Sci. Meet. American Institute of Aeronautics and Astronautics Inc.; 2014. .

[208] Black G, Sharpless RL, Slanger TG. Measurements of vibrationally excited molecules by Raman scattering. i the yield of vibrationally excited nitrogen in the reaction N+NO→N 2+O. J Chem Phys. 1973 jun;58(11):4792–4797.

[209] Popov NA. Pulsed nanosecond discharge in air at high specific deposited energy: Fast gas heating and active particle production. Plasma Sources Sci Technol. 2016 may;25(4).

[210] Lo A, Cessou A, Boubert P, Vervisch P. Space and time analysis of the nanosecond scale discharges in atmospheric pressure air: I. Gas temperature and vibrational distribution function of N 2 and O2. J Phys D Appl Phys. 2014 mar;47(11):115201.

[211] Lo A, Cessou A, Vervisch P. Space and time analysis of the nanosecond scale discharges in atmospheric pressure air: II. Energy transfers during the post-discharge. J Phys D Appl Phys. 2014 mar;47(11):115202.

[212] Kossyi IA, Kostinsky AY, Matveyev AA, Silakov VP. Kinetic scheme of the non-equilibrium discharge in nitrogen-oxygen mixtures. Plasma Sources Sci Technol. 1992;1(3):207–220.

[213] Göppert-Mayer M. Über Elementarakte mit zwei Quantensprüngen. Ann Phys. 1931 jan;401(3):273–294.

[214] Franken PA, Hill AE, Peters CW, Weinreich G. Generation of optical harmonics. Phys Rev Lett. 1961;7(4):118–119.

[215] Kaiser W, Garrett CGB. Two-photon excitation in CaF2: Eu2+. Phys Rev Lett. 1961 sep;7(6):229–231.

[216] Kang N, Gaboriau F, Oh SG, Ricard A. Modeling and experimental study of molecular nitrogen dissociation in an Ar-N2 ICP discharge. Plasma Sources Sci Technol. 2011 aug;20(4):45015–45029.

[217] Es-sebbar E, C-Gazeau M, Benilan Y, Jolly A, Pintassilgo CD. Absolute ground-state nitrogen atom density in a N2/CH 4 late afterglow: TALIF experiments and modelling studies. J Phys D Appl Phys. 2010 aug;43(33):7.

[218] Damen MA, Hage DACM, Van De Steeg AW, Martini LM, Engeln R. Absolute CO number densities measured using TALIF in a non-thermal plasma environment. Plasma Sources Sci Technol. 2019 nov;28(11):115006.

[219] Xiong Q, Liu H, Britun N, Nikiforov AY, Li L, Chen Q, et al. Time-Selective TALIF Spectroscopy of Atomic Oxygen Applied to an Atmospheric Pressure Argon Plasma Jet. IEEE Trans Plasma Sci. 2016 nov;44(11):2745–2753.

[220] Chng TL, Lepikhin ND, Orel IS, Popov NA, Starikovskaia SM. TALIF measurements of atomic nitrogen in the afterglow of a nanosecond capillary discharge. Plasma Sources Sci Technol. 2020 mar;29(3):035017.

[221] Lozovoy V, Pastirk I, Walowicz K, Dantus M. Multiphoton intrapulse interference. II. Control of two-and three-photon laser induced fluorescence with shaped pulses. Artic J Chem Phys. 2003;.

[222] Jain A, Wang Y, Kulatilaka WD. Three-photon-excited laser-induced fluorescence detection of atomic hydrogen in flames. Opt Lett. 2019 dec;44(24):5945.

[223] Das P, Ondrey GS, van Veen N, Bersohn R. Two photon laser induced fluorescence of carbon atoms. J Chem Phys. 1983 jul;79(2):724–726.

[224] Heaven M, Miller TA, Freeman RR, White JC, Bokor J. Two-photon absorption, laser-induced fluorescence detection of Cl atoms. Chem Phys Lett. 1982 mar;86(5-6):458–462.

[225] Selwyn GS, Baston LD, Sawin HH. Detection of Cl and chlorine-containing negative ions in rf plasmas by two-photon laser-induced fluorescence. Appl Phys Lett. 1987 sep;51(12):898–900.

[226] Herring GC, Dyer MJ, Jusinski LE, Bischel WK. Two-photon-excited fluorescence spectroscopy of atomic fluorine at 170 nm. Opt Lett. 1988 may;13(5):360.

[227] Bokor J, Freeman RR, White JC, Storz RH. Two-photon excitation of the n = 3 level in H and D atoms. Phys Rev A. 1981 jul;24(1):612–614.

[228] Bischel WK, Perry BE, Crosley DR. Two-photon laser-induced fluorescence in oxygen and nitrogen atoms. Chem Phys Lett. 1981 aug;82(1):85–88.

[229] Adams SF, Miller TA. Two-photon absorption laser-induced fluorescence of atomic nitrogen by an alternative excitation scheme. Chem Phys Lett. 1998 oct;295(4):305–311.

[230] Brewer P, Van Veen N, Bersohn R. Two-photon induced fluorescence and resonance-enhanced ionization of sulfur atoms. Chem Phys Lett. 1982 sep;91(2):126–129.

[231] Brewer P, Das P, Ondrey G, Bersohn R. Measurement of the relative populations of I(2P 1/20) and I(2P3/20) by laser induced vacuum ultraviolet fluorescence. J Chem Phys. 1983 jul;79(2):720–723.

[232] Goehlich A, Kawetzki T, Döbele HF. On absolute calibration with xenon of laser diagnostic methods based on two-photon absorption. J Chem Phys. 1998 jun;108(22):9362–9370.

[233] Bokor J, Freeman RR, White JC, Storz RH. Two-photon excitation of the n=3 level in H and D atoms. Phys Rev A. 1981 jul;24(1):612–614.

[234] Heaven M, Miller TA, Freeman RR, White JC, Bokor J. Two-photon absorption, laser-induced fluorescence detection of Cl atoms. Chem Phys Lett. 1982 mar;86(5-6):458–462.

[235] Niemi K, Gathen SVD, Döbele V, Schulz-Von Der Gathen V, Döbele HF. Absolute Calibration of Atomic Density Measurements by Laser-Induced Fluorescence Spectroscopy with Two-Photon Excitation (TALIF). J Phys D Appl Phys. 2001;34(15):2330–2335.

[236] Loudon R. The Quantum Theory of Light - Paperback - Rodney Loudon - Oxford University Press; 1983.

[237] Park J, Henins I, Herrmann HW, Selwyn GS, Hicks RF. Discharge phenomena of an atmospheric pressure radio-frequency capacitive plasma source. J Appl Phys. 2001 jan;89(1):20–28.

[238] Dilecce G, Vigliotti M, Benedictis SD. A TALIF calibration method for quantitative oxygen atom density measurement in plasma jets. J Phys D Appl Phys. 2000 mar;33(6):53–56.

[239] Niemi K, O'Connell D, de Oliveira N, Joyeux D, Nahon L, Booth JP, et al. Absolute atomic oxygen and nitrogen densities in radio-frequency driven atmospheric pressure cold plasmas: Synchrotron vacuum ultra-violet high-resolution Fourier-transform absorption measurements. Appl Phys Lett. 2013 jul;103(3):034102.

[240] Jeong JY, Park J, Henins I, Babayan SE, Tu VJ, Selwyn GS, et al. Reaction chemistry in the afterglow of an oxygen-helium, atmospheric-pressure plasma. J Phys Chem A. 2000 aug;104(34):8027–8032.

[241] Bekefi G, G. Principles of laser plasmas; 1976.

[242] Bicchi P, Marinelli C, Mariotti E, Meucci M, Moi L. Energy-pooling ionization and electron-ion recombination measurements in indium. J Phys B At Mol Opt Phys. 1997 feb;30(3):473–482.

[243] Kurunczi P, Lopez J, Shah H, Becker K. Excimer formation in high-pressure microhollow cathode discharge plasmas in helium initiated by low-energy electron collisions. Int J Mass Spectrom. 2001 feb;205(1-3):277–283.

[244] Tachibana K, Kishimoto Y, Sakai O. Measurement of metastable He* (2 3S 1) density in dielectric barrier discharges with two different configurations operating at around atmospheric pressure. J Appl Phys. 2005 jun;97(12):123301.

[245] Nersisyan G, Morrow T, Graham WG. Measurements of helium metastable density in an atmospheric pressure glow discharge. Appl Phys Lett. 2004 aug;85(9):1487–1489.

[246] Cardoso RP, Belmonte T, Henrion G, Sadeghi N. Influence of trace oxygen on He(2 3S) density in a He-O 2 microwave discharge at atmospheric pressure: Behaviour of the time afterglow. J Phys D Appl Phys. 2006 oct;39(19):4178–4185.

[247] Reuter S, Niemi K, Schulz-Von Der Gathen V, Döbele HF. Generation of atomic oxygen in the effluent of an atmospheric pressure plasma jet. Plasma Sources Sci Technol. 2009 nov;18(1):015006.